

Rice University

**Profiling of Relaxation Time and Diffusivity Distributions with
Low Field NMR**

by

Michael T. Rauschhuber

A THESIS SUBMITTED
IN PARTIAL FULFILLMENT OF THE
REQUIREMENTS FOR THE DEGREE

Doctor of Philosophy

APPROVED, THESIS COMMITTEE

George J. Hirasaki, A.J. Harstook Professor, Chair
Chemical and Biomolecular Engineering

Walter G. Chapman, William W. Akers Professor
Chemical and Biomolecular Engineering

Andreas Lüttge, Professor
Earth Science and Chemistry

HOUSTON, TEXAS

April 2011

Abstract

Profiling of Relaxation Time and Diffusivity Distributions with Low-Field NMR

by

Michael T. Rauschhuber

Nuclear magnetic resonance (NMR) is a common tool utilized in core analysis. NMR can reveal important information about pore structure, fluid configuration and wettability. However, standard NMR core analysis techniques look at the sample as a whole or only at thin slices. Two NMR pulse sequences are introduced that allow for the determination of relaxation time or diffusion-relaxation time distributions as a function of sample height.

One-dimensional T_2 and D - T_2 profiles can be determined with a low-field Maran Ultra spectrometer by implementing nuclear magnetic resonance imaging techniques. Frequency encoding gradients impart spatial resolution to the measurements and allow for the creation of T_2 and D - T_2 profiles without having to perform multiple slice selective measurements. The first technique, denoted as RARE, relies solely on resolving transverse relaxation, T_2 , as a function of height. The second method, D - T_2 profiling, allows for the determination of both the diffusion coefficient, D , and T_2 as a function of height. The ability to resolve D in addition to T_2 allows fluids with overlapping relaxation times to be distinguished, and therefore it is not necessary to use D_2O in order

to differentiate the water signal from the oil signal. Implementation of these two methods allows for the determination of porosity and saturation profiles. Experiments were performed with a sandpack in order to demonstrate the applicability of these two techniques, and saturation profiles of a sandpack were determined at various stages of the flooding process.

Acknowledgements

I would like to thank my thesis advisor, Professor George Hirasaki, for his guidance throughout my career as a graduate student at Rice University. I would also like to thank Maura Puerto for her help in the design of the sandpack used in this study. I would like to acknowledge my colleagues in the Hirasaki Lab Group for insightful discussions, aid in performing experiments, and their friendship. Finally, I would like to thank all of my family and friends for their moral support during my graduate studies.

Table of Contents

Acknowledgements.....	ii
Table of Contents.....	v
List of Figures.....	vii
Table of Tables.....	xii
Nomenclature.....	xiii
Introduction.....	1
1.1 Literature Review.....	2
1.2 Overview.....	5
NMR Profiling.....	7
2.1 Frequency-Encoding Gradients.....	7
2.2 Basic Spin Echo (SE) Imaging Pulse Sequence.....	9
2.3 Image Contrast.....	12
2.4 T ₂ Profiling via Rapid Acquisition with Relaxation Enhancement (RARE).....	16
2.4.1 Effect of Diffusion.....	18
2.5 Selection of RARE Parameters.....	23
2.5.1 Sample Size and Position.....	23
2.5.3 Dwell Time.....	27
2.5.4 Number of Acquisition Points.....	30
2.5.5 Selection Criteria.....	32
2.6 Data Processing.....	41
2.6.1 Profile Averaging.....	43
2.7 Application.....	47
Summary.....	51
D-T ₂ Profiling.....	52
3.1 Development of the Pulse Sequence.....	53
3.1.1 Gradient Pulse Structure and Echo Stability.....	55
3.1.2 Increasing Pulse Sequence Phase Stability.....	58
3.1.3 Magnetization Equation.....	62
3.1.4 Data Processing.....	63
3.1.5 Phase Cycling.....	64
3.2 Determination of Porosity and Saturation Profiles.....	65

3.3 Parameter Selection	69
3.3.1 Diffusion Editing Parameters.....	71
3.3.2 Gradient Pre-Pulses.....	77
3.3.3 Spacing between RF and Gradient Pulses	85
3.4 SandPack Experiments.....	91
3.5 An Alternate Method to Calculate Saturation.....	100
3.6 Summary	113
Conclusions and Future Work	114
4.1 Conclusions.....	114
4.2 Future Work.....	116
References.....	119
Appendix.....	123
A.1 Matlab Subprograms and Subroutines	123
A.2 Operation of Matlab Code for RARE experiment	124
A.2 Operation of Matlab Code for D-T ₂ profiling experiment.....	125

List of Figures

Figure 2.1: One Dimensional Profiling Pulse Sequence.....	9
Figure 2.2: Collected Echo for a Water Sample with a height of 4 cm. $g_1=g_2=0.8 \text{ G cm}^{-1}$, $\delta_1 = 1.3 \text{ msec}$, $\delta_2 = 2\delta_1$, $SI = 64$, $DW = 0.04 \text{ msec}$	11
Figure 2.3: Profile of 4 cm water sample generated after FFT reconstruction of the collected echo.....	11
Figure 2.4: Spin Density image of a layered water and squalane system.....	14
Figure 2.5: T_1 -weighted image of a layered water and squalane system.....	14
Figure 2.6: T_2 -weighted image of a layered water and squalane system.....	15
Figure 2.7: RARE Pulse Sequence Diagram (Bernstein, King, & Zhou, 2004).....	16
Figure 2.8: RARE Profiles of a water sample with a 4 cm height.....	18
Figure 2.9: Representation of the effective gradient, $g \star t$, in the RARE sequence.	20
Figure 2.10: Comparison of RARE Attenuation ($h = 0 \text{ cm}$) to CPMG Attenuation for water. RARE parameters: $g_1 = g_2 = 0.8 \text{ G cm}^{-1}$, $2\delta_1 = \delta_2 = 2.6 \text{ msec}$, $\tau = 3.0 \text{ msec}$	22
Figure 2.11: Comparison of RARE Attenuation ($h = 0 \text{ cm}$) to CPMG Attenuation for water. RARE parameters: $g_1 = g_2 = 1.6 \text{ G cm}^{-1}$, $2\delta_1 = \delta_2 = 2.6 \text{ msec}$, $\tau = 3.0 \text{ msec}$	22
Figure 2.12: Results of a series of FID experiments performed on a 0.5 cm sample of water used to determine the sweet spot of the MARAN-M. The horizontal line denotes a 5% percent deviation from the maximum amplitude.....	24
Figure 2.13: Observed vs. Predicted behavior of the MARAN-M's gradient. Deviations are observed at very low values of g	25
Figure 2.14: Demonstration of profile rounding due to a large Δf	26
Figure 2.15: Improper selection of DW. The measurement resolved a length much greater than the sample height.	27
Figure 2.16: Dwell time selected so that the sample plus an excess of about half a centimeter above and below the sample is measured. All other parameters remain the same as the profile depicted in Figure 2.15.	29
Figure 2.17: Increasing SI increases the resolution of the profile. The only parameter changed from Figure 2.16 to this figure is SI from 64 (Figure 2.16) to 128 (above).	

Resolution has been increased from 2.2 points cm^{-1} (Figure 2.16) to 4.4 points cm^{-1} (above).	32
Figure 2.18: Measurement Resolution based on equation (2. 35).	35
Figure 2.19: Measurement Resolution based on equation (2. 35) with g_{\min} and g_{\max} denoted by the red, vertical dashed lines	36
Figure 2.20: Measurement resolution based on equation 4 with g_{\min} and g_{\max} denoted by the red, vertical dashed lines. Red dot corresponds to selected g and δ_1 pair ($g = 0.80 \text{ G cm}^{-1}$, $\delta_1 = 1.43 \text{ msec}$).	39
Figure 2.21: Dwell time as a function of g for $\delta_1 = 1.43 \text{ msec}$. The dashed line represents the maximum DW determined by g , h_s , and h_e	40
Figure 2.22: SI as a function of g for $\delta_1 = 1.43 \text{ msec}$	40
Figure 2.23: First echo acquired during a RARE experiment on a water sample after application of FFT. Data is presented beforen (left) and after (right) rotation.	42
Figure 2.24: Rotation of FFT data for a RARE experiment on a	42
Figure 2.25: RARE profiles of a water/squalane system. The points represent the un-averaged data will the line indicate the profiles after averaging has been performed.	44
Figure 2.26: RARE profile (16 th echo) of a water/squalane system. The blue line corresponds to the profile prior to averaging. The green line indicates the resulting profile after averaging.	45
Figure 2.27: T_2 profile of a water/squalane system using the un-averaged data.	46
Figure 2.28: T_2 profile of a water/squalane system using the averaged data.	46
Figure 2.29: T_2 map for TCL 80. The white line indicates the $T_{2, \log\text{mean}}$	49
Figure 2.30: Porosity Profile for TCL 80	49
Figure 2.31: T_2 map for Yates D. The white line indicates the $T_{2, \log\text{mean}}$	50
Figure 2.32: Porosity Profile for Yates D.	50
Figure 3.1: D - T_2 profiling pulse sequence	54
Figure 3.2: Unipolar pulsed field gradient stimulated echo pulse diagram (Tanner, 1970)	56

- Figure 3.3:** Bipolar pulsed field gradient stimulated echo pulse diagram (Cotts, Hoch, Sun, & Markert, 1989)..... 56
- Figure 3.4:** : Effect of Unipolar vs. Bipolar Gradient Pulses in a Stimulated Echo Diffusion Sequence. $\Delta = 60$ msec, $\delta = 3$ msec, $g = 20$ G cm⁻¹, $RD = 1$ sec, $NS = 64$, 1 min. wait between experiments. (i) Unipolar Pulses, 1st experiment, (ii) Unipolar Pulses, 4th experiment, (iii) Bipolar Pulses, 1st experiment, (iv) Bipolar Pulses, 4th experiment . 57
- Figure 3.5:** Initial design of D - T_2 profiling pulse sequence..... 60
- Figure 3.6:** Reduction of phase sensitivity. Squalane, $g = 2.5$ G cm⁻¹, $d = 6$ msec. (i) 1st two echoes before inclusion of $\pi/2$ pulse and, (ii) After. (iii) FFT quadrature data of all echoes at $h = 1.38$ cm echoes before inclusion of $\pi/2$ pulse, and (iv) After..... 61
- Figure 3.7:** Comparison of M_0 for water and SMY crude oil. The effective Hydrogen Index, $HI_{\text{eff,SMY}}$, for SMY is 0.58..... 66
- Figure 3.8:** D - T_2 profiling map of water and SMY in a sandpack after 0.3 PV waterflood at $h = 12.8$ cm. The diffusion coefficient for water and the D - T_2 correlation for dead crude oils correspond to the horizontal and sloped solid white lines. The dashed purple line indicates the cutoff value used in calculating saturation. 68
- Figure 3.9:** Expected attenuation ratio for water (left pane) and oil (right pane) using a 12 point gradient list. 73
- Figure 3.10:** Saturation Profiles for a collection of vials with varying heights of oil and water when the number of gradients used during inversion is reduced and spaced evenly with respect to g^2 . $S_0 = 1.0, 0.5, 0.33,$ and 0.25 from top to bottom..... 74
- Figure 3.11:** Saturation Profiles for a collection of vials with varying heights of oil and water when the number of gradients used during inversion is reduced and spaced geometrically. $S_0 = 1.0, 0.5, 0.33,$ and 0.25 from top to bottom..... 75
- Figure 3.12:** T_2 and D projections of D - T_2 profile maps for a sandpack after oilflood. Horizontal white lines indicate individual measurement regions 78
- Figure 3.13:** Porosity (left) and oil saturation (right) profiles generated from D - T_2 profiling measurements. Horizontal black lines indicate individual measurement regions. 79
- Figure 3.14:** First echo collected with D - T_2 profiling pulse sequence using a weak gradient ($g = 0.8$ G cm⁻¹) 80
- Figure 3.15:** First echo collected with D - T_2 profiling pulse sequence using a strong gradient ($g = 27.2$ G cm⁻¹). Note the presence of two peaks as compared to the single peak in Figure 3.14. 80

- Figure 3.16:** Results from D - T_2 profiling experiments performed using (i) 0, (ii) 1, (iii) 3, (iv) 5, (v) 7, and (vi) 9 gradient pre-pulses. The colored lines represent the first echo collected at $g = 19.4, 27.2, 32.2, 38.0, \text{ and } 45.0 \text{ G cm}^{-1}$ (from left to right)..... 82
- Figure 3.17:** First echo collected with D - T_2 profiling pulse sequence using a strong gradient ($g = 27.2 \text{ G cm}^{-1}$) and 9 gradient prepulses. Note the absence of two peaks as compared Figure 3.15 82
- Figure 3.18:** T_2 and D projections of D - T_2 profile maps for a sandpack after oilflood. The pulse sequence utilized 9 pre-pulses for the measurement of the top 3 sections and 0 prepulses for the bottom 2 sections. Horizontal white lines indicate individual measurement regions 83
- Figure 3.19:** Porosity (left) and oil saturation (right) profiles generated from D - T_2 profiling measurements. The pulse sequence utilized 9 pre-pulses for the measurement of the top 3 sections and 0 prepulses for the bottom 2 sections. Horizontal black lines indicate individual measurement regions..... 84
- Figure 3.20:** Pulse sequence used to examine the effect of RF-gradient pulse..... 87
- Figure 3.21:** Effect of δ_3 on the FID signal using the pulse sequence depicted in Figure 3.20..... 87
- Figure 3.22:** Profiles of first echo collected from D - T_2 profiling pulse sequence. Experiment with $\delta_3 = 1.0 \text{ msec}$ exhibits a smaller amplitude and noticeable rounding near the bottom of the measurement range in comparison to the experiment performed with $\delta_3 = 5.0 \text{ msec}$ 88
- Figure 3.23:** T_2 and D projections of D - T_2 profile maps for a sandpack after oilflood. Oilflood was performed at a rate of 5 ft day^{-1} . Horizontal white lines indicate individual measurement regions 89
- Figure 3.24:** Porosity (left) and oil saturation (right) profiles generated from D - T_2 profiling measurements. Oilflood was performed at a rate of 5 ft day^{-1} . Horizontal black lines indicate individual measurement regions. 90
- Figure 3.25:** T_2 and D projections of D - T_2 profile maps for a sandpack after oilflood. Oilflood was performed at a rate of 40 ft day^{-1} . Horizontal white lines indicate individual measurement regions 93
- Figure 3.26:** Porosity (left) and oil saturation (right) profiles generated from D - T_2 profiling measurements. Oilflood was performed at a rate of 40 ft day^{-1} . Horizontal black lines indicate individual measurement regions. 94
- Figure 3.27:** T_2 and D projections of D - T_2 profile maps for a sandpack after a 0.3 PV waterflood performed at a rate of 1 ft day^{-1} . Horizontal white lines indicate individual measurement regions 95

- Figure 3.28:** Porosity (left) and oil saturation (right) profiles generated from $D-T_2$ profiling measurements after a 0.3 PV waterflood performed at a rate of 1 ft day^{-1} . Horizontal black lines indicate individual measurement regions. 96
- Figure 3.29:** T_2 and D projections of $D-T_2$ profile maps for a sandpack after a 0.6 PV waterflood performed at a rate of 1 ft day^{-1} . Horizontal white lines indicate individual measurement regions 97
- Figure 3.30:** Porosity (left) and oil saturation (right) profiles generated from $D-T_2$ profiling measurements after a 0.6 PV waterflood performed at a rate of 1 ft day^{-1} . Horizontal black lines indicate individual measurement regions. 98
- Figure 3.31:** Oil saturation profiles after a 0, 0.3, and 0.6 PV waterflood. Note that one segment of the sandpack at 0 pV waterflood was not measured. 99
- Figure 3.32:** Fit results using just the Diffusion Coefficient from sandpack after 0.3 PV waterflood ($h = 22.6 \text{ cm}$). 102
- Figure 3.33:** $D-T_2$ map taken from a profile of a sandpack after a 0.3 PV waterflood ($h = 22.6 \text{ cm}$). The green box denotes the region of interest for the bivariate, bimodal fit. The white squares show the resulting log means from the fit..... 104
- Figure 3.34:** $D-T_2$ fitting results of data presented in Figure 3.33. The bimodal, bivariate fit is depicted (left) as well as the contribution from each phase: oil (center) and water (right). 105
- Figure 3.35:** $D-T_2$ fitting results of data in Figure 3.33 presented as projections onto T_2 (top) and D (bottom) axes. 105
- Figure 3.36:** Comparison of a saturation profile calculated using fitting and cutoff methods. 106
- Figure 3.37:** Comparison of a saturation profile calculated using fitting and cutoff methods for a system of vials with varying heights of water and SMY crude oil..... 108
- Figure 3.38:** Saturation Profile of a water saturated sandpack. Most of the peaks generated when using the cutoff method are removed by fitting the diffusion coefficient. 110
- Figure 3.39:** Fitting result from the water saturated sandpack at $h = 17.02 \text{ cm}$ (location corresponding to large spike in saturation profile, Figure 3.38)..... 111
- Figure 3.40:** Saturation Profile of a sandpack after a 0.6PV waterflood. Both methods yield a saturation profile with similar features, but the fitting method yields lower oil saturation..... 112

Table of Tables

Table 2.1: Parameters for desired image contrast (Liang & Lauterbur, 2000).....	13
Table 2.2: Summary of porosity measurements for TCL 80 and Yates D.....	48
Table 3.1: D - T_2 profiling phase cycling list.....	64
Table 3.2: Diffusion parameters selected for the measurement of a water saturated sandpack.....	70
Table 3.3: Imaging parameters selected for the measurement of a water saturated sandpack.....	70
Table 3.4: Quality of fit for D and D - T_2 fitting methods for the determination of saturation.....	107

Nomenclature

α	Regularization parameter
γ	Gyromagnetic ratio
$\delta_{1,2}$	Gradient pulse duration
δ_3	RF-gradient pulse spacing
Δ	Diffusion time for unipolar pulsed field gradient stimulated echo
Δ'	Diffusion time for bipolar pulsed field gradient diffusion measurement
$\Delta_{1,f}$	spacing between prephasing and readout gradient pulses
ϕ	Porosity
μ	Viscosity
τ	Echo spacing
τ_L	Echo spacing during the diffusion section of Diffusion Editing Pulse Sequence
τ_s	Echo spacing during the relaxation section of Diffusion Editing Pulse Sequence
σ	Interfacial tension
B_0	Magnetic field strength
D	Self-diffusion coefficient
DW	Dwell Time
f	Frequency
f_L	Larmor frequency
$g_{1,2,f}$	Imaging gradient strength
g_D	Diffusion gradient strength
h_s	Sample height
h_ϵ	Length outside of sample to be measured
HI	Hydrogen index
k	Permeability
L	Length of sandpack
M	Magnetization at time, t
M_0	Initial magnetization at time t = 0
$N_{C,end}$	Dimensionless Capillary end-effect Number

R	Diffusion attenuation ratio
S_o	Oil Saturation
SI	Number of acquisition points
t	time
T_1	Longitudinal relaxation time
T_2	Transverse relaxation time
$T_2^\#$	Effective transverse relaxation time due to diffusion attenuation caused by imaging gradient pulses
v	Superficial velocity
V	Volume
x	position

Chapter 1

Introduction

In 1946, the phenomenon of nuclear magnetic resonance (NMR) was first observed (Bloch, Hansen, & Packard, 1946) (Purcell, Torrey, & Pound, 1946). A few years later, Hahn (1950) observed a spin echo on an oscilloscope and proposed their use to determine relaxation times. Then, in 1973, the application of NMR to acquire spatial images was proposed (Lauterbur, 1973). Since then great strides have been made in the field of NMR. Chemical shift spectroscopy can be used to determine the chemical structure of a given compound. Imaging techniques can be applied to generate visualization of the internal properties of a sample (Bernstein, King, & Zhou, 2004). Pulsed-field gradient (PFG) measurements are sensitive to molecular motion and can therefore reveal information about the porous structures which hinder the random motion of molecules (Stejskal & Tanner, 1965). Now, NMR is a common tool in the scientific arena and has even become a mainstay in everyday life. One field of application for NMR is in core analysis.

The purpose of this research is to develop and implement new NMR technologies to better characterize porous media. Using the appropriate techniques, the NMR signal can reveal an enormous amount of information about sample properties. These properties include, but are not limited to, the heterogeneity, fluid configuration, wettability, and

pore structure of a core sample. Since the NMR signal is generated only by the fluid within the porous structure, the nature of that signal gives clues or insights into the pore space and mineral-fluid interactions. Therefore, core analysis can lead to better interpretation of well logs and greater understanding of core and reservoir properties. The scope of this work is to extend NMR imaging techniques for use with a low-field spectrometer, and then apply these methods to determine spatially varying properties, namely porosity and saturation.

1.1 Literature Review

Nuclear magnetic resonance (NMR) imaging is a tomographic technique in which spatial distributions of an object's physical or chemical properties can be generated via NMR signals (Liang & Lauterbur, 2000). Since NMR is a passive technology, analysis of a sample can be performed without harming or damaging it. NMR imaging, or more commonly magnetic resonance imaging (MRI), is most frequently associated with the medical field due to its increased application in clinical settings. However, NMR imaging techniques are applied in a broad range of other disciplines. For instance, MRI can be used to characterize flowing fluids, to monitor chemical reactors, and analyze fluid bearing porous media. Analysis of flowing systems allows for the determination of rheological properties such as the viscosity of polymeric fluids. Additionally, holdup and wetting in a packed bed reactor can be studied using imaging methods (Stapf & Han, 2006).

The implementation of NMR imaging techniques has proven to be successful in analyzing fluid bearing porous structures. Blackband et al. (1986) implemented a steady-state free precession (SSFP) technique in order to discriminate between fast and slow relaxing components of sand samples with known quantities of oil and water. The SSFP method resolved the apparent spin-density at only a thin slice; therefore, a set of measurements, each acquired at a different slice of the sample, is necessary to create a profile of the entire sample. Edelstein et al. (1988) achieved a porosity profile by using Carr-Purcell Fourier Imaging and determined average oil/water saturation of carbonate and sandstone cores using C^{13} spectra shift imaging. Using a medical MRI imaging unit, Baldwin and Yamanashi (1986) distinguished water and oil in a Berea core sample by adding Mn^{+2} ions to the aqueous phase to improve T_2 contrast. Mandava et al. (1990) used a single spin echo imaging sequence to obtain porosity and saturation profiles at different stages of the displacement of n-octadecane by heavy water from a limestone core.

Furthermore, imaging techniques allow for more than just the determination of sample saturations. For instance, Chen, Kim, Qin, & Watson (1992) examined core heterogeneity by generating cross-sectional thin-slice profiles of Brown sandstone having laminated structures with bedding planes. Fordham et al. (1993) measured T_2 as a function of sample position of a Richemont limestone saturated with n-dodecane and heavy water using a series of single spin echo imaging sequences, with each echo having a different degree of T_2 contrast. Quan et al. (1996) applied NMR imaging to examine the effects of steam foam flooding by monitoring fluid distributions within in a core. Johns and Gladden (1998) studied the dissolution and mobilization of octanol ganglia

trapped in a porous media by capillary forces and surrounded by water. Cheng, MacGregor, & Balcom (2005) imaged the flow of a commercially available viscous hydrocarbon, SAE 85W-140, through a sand pack using a phase-encoded multiple echo C^{13} MRI sequence. While C^{13} imaging allows for the direct detection of hydrocarbons, a low relative abundance and small gyromagnetic ratio of C^{13} hinder this approach from becoming an effective tool in examining partially saturated porous media, but C^{13} MRI imaging is still a powerful tool. For instance, the use of C^{13} imaging allows for the generation of transient profiles of the adsorption and desorption of CO_2 on zeolites (Cheng, Huang, Eic, & Balcom, 2005). NMR proton imaging can be used to generate water-air capillary pressure curves. Chen & Balcom (2005) generated water-air capillary pressure curves of a Berea sandstone using Single Point Ramped Imaging with T_1 Enhancement (SPRITE). Using SPRITE imaging, the water saturation profile was determined and then related to capillary pressure. Furthermore, pore-filling mechanism for co-current and counter-current imbibition were studied using SPRITE and Decay to Diffusion in an Internal Field (DIFF) (Chen, Butler, Gingras, & Balcom, 2005). Under counter-current imbibition, pores filled via a film-thickening mechanism while co-current imbibition exhibited a piston-like mechanism.

In the determination of saturation profiles using NMR imaging, many techniques have been applied. Most rely on the use of air/water systems (Chen & Balcom, 2005) (Green, Dick, McAloon, de J. Cano-Barrita, Burger, & Balcom, 2008) or the replacement of water with heavy water in order to negate its contribution to T_2 distributions (Green, Dick, McAloon, de J. Cano-Barrita, Burger, & Balcom, 2008) (Riskedal, Tipura, & Graue, 2008). Additionally, recent studies can be broadly divided into two categories

based on the imaging technique applied: slice selective and frequency-encoding. One example of slice selective measurements is the repeated application of a slice selective CPMG measurement along the length of a sample in order to generate a profile (Johannesen, Howard, & Graue, 2008). However, the two methods presented in this study illustrate the use of frequency-encoding gradients to determine either T_2 or $D-T_2$ profiles.

1.2 Overview

Two new methods for generating NMR profiles are presented in this document. The first is an imaging analogue of the CPMG measurement so that T_2 can be resolved as a function of sample height. The second is an imaging analogue of a pulsed field gradient diffusion editing experiment. The goal behind the design of these pulse sequences is to remove the limitation of measuring systems with only a single NMR sensitive phase while generating a profile without the need for multiple slice selective measurements. In order to accomplish this goal, the imaging experiments rely on the ability to measure either T_2 or $D-T_2$. In a few cases, oil and water within a core sample can be distinguished if they have non-overlapping T_2 distributions. However, most often the two phases possess overlapping T_2 distributions and cannot be distinguished without replacing the water with D_2O (Zhang, 2001) or adding Mn^{+2} ions to the aqueous phase (Stapf & Han, 2006). When oil and water have overlapping T_2 distributions, diffusion editing can be implemented. Diffusion editing is a method in which both relaxation and

diffusion data can be collected together (Hürlimann & Venkataramanan, 2002). The initial part of the sequence is designed to be sensitive to diffusion. The remaining portion of the sequence is composed of a train of π pulses enabling the measurement of T_2 . Since resolution is achieved in both diffusivity and T_2 , fluids with similar relaxation times can be differentiated if they have different diffusivities. If the viscosity contrast between oil and water is large enough, the two phases will have very different self-diffusion coefficients, and overlapping peaks in the T_2 distribution become two separate spots on a D - T_2 map allowing one to determine the contribution of each phase to the overall signal (Flaum, Chen, & Hirasaki, 2004).

In this document each pulse sequence is presented in a separate chapter. Chapter 2 introduces basic techniques needed to produce an NMR profile. Also included in Chapter 2 is the pulse sequence designed to measure T_2 profiles. Then, Chapter 3 addresses the construction of the D - T_2 profiling sequence. A glossary of terms is defined in the Nomenclature Section, and operation of any relevant code is addressed in the Appendix.

Chapter 2

NMR Profiling

Magnetic resonance imaging (MRI) relies on the fundamental principles of nuclear magnetic resonance (NMR) to extract spatial information about a given sample. While standard NMR techniques, such as CPMG, tend to look at either the whole sample or only a thin slice, MRI can be implemented in order to study the configuration of fluids within a core. Spatial resolution of properties such as magnetization and relaxation times will allow for the determination of saturation profiles and sample heterogeneities, such as changes in local porosity or pore size distribution. However, these experiments are typically limited to imaging or high field spectrometers. Applications in this study will focus on the use of a low-field instrument (2 MHz Maran Ultra) to determine sample heterogeneities in one dimension (1-D) by generating T_2 profiles.

2.1 Frequency-Encoding Gradients

Frequency encoding is a standard MR technique used to detect spatial information from a desired sample. In a uniform magnetic field, protons precess at the same frequency, known as the Larmor frequency.

$$f_L = \frac{\gamma}{2\pi} B_0 \quad (2.1)$$

When a magnetic gradient is applied, the intensity of the magnetic field and subsequently, the precession frequency varies with spatial position. For instance, under the application of a linear gradient field, the spatially dependent precession frequency can be represented by

$$f(x) = \frac{\gamma}{2\pi} (B_0 + g_x x) \quad (2.2)$$

Or

$$f(x) = f_L + \frac{\gamma}{2\pi} g_x (x - x_L) \quad (2.3)$$

where g_x designates the gradient strength and x denotes position. Therefore, spatial information can be extracted from the sample's various precession frequencies.

Consequently, g_x is referred to as a frequency-encoding gradient (Bernstein, King, & Zhou, 2004).

2.2 Basic Spin Echo (SE) Imaging Pulse Sequence

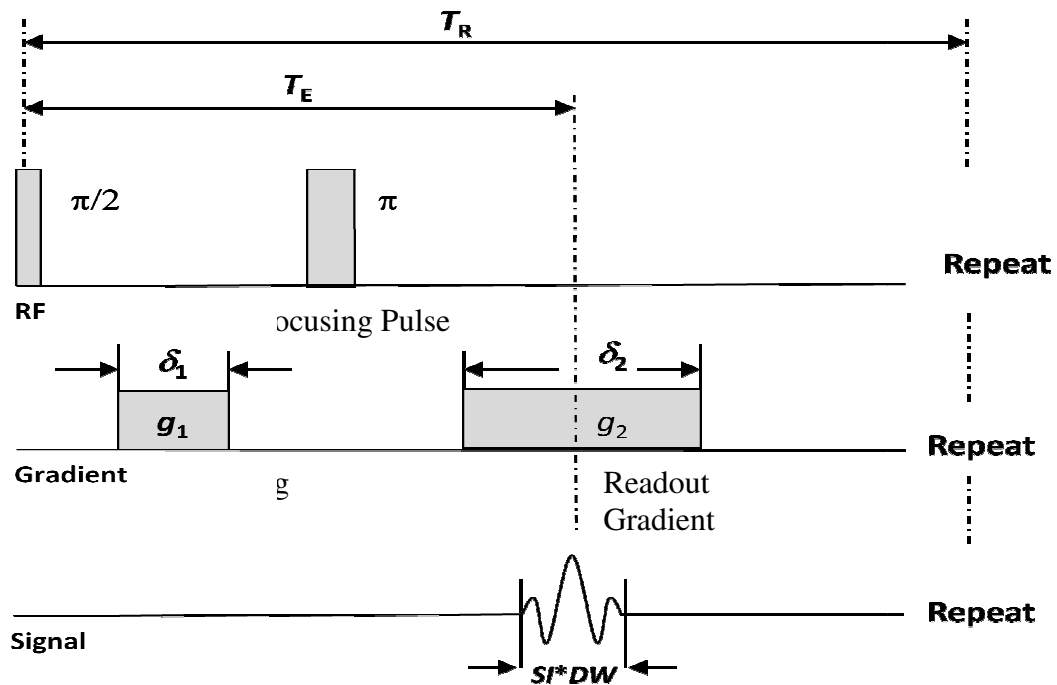


Figure 2.1: One Dimensional Profiling Pulse Sequence (Bernstein, King, & Zhou, 2004)

The basic spin echo imaging pulse sequence is presented in Figure 2.1. The radiofrequency (RF) pulse structure is the same as found in the Carr-Purcell-Meiboom-Gill (CPMG) experiment. The first $\pi/2$ pulse tips the magnetization into the transverse plane and the π pulse refocuses the signal allowing for formation of an echo at time, T_E . The imaging portion of the sequence is comprised of two gradient pulses, the prephasing and readout pulses, which are separated by a refocusing RF pulse. The prephasing pulse prepares the system for an echo to occur later. The prephasing pulse causes the magnetic field to be stronger at one position than another resulting in non-uniform precession frequencies throughout the sample. Therefore, spin isochromats, regions of constant precession frequency, will begin to amass phase at different rates. Then, the refocusing pulse flips all of the spins by 180° . The subsequent readout pulse plays a similar role as

the prephasing pulse, causing different isochromats to gather phase at different rates. Due to the application of a refocusing pulse, the isochromats that were spinning the slowest during the prephasing pulse will be precessing the fast during the readout pulse. This results in the formation of an echo (Bernstein, King, & Zhou, 2004).

The temporal location of the echo depends not on the spacing of the RF pulses, but on the duration and magnitude of the gradient pulses. When the area under the readout pulse equals the area under the prephasing pulse, the echo will reach its maximum. A one dimensional profile is then attained by performing a direct fast Fourier transform (FFT) reconstruction of the acquired signal (Liang & Lauterbur, 2000). For instance, a collected echo is depicted in Figure 2.2 and its corresponding 1-D profile in Figure 2.3. Note that the scale of the ordinate in Figure 2.3 is in centimeters not Hertz; the conversion between the two is made via the linear relationship described in equation (2.4).

$$f - f_L = \frac{\gamma}{2\pi} g_x (x - x_L) \quad (2.4)$$

where x_L corresponds to the sample height at which $f = f_L$.

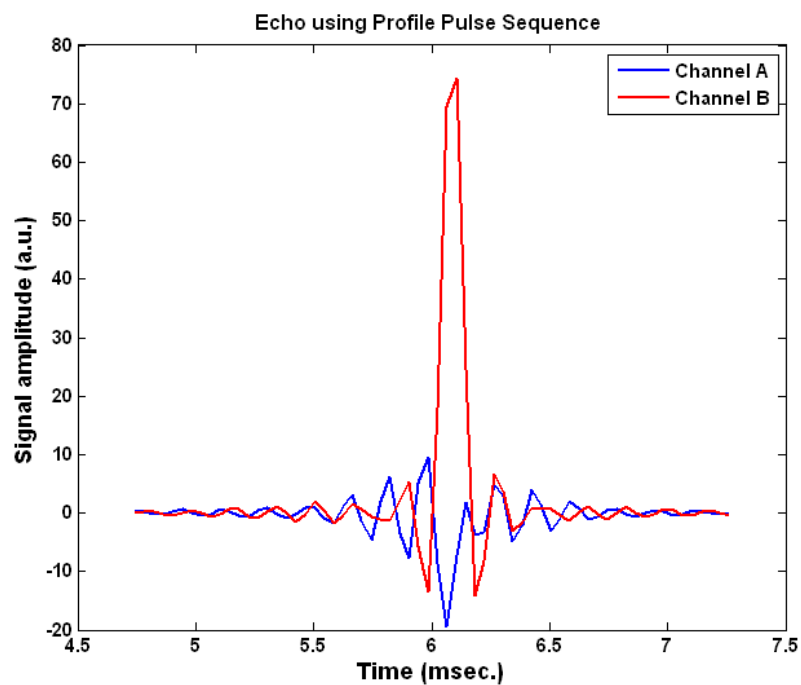


Figure 2.2: Collected Echo for a Water Sample with a height of 4 cm.
 $g_1=g_2=0.8 \text{ G cm}^{-1}$, $\delta_1 = 1.3 \text{ msec}$, $\delta_2 = 2\delta_1$, $SI = 64$, $DW = 0.04 \text{ msec}$

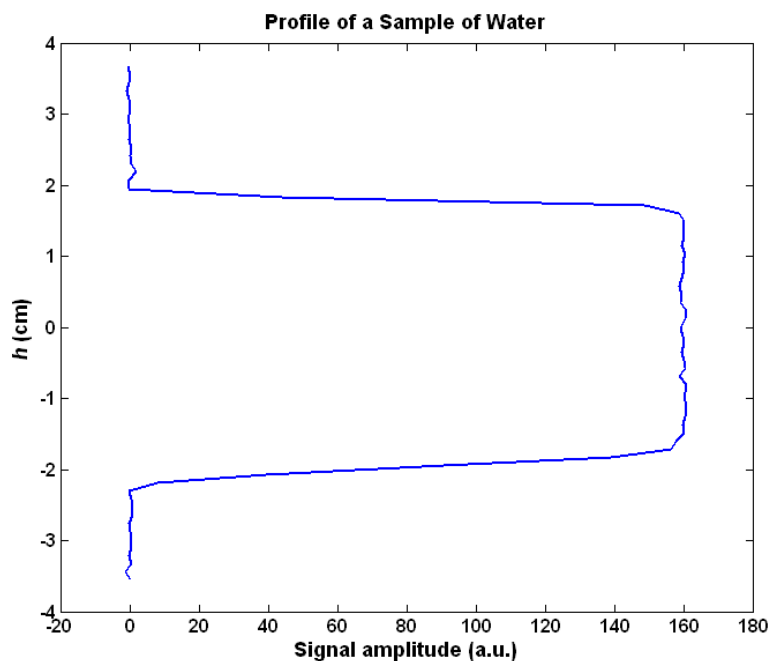


Figure 2.3: Profile of 4 cm water sample generated after FFT reconstruction of the collected echo.

2.3 Image Contrast

Image contrast is a technique used to stress either the T_1 or T_2 component of relaxation. Three types of contrast methods are readily applicable to this pulse sequence: spin-density, T_1 -weighting, and T_2 -weighting. The easiest way to understand how to generate an image with the desired contrast method is to consider the magnetization equation and how it may apply to a system with two vastly different relaxations times (e.g., squalane layered on top of water). For the previously described basic spin echo imaging pulse sequence, the magnetization is described by equation (2. 5).

$$M = M_0 \left[1 - \exp\left(\frac{-T_R}{T_1}\right) \right] \left[\exp\left(\frac{-T_E}{T_2}\right) \right] \quad (2. 5)$$

where T_E is the time at which the echo center occurs and T_R is the repetition time between scans (Liang & Lauterbur, 2000). The parameters T_E and T_R can be selected in such a manner so that the profile is representative of M_0 or is either weighted by the T_1 or T_2 terms. Therefore, image contrast can be used to help differentiate fluids with varying relaxation times as in the squalane/water example. In Table 2.1, guidelines for selecting T_E and T_R for a given method of contrast are given.

Table 2.1: Parameters for desired image contrast (Liang & Lauterbur, 2000) T_A : relaxation time of fast relaxing component T_B : relaxation time of slow relaxing component

Method of Contrast	T_E	T_R
Spin Density	$T_E \ll T_A < T_B$	$T_A < T_B \ll T_R$
T_1 -weighted	$T_E \ll T_A < T_B$	$T_A < T_R < T_B$
T_2 -weighted	$T_A < T_E < T_B$	$T_A < T_B \ll T_R$

For T_1 contrast, selection of T_R should allow for one fluid to be fully polarized while the other is only partially polarized. Similarly, for T_2 contrast, the proper choice of T_E allows for greater relaxation of one fluid than the other. The difference between the various contrast methods are illustrated in the figures below. All profiles are of the same layered water ($T_2 = 2.80$ sec) and squalane ($T_2 = 120$ msec) system, and the only parameters varying are T_E and T_R . Figure 2.4 represents a spin-density image. The two phases cannot be distinguished from one another because both water and squalane have similar hydrogen indexes. On the other hand, the squalane layer in a T_1 -weighted image (Figure 2.5) has a much larger amplitude because it is allowed to fully polarize between scans while the water is not. Finally, Figure 2.6 is an illustration of a T_2 -weighted image in which both phases are allowed to fully polarize between scans. Therefore, a long T_E results in greater relaxation in the oil phase and, subsequently, greater amplitude of the water phase. However, the longer T_E will also result in relaxation due to diffusion if the gradient is too large.

Spin Density Image of a Layered Water/Squalane System ($T_E = 8$ msec, $T_R = 15,000$ msec)

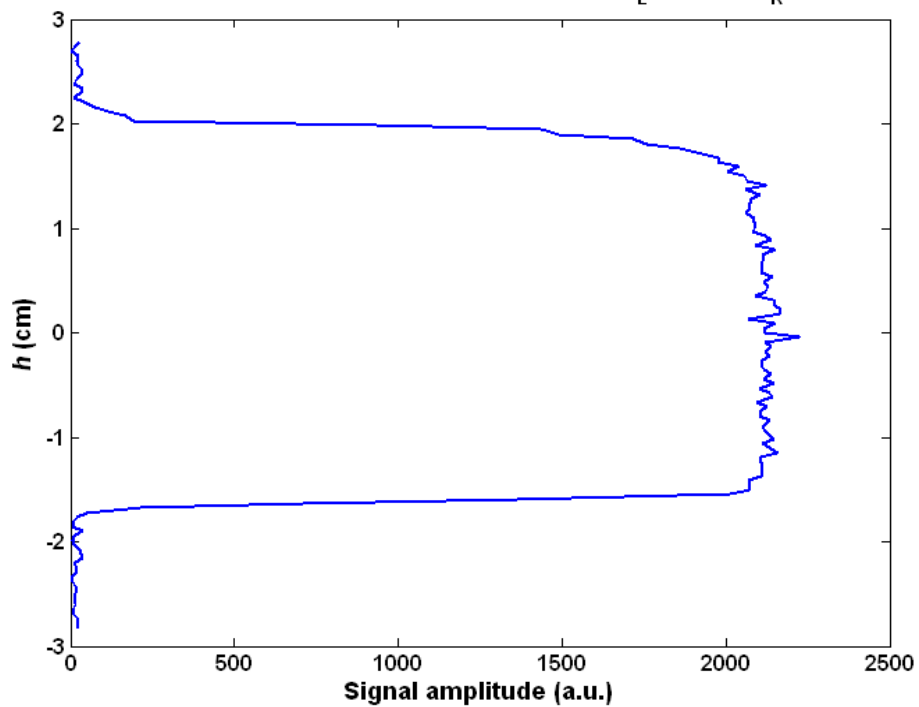


Figure 2.4: Spin Density image of a layered water and squalane system

T_1 -Weighted Image of a Layered Water/Squalane System ($T_E = 8$ msec, $T_R = 714$ msec)

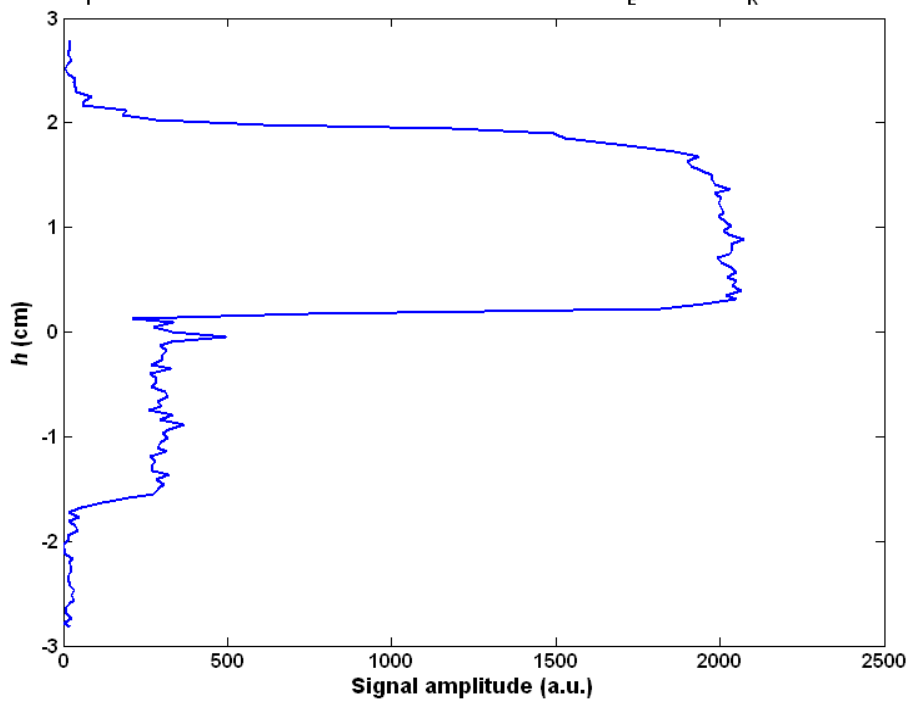


Figure 2.5: T_1 -weighted image of a layered water and squalane system

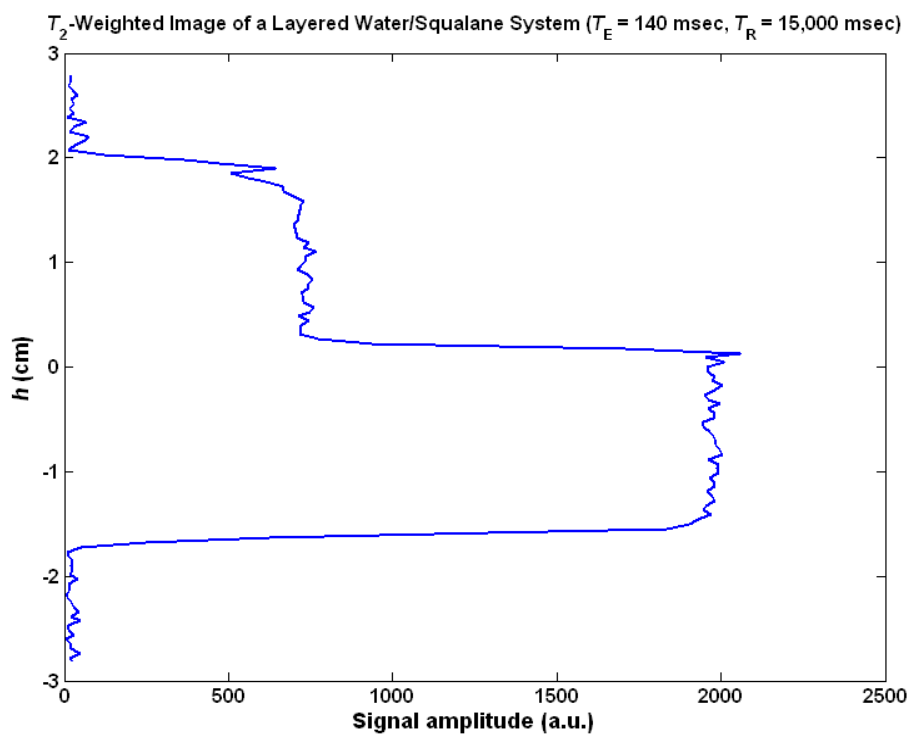


Figure 2.6: T_2 -weighted image of a layered water and squalane system

2.4 T_2 Profiling via Rapid Acquisition with Relaxation Enhancement (RARE)

The rapid acquisition with relaxation enhancement pulse sequence (RARE) is a CPMG-style extension of the one dimensional profile measurement first proposed by Henning et al. (1986). It is commonly used for clinical imaging, but modifications to the sequence must be made in order to accommodate the use of a Maran. Presented below is a schematic of the pulse sequence created for the Maran.

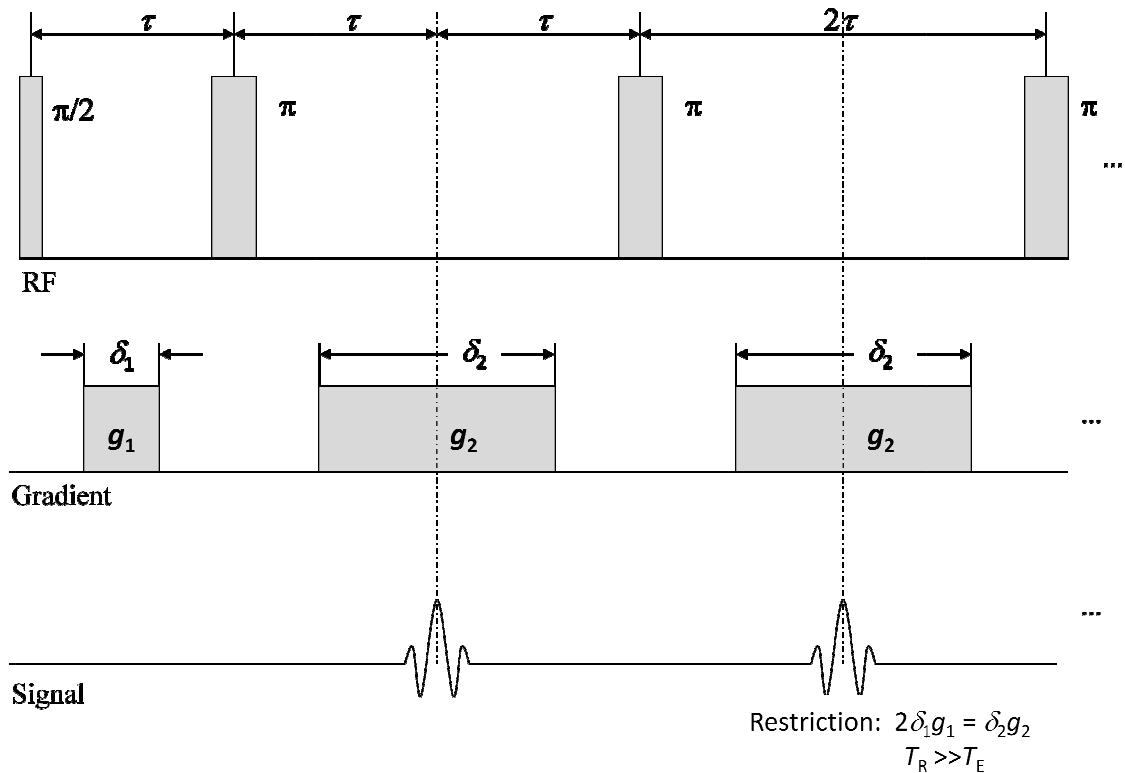


Figure 2.7: RARE Pulse Sequence Diagram (Bernstein, King, & Zhou, 2004)

In the above schematic, the first gradient pulse is known as the pre-phasing pulse and all subsequent gradient pulses are referred to as readout or imaging pulses. Both pulses play analogous roles as their counterparts in the one dimensional profiling pulse

sequence with one significant exception. As in the profiling sequence, the temporal location of the echo occurs when the area of the readout pulse is equivalent to the area under the prephasing pulse. Therefore, the remainder of the readout pulse acts as a prephasing pulse for the next echo. Resulting from this fact stems a careful balance between the two gradient pulses. In other words, the readout pulse should have twice the area of the prephasing pulse. In Figure 2.7, note that $2g_1\delta_1 = g_2\delta_2$.

The Fourier transform can be taken for each individual echo to obtain a series of one-dimensional profiles. The attenuation in the signal is also observable in the profiles. Therefore, the goal behind using such a sequence is to take advantage of the frequency encoding gradients and extract T_2 information as a function of position within the sample. A series of profiles with an increasing amount of T_2 relaxation generated by the RARE sequence is shown in Figure 2.8.

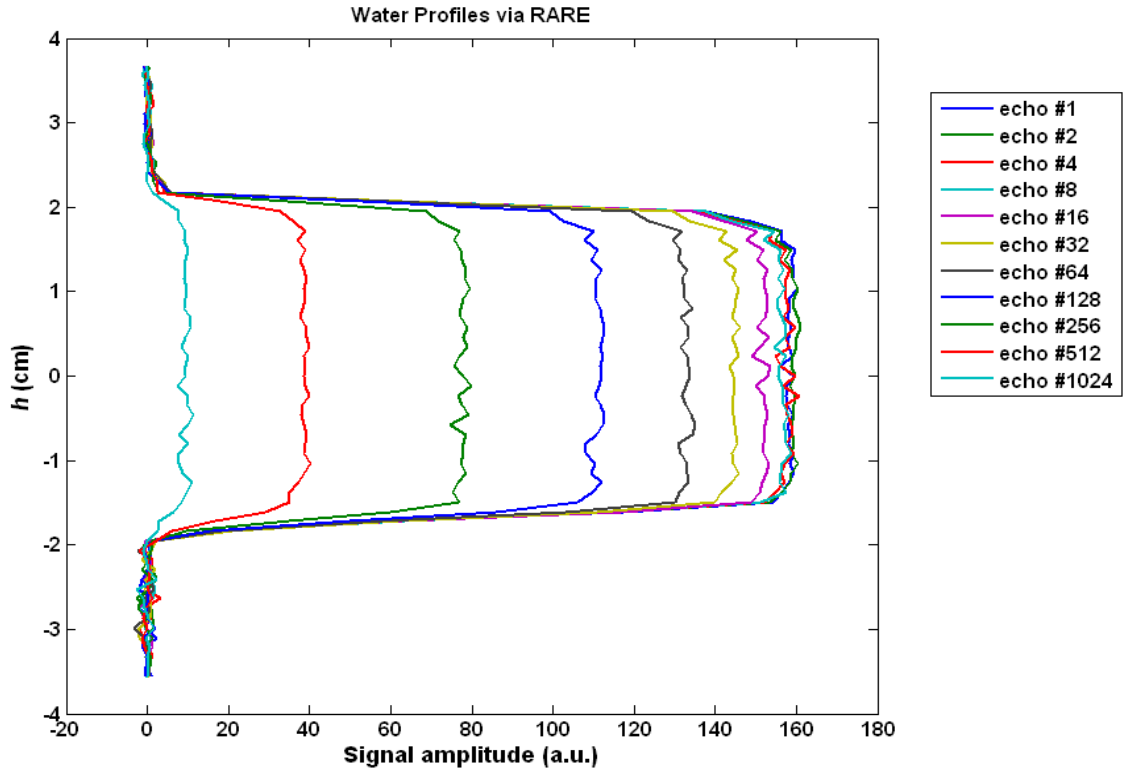


Figure 2.8: RARE Profiles of a water sample with a 4 cm height.
 $g_1 = g_2 = 0.800 \text{ G cm}^{-1}$, $\delta_1 = 1.30 \text{ msec}$, $\delta_2 = 2\delta_1$, $\tau = 3.00 \text{ msec}$, $DW = 40.0 \text{ msec}$, $SI = 64$

2.4.1 Effect of Diffusion

Due to the presence of multiple gradient pulses, attenuation due to diffusion can become significant. Therefore, it is necessary to develop a suitable model describing the attenuation in terms of the relevant parameters of the pulse sequence. Callaghan (1991) suggests that one method which can be used to determine the effect of self-diffusion is the application of the Bloch-Torrey equations. In the rotating reference frame, the effect of self-diffusion and velocity on the transverse magnetization, M_T , can be represented by (Torrey, 1956)

$$\frac{\partial M_T}{\partial t} = -i\gamma \mathbf{r} \cdot \mathbf{g} M_T - \frac{M_T}{T_2} + D\nabla^2 M_T - \nabla \cdot \mathbf{v} M_T \quad (2.6)$$

With the solution (Stejskal & Tanner, 1965)

$$M_T(r, t) = A(t) \exp \left[-i\gamma \mathbf{r} \cdot \int_0^t \mathbf{g}(t') dt' \right] \exp \left(\frac{-t}{T_2} \right) \quad (2.7)$$

At the echo center, $\int_0^t \mathbf{g}(t') dt'$ is equaled to zero. Therefore, equation (2.7) reduces to

$$M_T(r, t) = A(t) \exp \left(\frac{-t}{T_2} \right) \quad (2.8)$$

Substituting equation (2.8) into equation (2.6) yields an expression for A(t).

$$\frac{\partial A(t)}{\partial t} = -D\gamma^2 \left(\int_0^t \mathbf{g}(t') dt' \right) \exp \left(\frac{-t}{T_2} \right) \quad (2.9)$$

$$A(t) = \quad (2.10)$$

$$\exp \left[-D\gamma^2 \int_0^t \left(\int_0^{t'} \mathbf{g}(t'') dt'' \right)^2 dt' \right] \exp \left[i\gamma \mathbf{v} \cdot \int_0^t \left(\int_0^{t'} \mathbf{g}(t'') dt'' \right) dt' \right]$$

If there is no flow, this expression can be reduced to

$$A(t) = \exp \left[-D\gamma^2 \int_0^t \left(\int_0^{t'} \mathbf{g}(t'') dt'' \right)^2 dt' \right] \quad (2.11)$$

This formulation neglects the presence of RF pulses. However, the effect of the RF pulses can be accounted for by examining the “effective gradient”. When a π pulse is applied, the phase shift due to the presence of the gradient is flipped. This is equivalent to applying a gradient pulse with the opposite polarity. Therefore, the effective gradient

, $g^*(t)$, can be thought of as gradient pulses required to refocus the signal in the absence of 180° RF pulses, and is represented in the following figure for the RARE sequence.

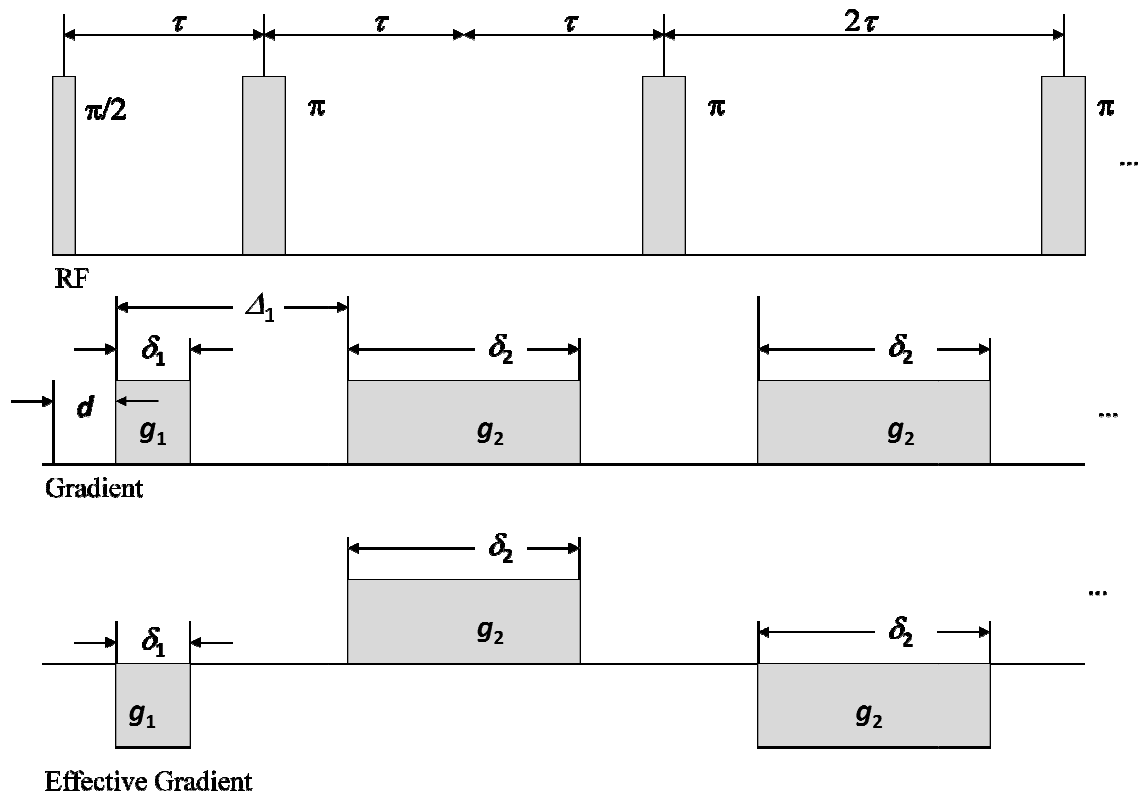


Figure 2. 9: Representation of the effective gradient, $g^*(t)$, in the RARE sequence.

Or the effective gradient, $g^*(t)$, can be defined as

0	when $0 < t < d$
$-g_1$	when $d < t < d + \delta_1$
0	when $d + \delta_1 < t < d + \Delta_1$
g_2	when $d + \Delta_1 < t < 2\tau + \delta_2/2$
0	when $2\tau + \delta_2/2 < t < 4\tau - \delta_2/2$
$-g_2$	when $4\tau - \delta_2/2 < t < 4\tau + \delta_2/2$
0	when $4\tau + \delta_2/2 < t < 6\tau - \delta_2/2$
g_2	when $6\tau - \delta_2/2 < t < 6\tau + \delta_2/2$
...	
$-g_2$	when $2n\tau - \delta_2/2 < t < 2n\tau + \delta_2/2$, where n , the number of echoes, is even.

Using these facts and imposing the stipulation that $g_1 = g_2 = g$ and $2\delta_1 = \delta_2$, $A(t)$ takes the form

$$A(t) = \exp \left[-D\gamma^2 g^2 \delta_1^2 \left(2(n-1)\tau + \Delta_1 - \frac{(n-1)}{3} \delta_2 \right) \right] \quad (2.12)$$

Therefore, the magnetization at the echo center of the RARE sequence can be described by

$$\frac{M(t)}{M_0} = \exp \left[-D\gamma^2 g^2 \delta_1^2 \left(2(n-1)\tau + \Delta_1 - \frac{(n-1)}{3} \delta_2 \right) \right] \exp \left(\frac{-t}{T_2} \right) \quad (2.13)$$

Where n is the number of echoes. A comparison of this equation to experimental results can be seen in Figure 2.10 and Figure 2.11. Water was used as the sample. The blue curve represents the CPMG decay, the green curve is the decay of the RARE profiles at the specified sample location, and the red curve is the calculated behavior. When $g = 0.8$ or 1.6 G cm^{-1} , the RARE decay is noticeable different from the CPMG decay. In both instances, this discrepancy is caused attenuation due to diffusion. Equation (2.13) accurately captures the impact of diffusion on the signal decay and overlays the RARE decay curve in both Figure 2.10 and Figure 2.11.

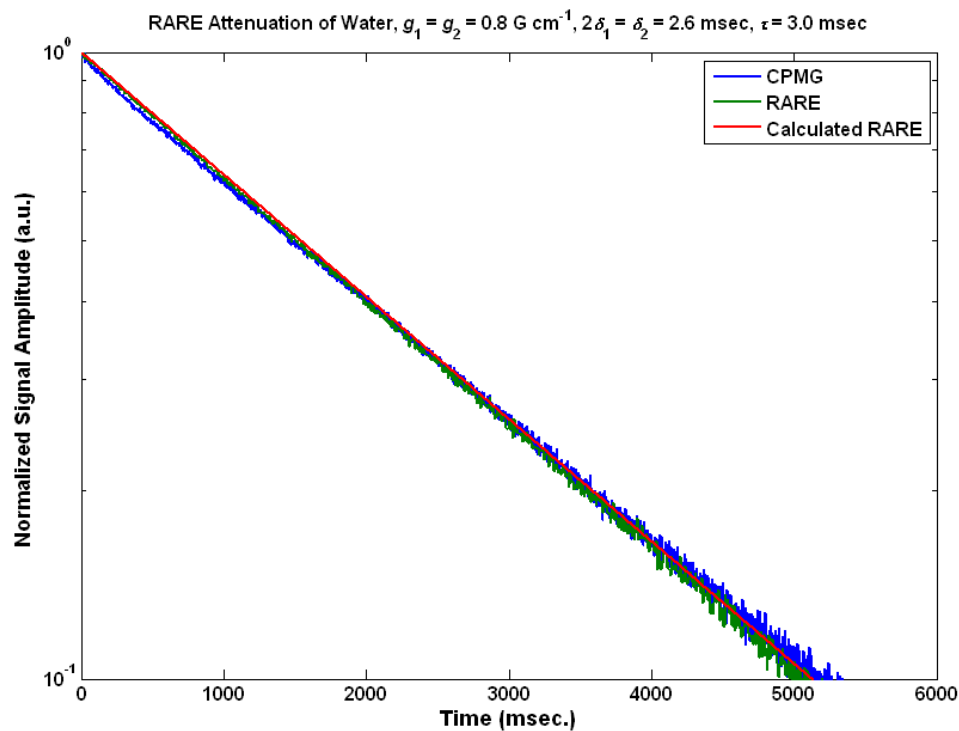


Figure 2.10: Comparison of RARE Attenuation ($h = 0 \text{ cm}$) to CPMG Attenuation for water. RARE parameters: $g_1 = g_2 = 0.8 \text{ G cm}^{-1}$, $2\delta_1 = \delta_2 = 2.6 \text{ msec}$, $\tau = 3.0 \text{ msec}$

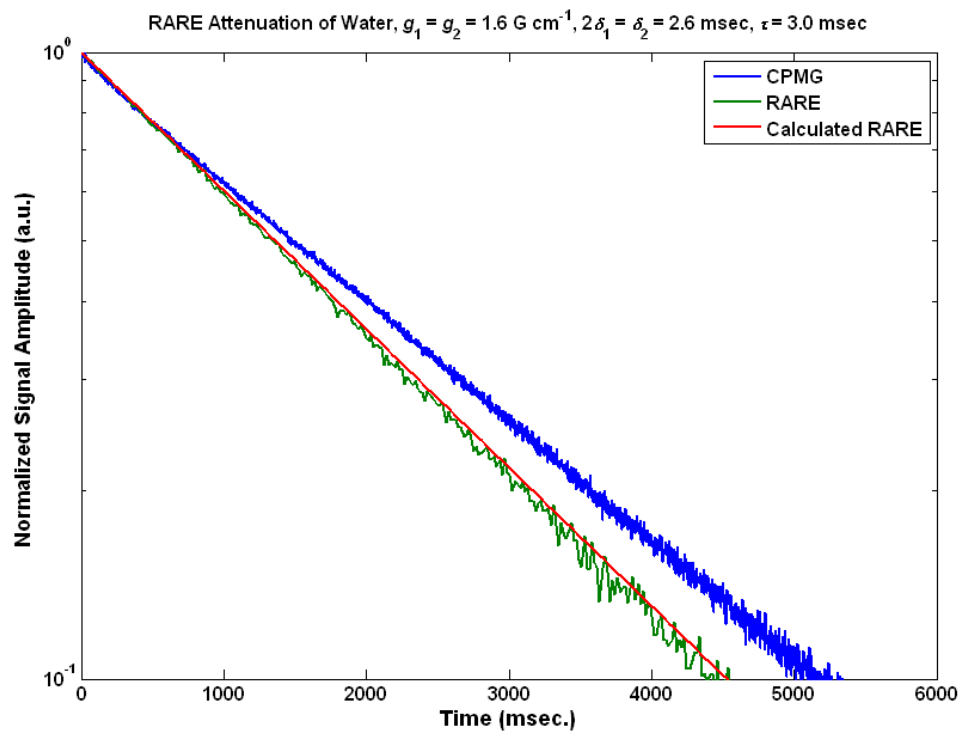


Figure 2.11: Comparison of RARE Attenuation ($h = 0 \text{ cm}$) to CPMG Attenuation for water. RARE parameters: $g_1 = g_2 = 1.6 \text{ G cm}^{-1}$, $2\delta_1 = \delta_2 = 2.6 \text{ msec}$, $\tau = 3.0 \text{ msec}$

2.5 Selection of RARE Parameters

The generation of NMR 1-D profiles is highly dependent upon the selected experimental parameters such as the sample size and location, gradient strength (g) and duration (δ), the dwell time (DW), and the number of acquisition points (SI). Choosing experimental parameters is not a trivial task since an interdependence of the parameters exists. For example, a long acquisition time will yield a higher resolution image, but will require longer gradient pulses ultimately causing greater diffusion attenuation. This section discusses the relevant parameters, their impact on the quality of the collected image, and proposes a selection method.

2.5.1 Sample Size and Position

The sample should be located within the sweet spot of the NMR and centered about f_{Larmor} . In order to determine the size and location of the sweet spot, a series of FID experiments were performed with water. The water sample has a height 0.5 cm and was moved in 0.5cm increments through the probe; an FID was performed at each location. The results are illustrated in Figure 2.12. From these results, it was determined the sweet spot was about 5 cm long. Therefore, for all subsequent measurements, the sample will be located within the sweet spot and have a height of 4 cm.

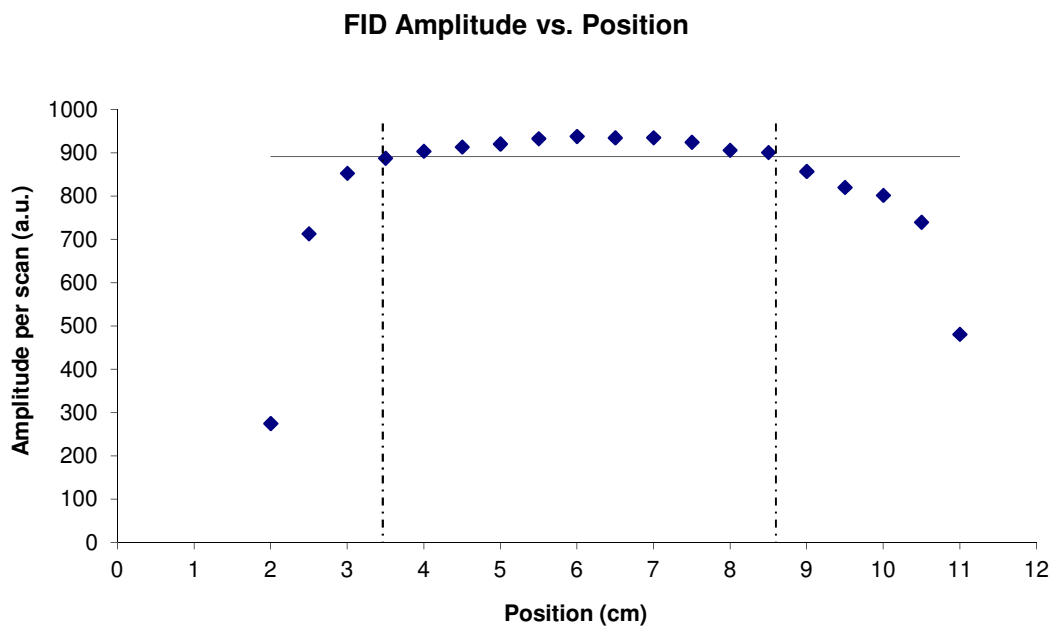


Figure 2.12: Results of a series of FID experiments performed on a 0.5 cm sample of water used to determine the sweet spot of the MARAN-M. The horizontal line denotes a 5% percent deviation from the maximum amplitude.

2.5.2 Gradient Strength

Gradient pulses are necessary in order to generate MRI images, and subsequently a range a viable gradient strengths exists. On one hand, the presence of multiple gradient pulses results in a greater amount of attenuation due to diffusion. One way to reduce the diffusion attenuation is to use weaker gradient pulses. Therefore, it is necessary to properly characterize the behavior of the gradient over a range of values. For instance, at very low gradients, the expected behavior deviates from what is observed. This deviation marks the lower range of reliable gradient strengths, g_{\min} ,

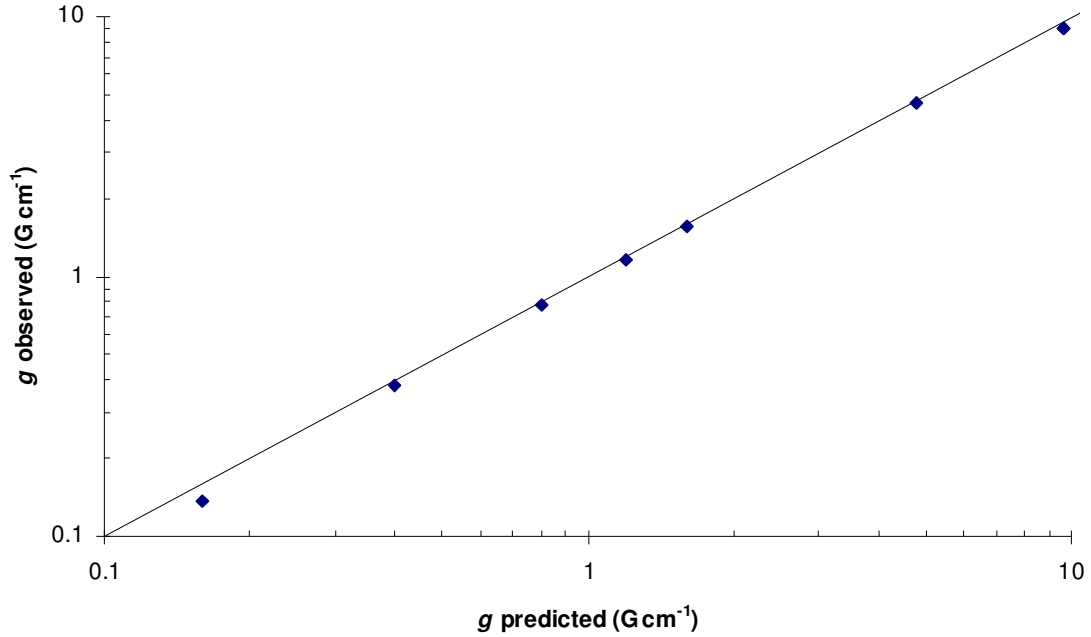


Figure 2.13: Observed vs. Predicted behavior of the MARAN-M's gradient. Deviations are observed at very low values of g

On the other hand, the maximum gradient strength, g_{\max} , depends on the probe's bandwidth as well as the height of the sample. The spectrometer is most sensitive to frequencies near the Larmor frequency, and the probe's response to frequency diminishes as the encoded frequencies deviate farther from the Larmor frequency. Profile rounding can occur as g becomes larger, and therefore, it is desired to keep the gradient small enough so that the range of encoded frequencies, Δf , does not exceed the linear response range of the probe.

$$\Delta f = \frac{\gamma}{2\pi} g h_s \quad (2.14)$$

Figure 2.14 demonstrates profile rounding. In this plot, the range of encoded frequencies is about 30 kHz, and slight rounding is noted at the top and bottom of the sample.

Selection of g_{\max} should limit the range of encoded frequencies so that rounding does not occur.

$$g_{\max} = \frac{2\pi\Delta f_{\max}}{\gamma h_S} \quad (2.15)$$

Where Δf_{\max} is the maximum allowable frequency range. Δf_{\max} has been set to 30 kHz for the subsequent calculations.

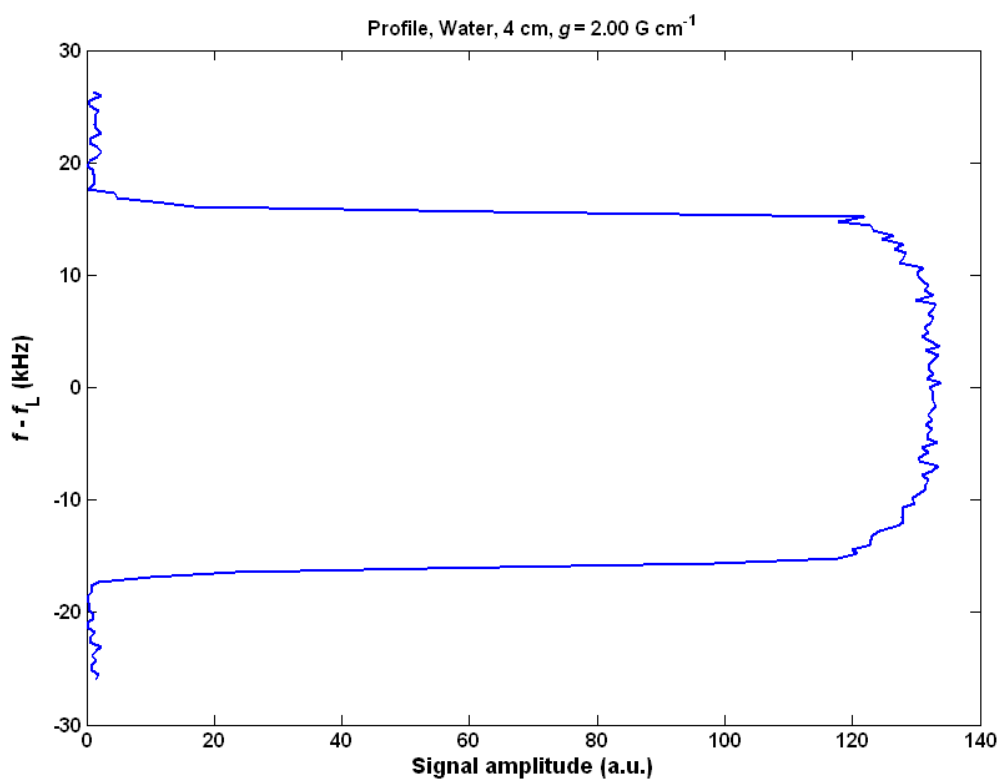


Figure 2.14: Demonstration of profile rounding due to a large Δf

2.5.3 Dwell Time

The dwell time (DW) is the spacing between the acquired data points. The reciprocal of the dwell time is the sampling rate, and the sampling rate must be large enough to measure all of the frequencies encoded in the sample without aliasing the signal. Since the gradient strength relates the encoded frequencies to sample position, DW governs the measurement length of the imaging experiment. Therefore, DW should be selected to acquire data over the length of the sample plus a small distance beyond. If the dwell time is too short, the distance which the measurement can identify is much longer than the length of the sample (Figure 2.15).

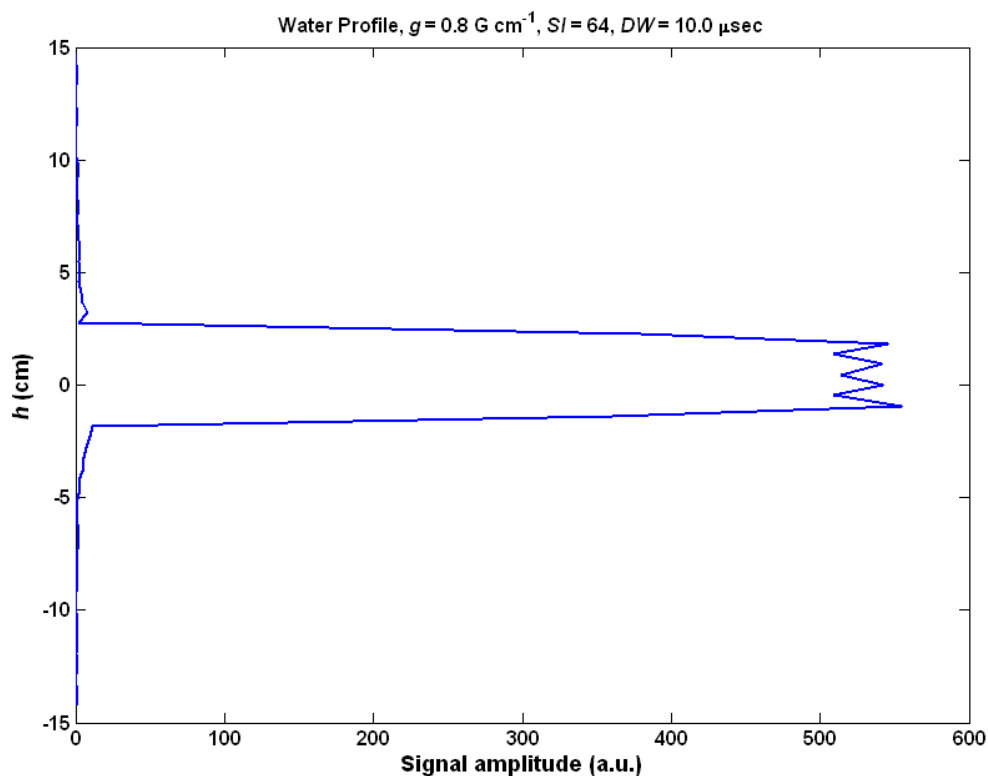


Figure 2.15: Improper selection of DW . The measurement resolved a length much greater than the sample height.

The largest, useable dwell time, DW_{max} , can be determined from the size of the sample and the strength of the gradient pulses applied. Equation (2. 17) gives a means of calculating an appropriate DW_{max} . This equation is based on the Nyquist sampling theorem which states that the sampling rate, SR , should be at least twice the maximum frequency encoded in the signal where the maximum encoded frequency, f_{max} , corresponds to half the sample height plus a small distance outside for a centered sample (Bernstein, King, & Zhou, 2004). If this criterion is not met, aliasing can occur.

$$SR_{max} = \frac{1}{DW_{max}} = 2f_{max} \quad (2. 16)$$

$$DW_{max} = \frac{1}{2f_{max}} = \frac{1}{2 \left(\frac{\gamma}{2\pi} g \frac{h_s + h_\epsilon}{2} \right)} = \frac{2\pi}{\gamma g (h_s + h_\epsilon)} \quad (2. 17)$$

where h_s is the sample height and h_ϵ is the length outside of the sample to be measured.

For example, Figure 2.16 depicts a profile in which the dwell time has been chosen so that the sample plus about half a centimeter above and below the sample is resolved.

Note that only DW has changed between Figure 2.15 and Figure 2.16.

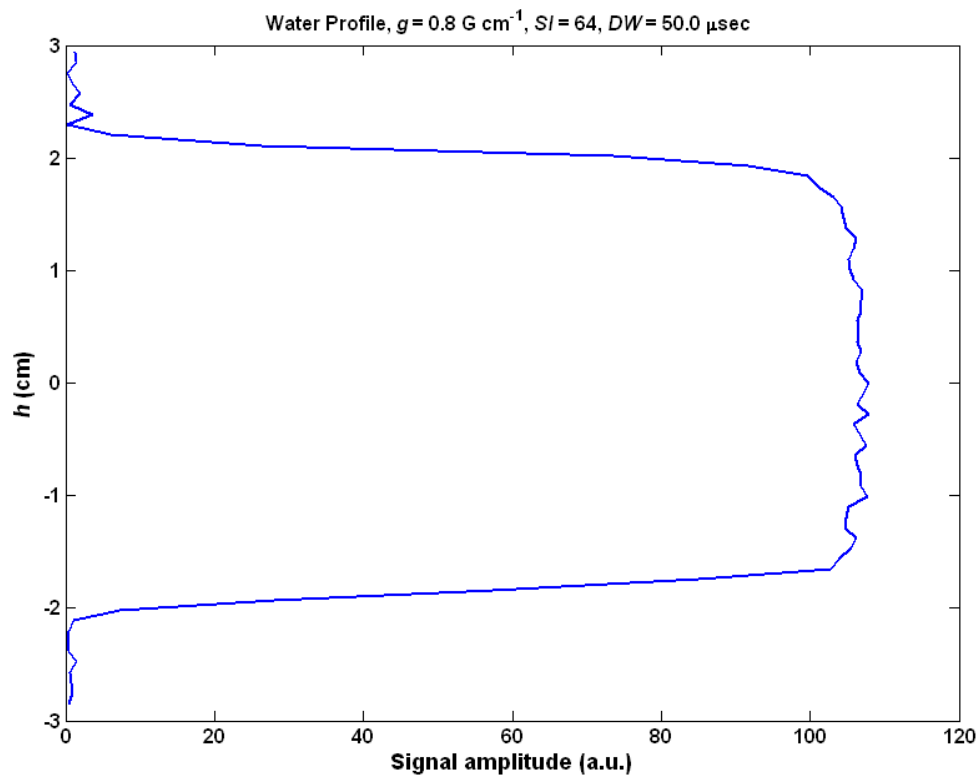


Figure 2.16: Dwell time selected so that the sample plus an excess of about half a centimeter above and below the sample is measured. All other parameters remain the same as the profile depicted in Figure 2.15.

2.5.4 Number of Acquisition Points

The number of acquisition point (SI) is also a vital parameter for spatial resolution of a profiling measurement. While DW determined the range of frequencies resolved, SI governs the number of points spanning that range. Therefore, the product of SI and DW directly impact image resolution.

$$resolution \left[\frac{\text{points}}{\text{cm}} \right] = \frac{SI}{h_s + h_\epsilon} \quad (2.18)$$

$$(h_s + h_\epsilon) = \frac{2\pi}{\gamma g DW} \quad (2.19)$$

$$resolution \left[\frac{\text{points}}{\text{cm}} \right] = \frac{\gamma g DW SI}{2\pi} \quad (2.20)$$

However, acquisition must occur under a gradient and is therefore limited by the readout gradient duration (δ_2). Therefore, the duration of the gradient pulse must be greater than or equaled to the product of SI and DW . Increasing the gradient duration to accommodate more points will increase resolution at the cost of greater attenuation due to diffusion.

$$\delta_2 \geq SI DW \quad (2.21)$$

Furthermore, it is desirable to keep SI as a power of 2 (i.e., 2^n where n is an integer) because the FFT algorithm is fastest for powers of 2.

$$SI = 2^n \quad (2.22)$$

By collecting as many points as possible equation (2. 21) can be rearranged to give

$$SI = \frac{2\delta_1}{DW} \quad (2.23)$$

Combining equations (2. 22) and (2. 23) yields

$$2^n = \frac{2\delta_1}{DW} \quad (2.24)$$

Taking the logarithm of equation (2. 24) allows for one to solve for which power of 2 will be used to determine SI .

$$n \ln(2) = \ln\left(\frac{2\delta_1}{DW}\right) \quad (2.25)$$

Solving for n yields equation (2. 26).

$$n = \text{INT} \left[\frac{\ln\left(\frac{2\delta_1}{DW}\right)}{\ln(2)} \right] \quad (2.26)$$

The operation $\text{INT}(x)$ rounds the value x down to the nearest integer. Rounding the value down ensures that equation (2. 21) is satisfied. Therefore, SI can be expressed as

$$SI = 2^{\text{INT} \left[\frac{\ln\left(\frac{2\delta_1}{DW}\right)}{\ln(2)} \right]} \quad (2.27)$$

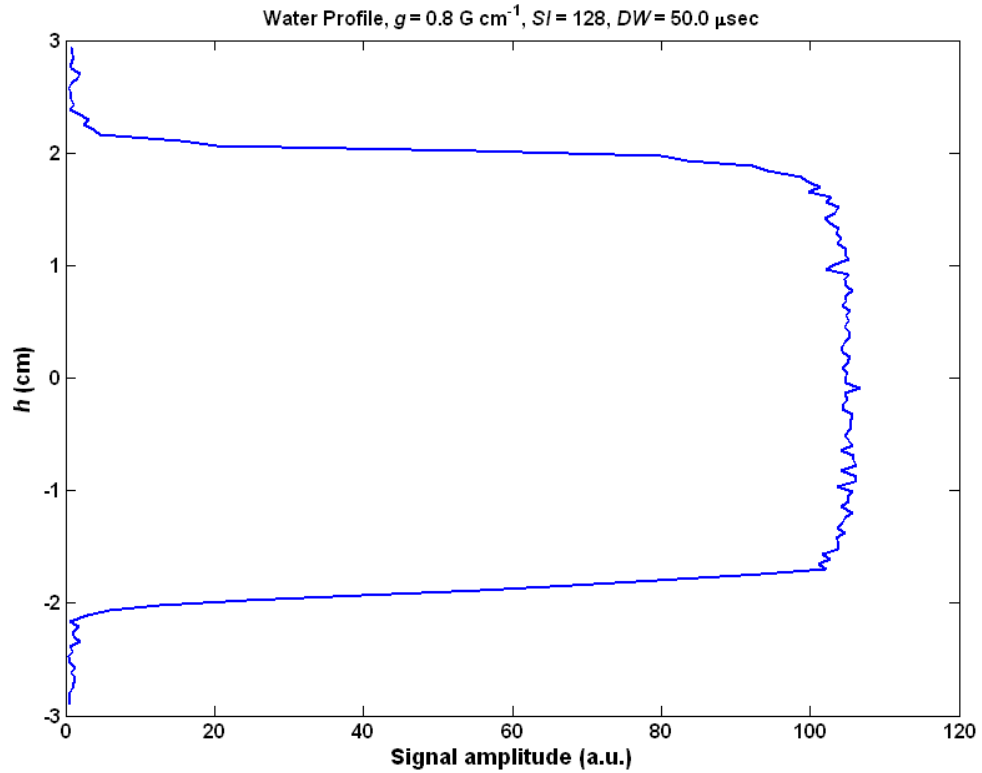


Figure 2.17: Increasing SI increases the resolution of the profile. The only parameter changed from Figure 2.16 to this figure is SI from 64 (Figure 2.16) to 128 (above). Resolution has been increased from $2.2 \text{ points cm}^{-1}$ (Figure 2.16) to $4.4 \text{ points cm}^{-1}$ (above).

2.5.5 Selection Criteria

Various parameters can affect the results of a RARE experiment. For instance, the gradient pulse strength (g) and durations (δ_1 , δ_2) influence the attenuation due to diffusion while SI and DW dictate the measurement's resolution. In order to best select experimental parameters, understanding how these parameters will affect the experiments results is necessary.

The equation below describes the signal attenuation due to both diffusion and relaxation. $T_2^\#$ is the effective transverse relaxation time of the RARE experiment which includes signal attenuation due to diffusion sensitivity caused by the imaging gradient pulses.

$$\exp\left(\frac{-t}{T_2^\#}\right) = \exp\left(-D\gamma^2 g^2 \delta_1^2 \left(2(n-1)\tau + \Delta_1 - \frac{(n-1)}{3}\delta_2\right)\right) \exp\left(\frac{-t}{T_2}\right) \quad (2.28)$$

The above equation is only valid for the case where $g = g_1 = g_2$ and $2\delta_1 = \delta_2$. Equation (2.28) can be rearranged to show the contribution due to diffusion.

$$\frac{1}{T_2} - \frac{1}{T_2^\#} = \frac{-D\gamma^2 g^2 \delta_1^2}{t} \left(2(n-1)\tau + \Delta_1 - \frac{(n-1)}{3}\delta_2\right) \quad (2.29)$$

Since $t = 2n\tau$, this can be rewritten as

$$\frac{1}{T_2} - \frac{1}{T_2^\#} = -D\gamma^2 g^2 \delta_1^2 \left(\frac{2(n-1)\tau}{2n\tau} + \frac{\Delta_1}{2n\tau} - \frac{(n-1)}{3(2n\tau)}\delta_2\right) \quad (2.30)$$

As n , or the number of echoes, becomes larger, $(n-1)/n$ will approach unity and $\Delta_1/(2n\tau)$ will tend to zero since $1/n$ approaches zero as n tends to infinity. Therefore, the difference between the relaxation rates can be estimated by

$$\frac{1}{T_2} - \frac{1}{T_2^\#} \approx -D\gamma^2 g^2 \delta_1^2 \left(1 - \frac{\delta_1}{3\tau}\right), \quad n \rightarrow \infty \quad (2.31)$$

Therefore the ratio of $T_2^\#$ to T_2 can be expressed as

$$\frac{T_2^\#}{T_2} = \left[1 + D\gamma^2 g^2 \delta_1^2 \left(1 - \frac{\delta_1}{3\tau} \right) \right]^{-1}, \quad n \rightarrow \infty \quad (2.32)$$

However, when selecting parameters for the RARE sequence, image resolution must also be taken into consideration. Image resolution also depends on the gradients strength, in addition to the dwell time (DW) and number of acquisition points (SI).

$$resolution \left[\frac{\text{points}}{\text{cm}} \right] = \frac{\gamma g DW SI}{2\pi} \quad (2.33)$$

For a given g , the maximum resolution occurs when data is acquired during the entire readout gradient or

$$2\delta_1 = SI DW \quad (2.34)$$

Substituting equation (2.34) into equation (2.33) demonstrates that resolution is also a function of g and δ_1 .

$$resolution \left[\frac{\text{points}}{\text{cm}} \right] = \frac{\gamma g \delta_1}{\pi} \quad (2.35)$$

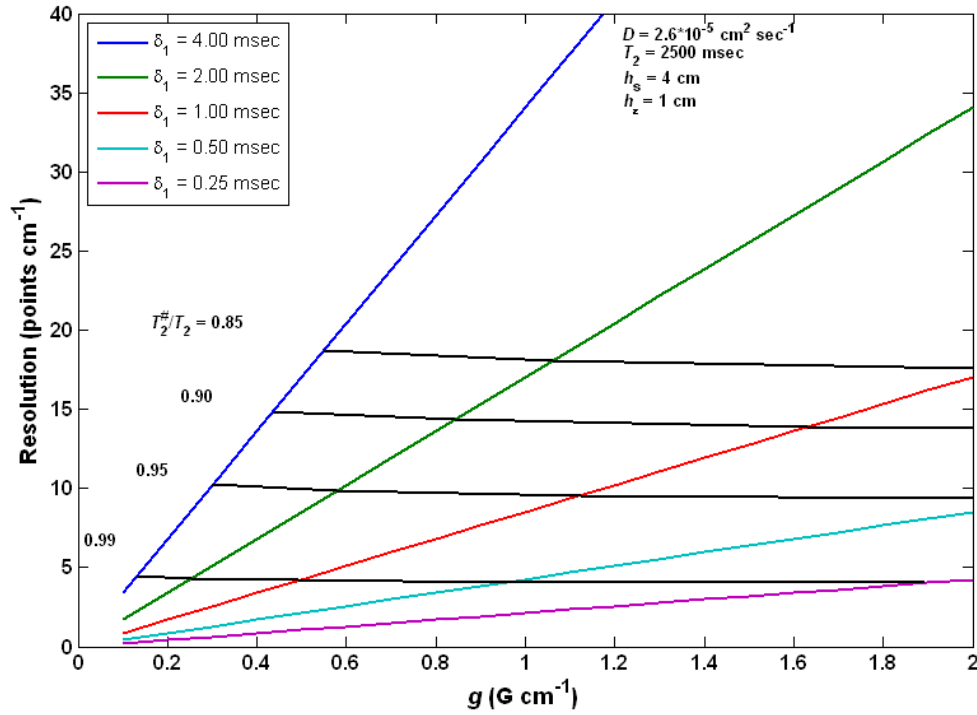


Figure 2.18: Measurement Resolution based on equation (2. 35).

Figure 2.18 shows the resolution as function of g and δ_1 (equation (2. 35)). Also plotted on the graph are lines of constant $(T_2^\# / T_2)$. For these calculations, τ was chosen so that there would be 1 millisecond between the end of a gradient pulse and the subsequent RF pulse (equation (2. 36)). For a low strength gradient, a 1 msec spacing between the gradient and RF pulses will prevent overlap of the pulses.

$$\tau = \delta_1 + 1 \text{ msec} \quad (2. 36)$$

Figure 2.18 demonstrates that for a given $T_2^\# / T_2$, the corresponding image resolution changes only slightly. Therefore, by selecting an acceptable amount of attenuation due to diffusion, the image resolution is set, and a tradeoff between resolution and $T_2^\# / T_2$ ensues. For example, if it is desired to have $T_2^\# / T_2 = 0.95$ for a 4 cm water sample, then the

resulting image will have a resolution of about 9 points cm^{-1} . In order to generate a higher resolution image, the RARE signal will undergo more attenuation due to diffusion.

By selecting the $T_2^\# / T_2$, possible g and δ_1 pairs can be determined. These pairs correspond to the lines of constant $T_2^\# / T_2$ in Figure 2.18. However, not all of the gradient strengths (g) can be used to produce meaningful profiles; a minimum and maximum gradient strength exist for each measurement

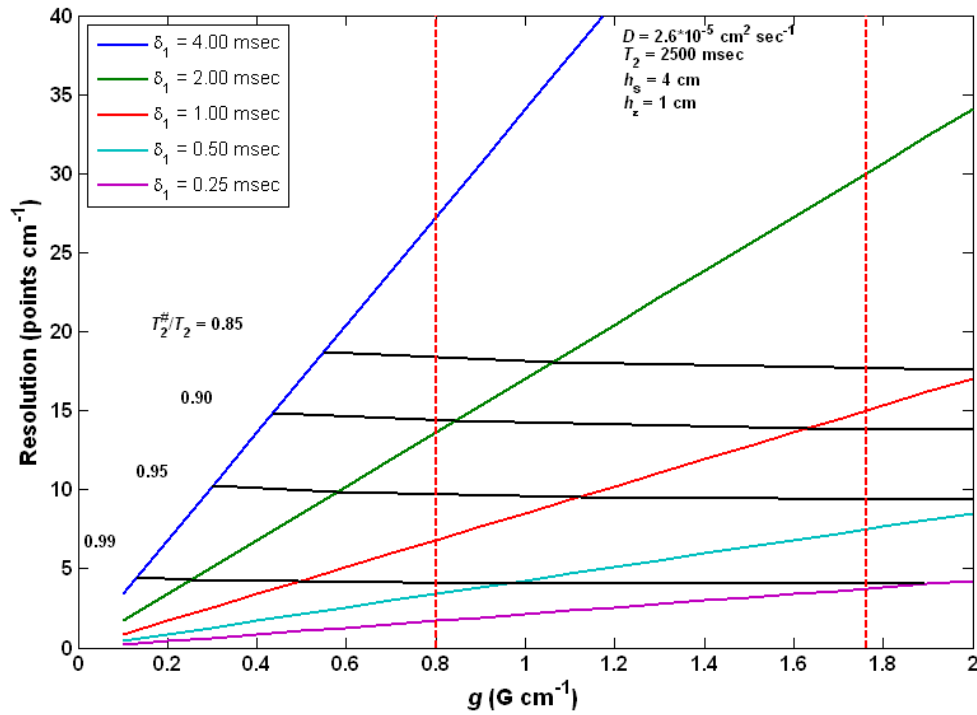


Figure 2.19: Measurement Resolution based on equation (2. 35) with g_{\min} and g_{\max} denoted by the red, vertical dashed lines

g_{\min} and g_{\max} , introduced in section 2.5.2, can be added to the resolution plot and subsequently, limits the range of possible g and δ_1 (Figure 2.19). However, a broad range of g and δ_1 pairs still exists for a given $T_2^\# / T_2$. The minimum T_2 value to be resolved for

the measurement can be used in selecting only a single pair. Since the gradient pulses are between the π -pulses, the echo spacing is limited by the gradient duration.

$$\delta_1 < \tau \quad (2.37)$$

However, the echoes must be spaced close enough in order to resolve the fast relaxing components.

$$2\delta_1 < 2\tau \ll \min(T_2) \quad (2.38)$$

If a minimum ratio between echo spacing and $\min(T_2)$ is established, a relationship between δ_1 and $\min(T_2)$ can be constructed using equation (2.36) and (2.38). Equation (2.39) represents an arbitrary ratio between δ_1 and $\min(T_2)$.

$$\frac{2\tau_{max}}{\min(T_2)} < \frac{1}{10} \quad (2.39)$$

Combining equations (2.38) and (2.39),

$$2\delta_1 < 2\tau_{max} < \frac{1}{10} \min(T_2) \quad (2.40)$$

Substituting equation (2.36) into (2.40),

$$\delta_1 < \frac{1}{20} \min(T_2) - 1 \text{ msec} \quad (2.41)$$

Using the largest δ_1 will allow for the longest echo train, and subsequently the broadest resolution of relaxation times. Therefore, equation (2.42) is used as the relationship between the minimum T_2 and the gradient duration.

$$\delta_1 = \frac{1}{20} \min(T_2) - 1 \text{ msec} \quad (2.42)$$

With a $T_2^\# / T_2$ selected, use of equation (2.42) should yield a suitable g and δ_1 pair. If, however, this pair lies outside the bounds set by the g_{\max} and g_{\min} lines, then the selected g and δ_1 pair will correspond to the intersection of the $T_2^\# / T_2$ curve and the nearest vertical bound (either g_{\max} or g_{\min}). Similarly if equation (2.42) produces a negative value, then the g and δ_1 pair will correspond to the intersection of the $T_2^\# / T_2$ curve and the g_{\min} line. In this situation, the fastest relaxing components may not be well resolved. Choosing a value of $T_2^\# / T_2$ closer to unity should produce a better measurement of the fastest relaxation times (image resolution should be reduced). Figure 2.20 shows the selected g and δ_1 pair for a water sample.

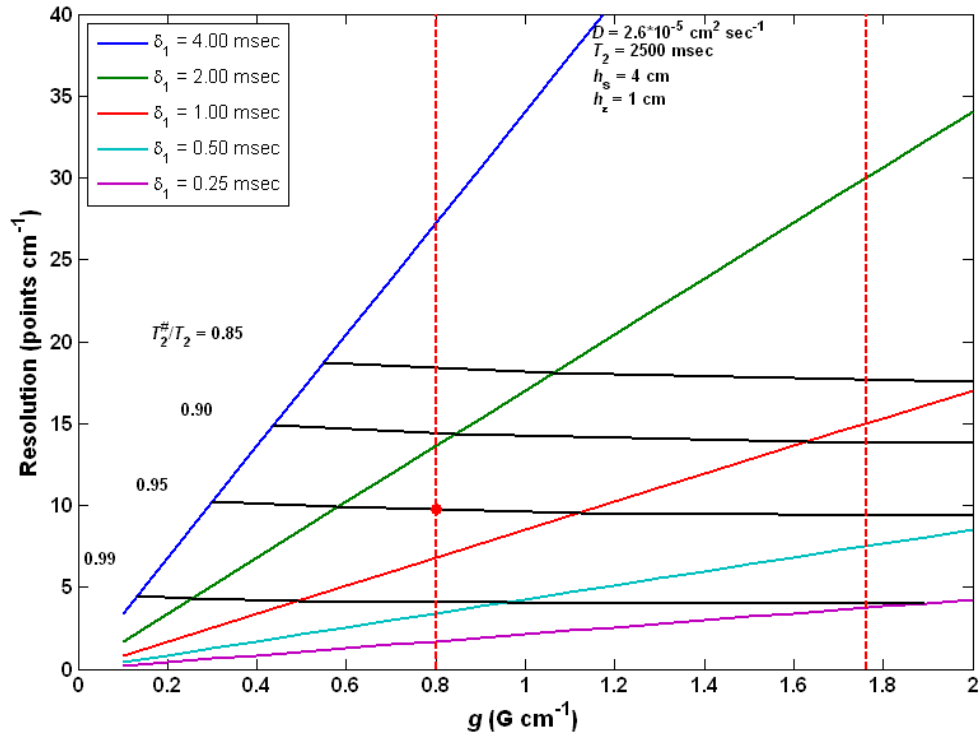


Figure 2.20: Measurement resolution based on equation (2. 17) with g_{\min} and g_{\max} denoted by the red, vertical dashed lines. Red dot corresponds to selected g and δ_1 pair ($g = 0.80 \text{ G cm}^{-1}$, $\delta_1 = 1.43 \text{ msec}$).

Once a g and δ_1 pair have been selected, DW and SI can be determined using equations (2. 17), (2. 27), and (2. 34). Collection should occur for the entire duration of the rephrasing pulse (equation (2. 34)), and SI should remain an integer power of 2 (equation (2. 27)). Presented below are plots for SI and DW corresponding to $\delta_1 = 1.43 \text{ msec}$. The red dot indicates the appropriate choice for SI and DW .

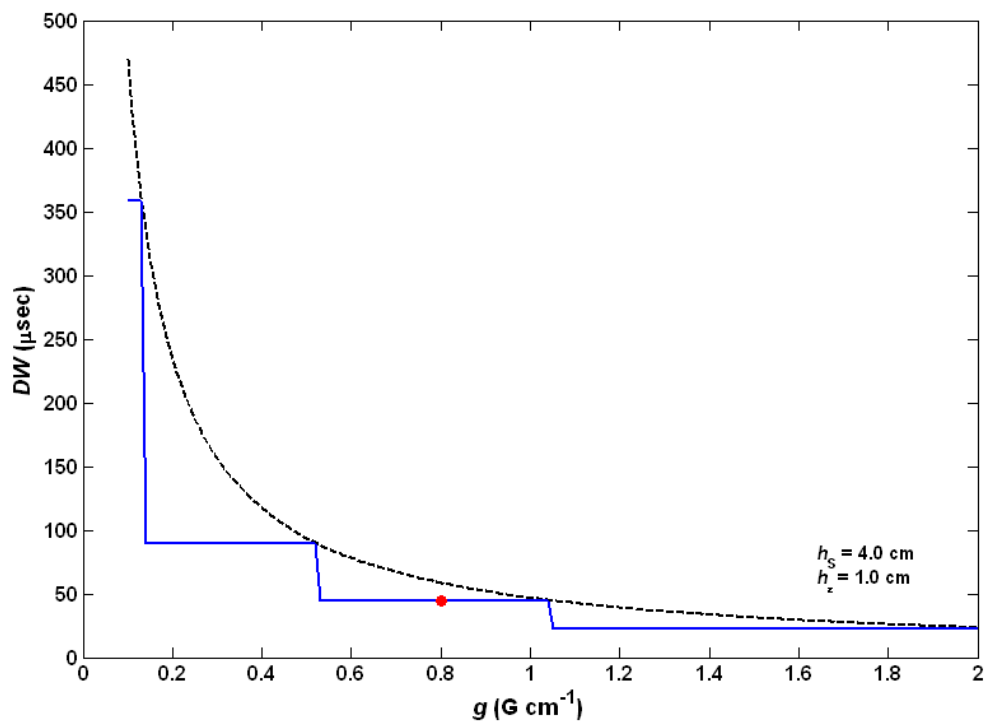


Figure 2.21: Dwell time as a function of g for $\delta_1 = 1.43$ msec. The dashed line represents the maximum DW determined by g , h_s , and h_e .

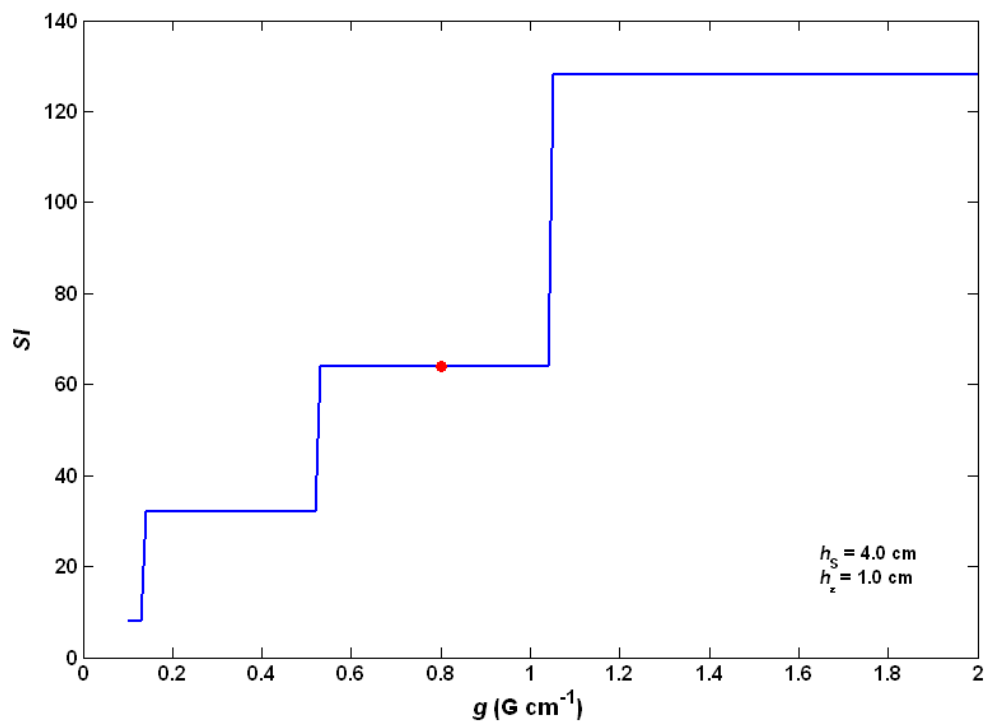


Figure 2.22: SI as a function of g for $\delta_1 = 1.43$ msec.

2.6 Data Processing

Data generated from a RARE experiment requires slightly more processing than required for a standard CPMG measurement. The first step is to apply a direct FFT reconstruction (Liang & Lauterbur, 2000) to the two channel data of each echo individually. The frequency scale can then be converted to a length by applying equation (2.3). The application of the FFT yields both a real and imaginary signal (Figure 2.23, left). The imaginary portion of the profile can be removed by rotating the data. Axis rotation is performed using the transformed data of all the echoes at a single height or frequency. For instance, transformed data at $h = 0.0$ cm taken from all 1024 echoes of an experiment performed on 3 cm water sample can be plotted and rotated as shown in Figure 2.24. After rotation, the real portion of the data represents the profile while the imaginary portion is a measure of the noise (Figure 2.23, right). Now, the profiles can then be modified by means of applying a weighted average to help smoothen out their plateaus. This is discussed in the next section.

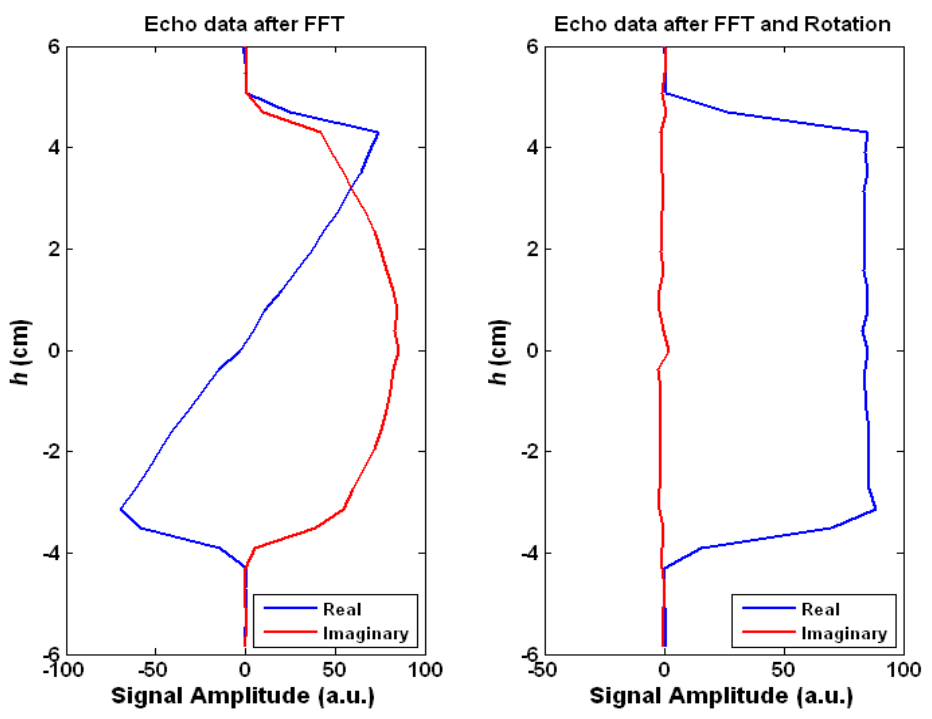


Figure 2.23: First echo acquired during a RARE experiment on a water sample after application of FFT. Data is presented before (left) and after (right) rotation.

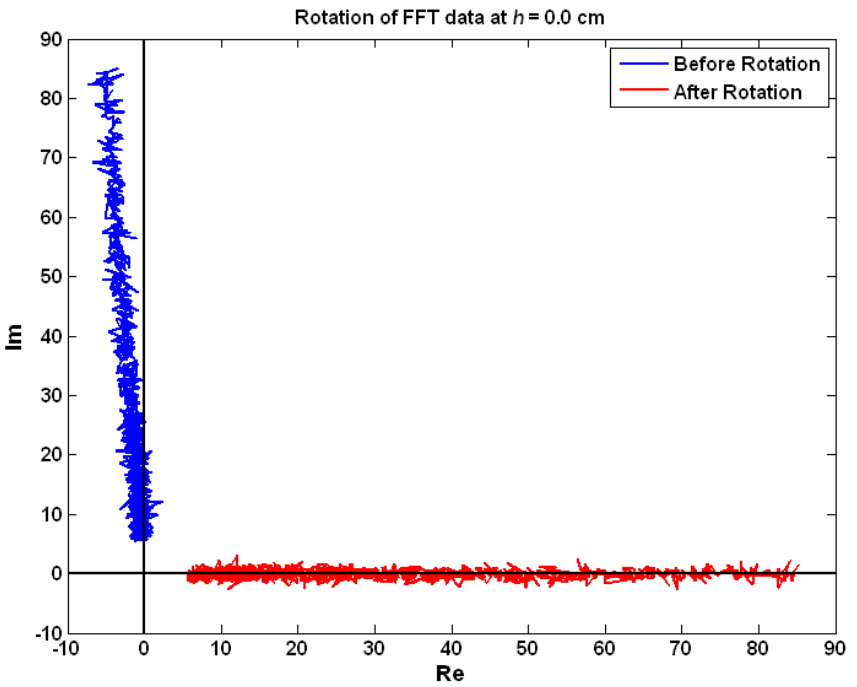


Figure 2.24: Rotation of FFT data for a RARE experiment on a water sample at $h = 0.0$ cm

Finally, the data is ready to be inverted (Chuah, 1996). The profile data at each height is inverted in order to determine a T_2 distribution at that position. For these experiments, the full form of the attenuation equation, equation (2. 28), was not used. Instead, the diffusion kernel is neglected and an effective relaxation, $T_2^\#$, is determined. Proper parameter selection is necessary in order to reduce the effect of attenuation due to diffusion. A common regularization parameter, α , is used throughout the system during inversion. Once the inversion has been performed at each position, the results can be combined into a T_2 map for the measured sample.

2.6.1 Profile Averaging

The profiles collected via the RARE sequence for bulk fluids have consistently demonstrated a noisy plateau. In order to reduce the noise, a 3-point weighted average is implemented.

$$\bar{S}(x_i) = w_1 S(x_{i-1}) + w_2 S(x_i) + w_3 S(x_{i+1}) \quad (2. 43)$$

Where $S(x_i)$ is the signal amplitude at the height x_i , $\bar{S}(x_i)$ is the weighted signal average and w_i are the weights used to perform the average. Note that $w_1 + w_2 + w_3 = 1$.

The example below shows this averaging performed on a layered water/squalane system with $w_2 = 0.5$ and $w_1 = w_3 = 0.25$. In the figure below, the points represent the profile data prior to averaging while the lines identify the averaged profiles. The profiles become slightly more rounded at the corners and oil/water interface after the averaging is

performed. This is evident in Figure 2.26 which depicts the profile acquired from the 16th echo.

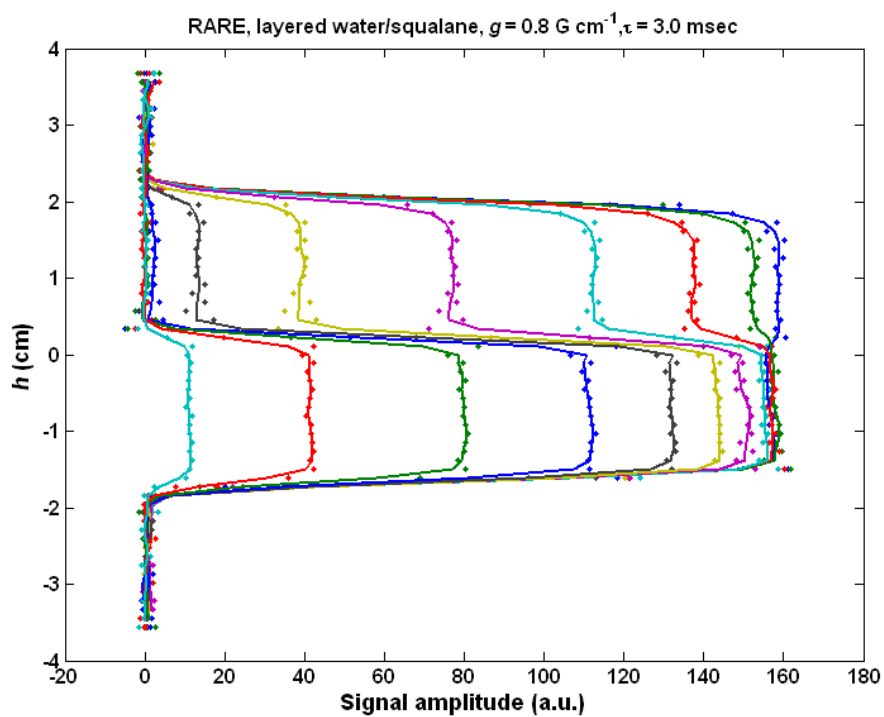


Figure 2.25: RARE profiles of a water/squalane system. The points represent the un-averaged data will the line indicate the profiles after averaging has been performed.

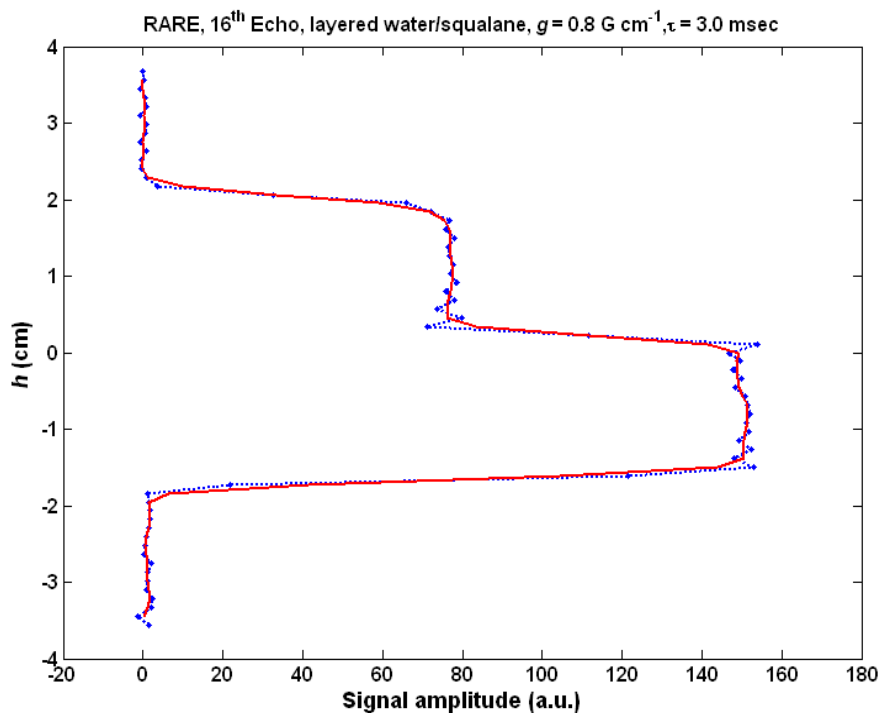


Figure 2.26: RARE profile (16th echo) of a water/squalane system. The blue line corresponds to the profile prior to averaging. The red line indicates the resulting profile after averaging.

T_2 distributions were found from the RARE profiles before and after averaging. Note that for both calculations, the regularization parameters was kept constant ($\alpha = 0.75$). The T_2 profiles presented in Figure 2.27 and Figure 2.28 are generated from the data before and after averaging, respectively. Both profiles show the same basic features. However, the averaged data appears to yield a more consistent T_2 profile over the two phases, especially the oil phase. The oil profile in the un-averaged profile demonstrates a lack of uniformity at higher relaxation times (the right edge, Figure 2.27). Also, the $T_{2,\log\text{mean}}$ demonstrates oscillation in both the water and oil layers. This does not appear to be the case for the averaged profiles (Figure 2.28). Therefore, by applying a weighted average to noisy profiles, T_2 profiles with a greater uniformity can be produced.

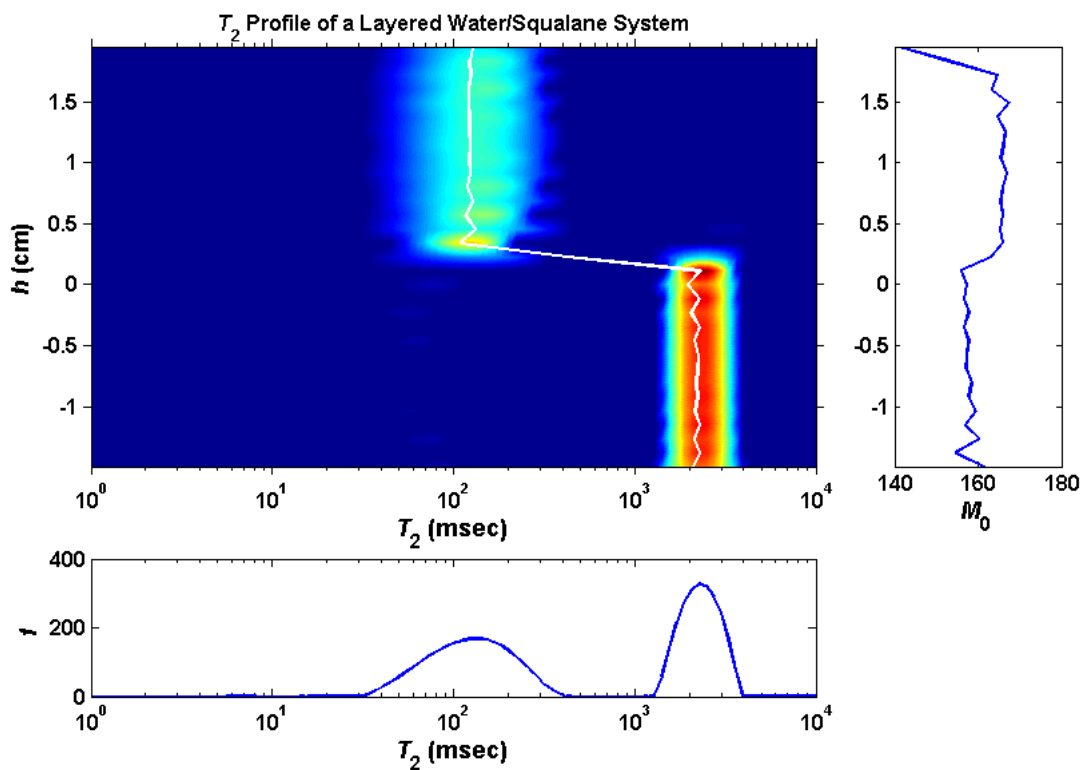


Figure 2.27: T_2 profile of a water/squalane system using the un-averaged data. White line indicates the $T_{2,\log\text{mean}}$.

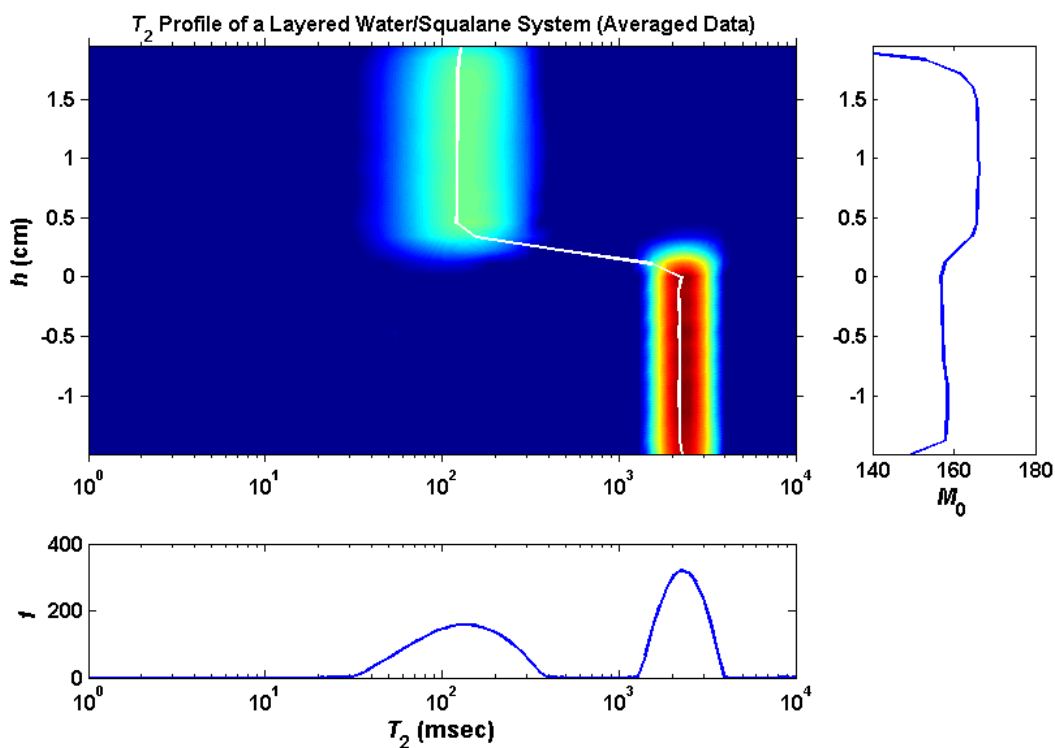


Figure 2.28: T_2 profile of a water/squalane system using the averaged data. White line indicates the $T_{2,\log\text{mean}}$.

2.7 Application

The RARE sequence can be applied to a system in order to generate a map of T_2 distributions as a function of sample position. Figure 2.28 is an example of a T_2 map for a layered water/squalane system. While this is a simplistic system, the two phases are clearly distinguishable in the T_2 map due to their distinct relaxation times. However, RARE can be extended to examine systems with greater heterogeneity.

Core samples can have complex pore structures. Implementation of the RARE sequence yields a greater insight into the core's heterogeneity than the standard CPMG measurement due to the spatial resolution of the imaging experiment. Both CPMG and RARE experiments performed on two different core samples of similar size (1 in. diameter by 1 in. height). The first sample was a Texas Cream Limestone, denoted TCL 80. The results from the CPMG experiment revealed that the core has a bimodal pore distribution, and the RARE experiment confirms this finding as well as showing that the pore distribution remains fairly constant across the height of the sample (Figure 2.29). The results for the second core, a Yates vuggy carbonate denoted D, also revealed a bimodal pore size distribution. However, the RARE results give a much clearer picture of the core sample's heterogeneity. Even though the sample is only 1 inch in diameter and 1 inch in height, Figure 2.31 shows that porosity is not uniform across the core. Additionally, the T_2 profile indicates that the fraction of microporosity appears to fluctuate along the length of the core, but the fraction of macroporosity is the lowest near the top of quarter of the core and then reaches a maximum near the center.

After generating a T_2 map, porosity profiles can be constructed by comparing the RARE profiles of the brine saturated core sample and a bulk brine sample. A profile of

intrinsic magnetization was generated by extrapolating the first 15 profiles for both the rock and brine sample. The brine sample had the same dimensions as the core sample. The porosity was calculated using the equation below. Note the brine's intrinsic magnetization, \bar{M}_{0brine} , and volume corresponding to single profile point, $V_{point\ brine}$, will be constant throughout the sample. Therefore, the denominator of equation (2. 44) takes on a constant value.

$$\phi_{RARE}(x) = \frac{M_{0core}(x) / V_{point\ core}}{\bar{M}_{0brine} / V_{point\ brine}} \quad (2. 44)$$

Figure 2.30 and Figure 2.32 depict the porosity profile for TCL 80 and Yates D, respectively. The porosity obtained from the RARE measurement was compared to the porosity measured gravimetrically as well as the NMR porosity obtained from the intrinsic magnetization of a CPMG experiments. Table 2.2 summarizes these results and illustrates that all three measurement techniques are in very good agreement. Figure 2.30 shows that the TCL 80's porosity doesn't change very much across the sample. However, Figure 2.32 demonstrates that the porosity of the vuggy carbonate is not constant across the sample and varies from about 10% at the top of the core to about 25% near the center even though it is only an inch in height.

Table 2.2: Summary of porosity measurements for TCL 80 and Yates D

	$\phi_{Grav.}$	ϕ_{CPMG}	ϕ_{RARE}
TCL 80	0.245	0.243	0.242
Yates D	0.200	0.200	0.208

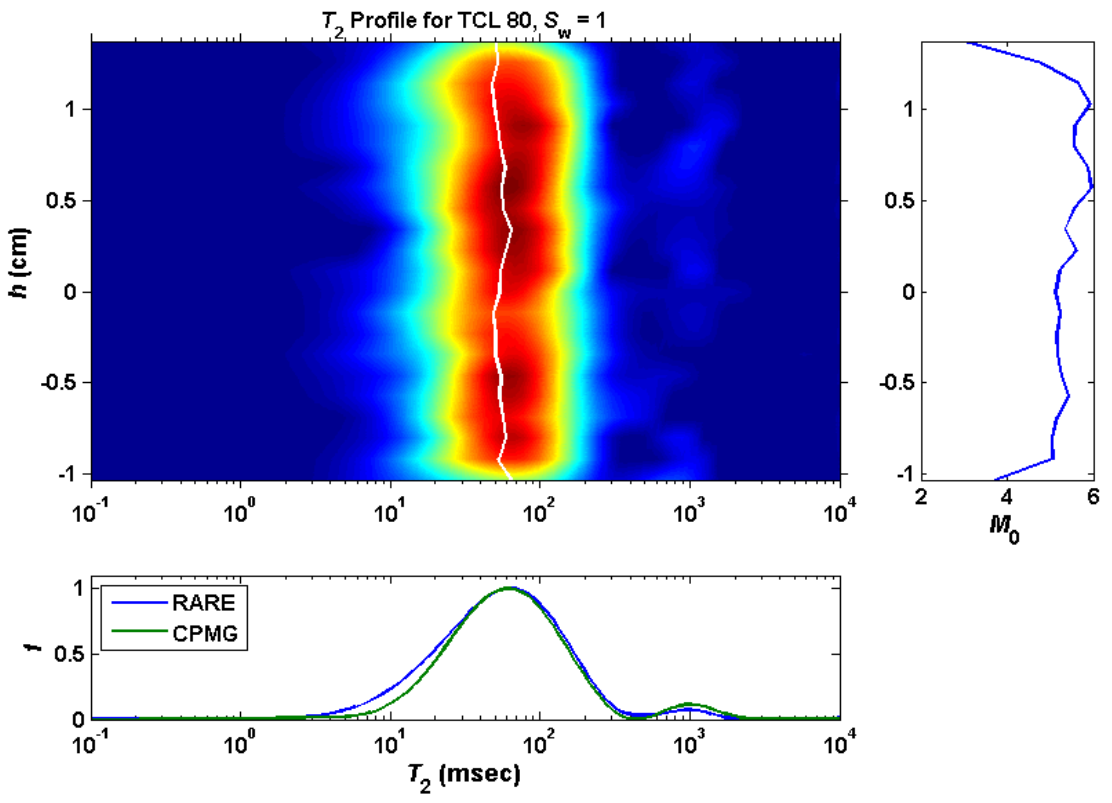


Figure 2.29: T_2 map for TCL 80. The white line indicates the $T_{2, \logmean}$

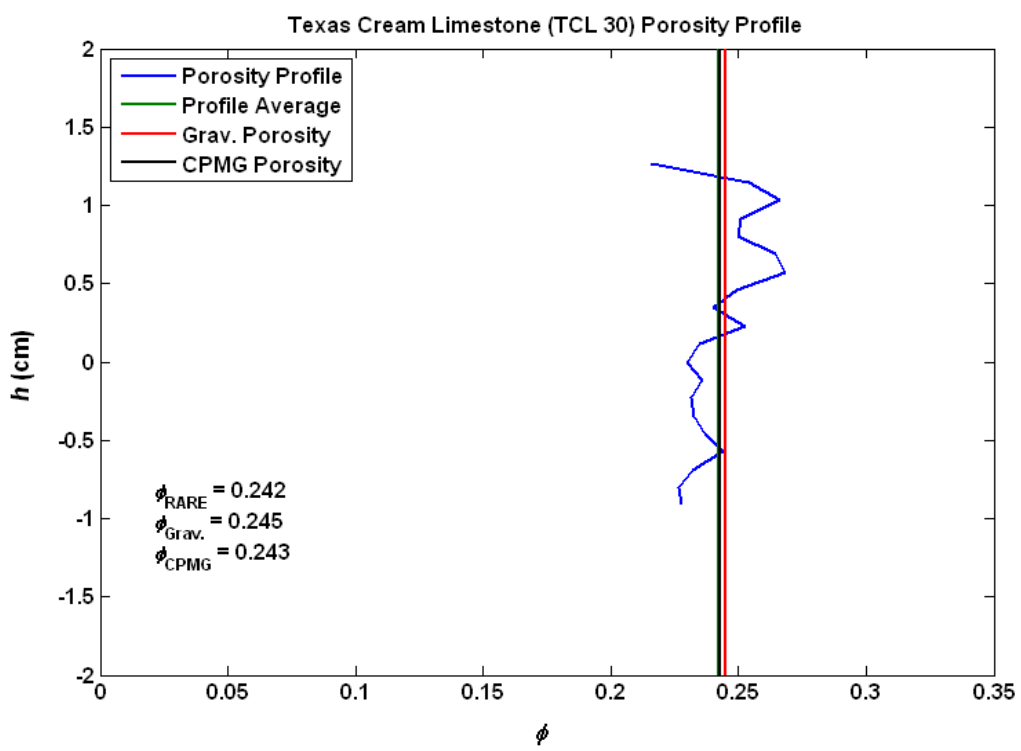


Figure 2.30: Porosity Profile for TCL 80

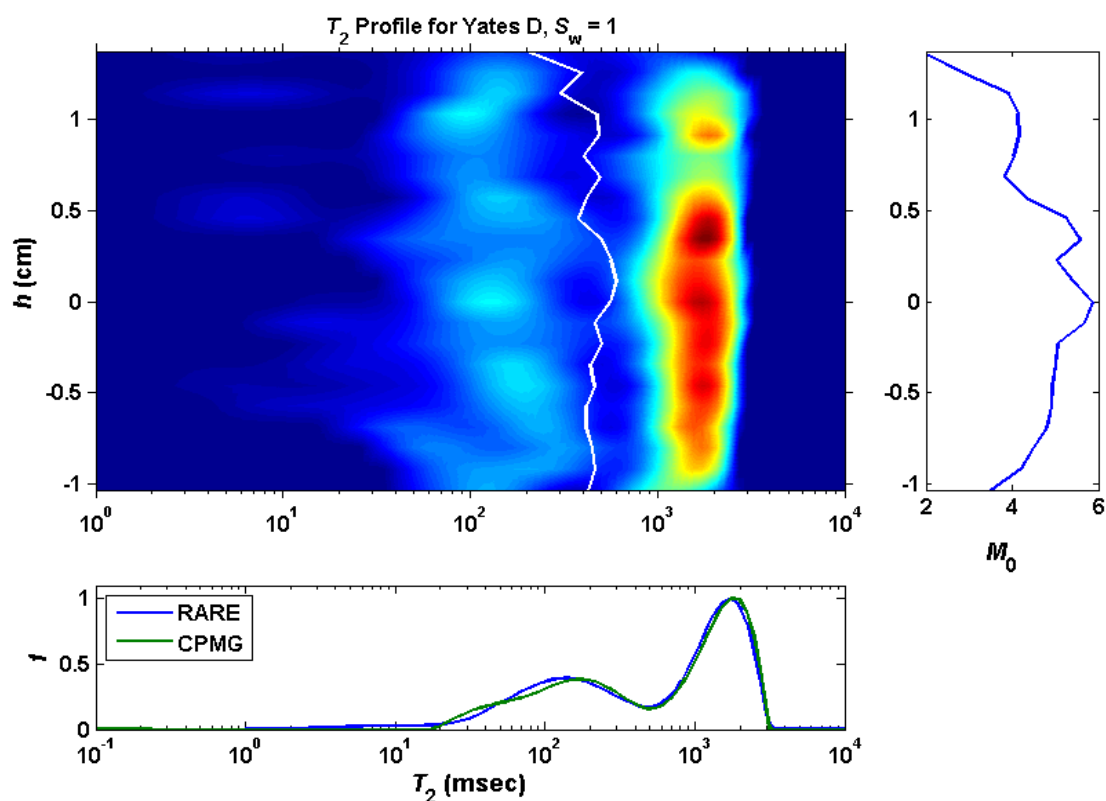


Figure 2.31: T_2 map for Yates D. The white line indicates the $T_{2, \logmean}$

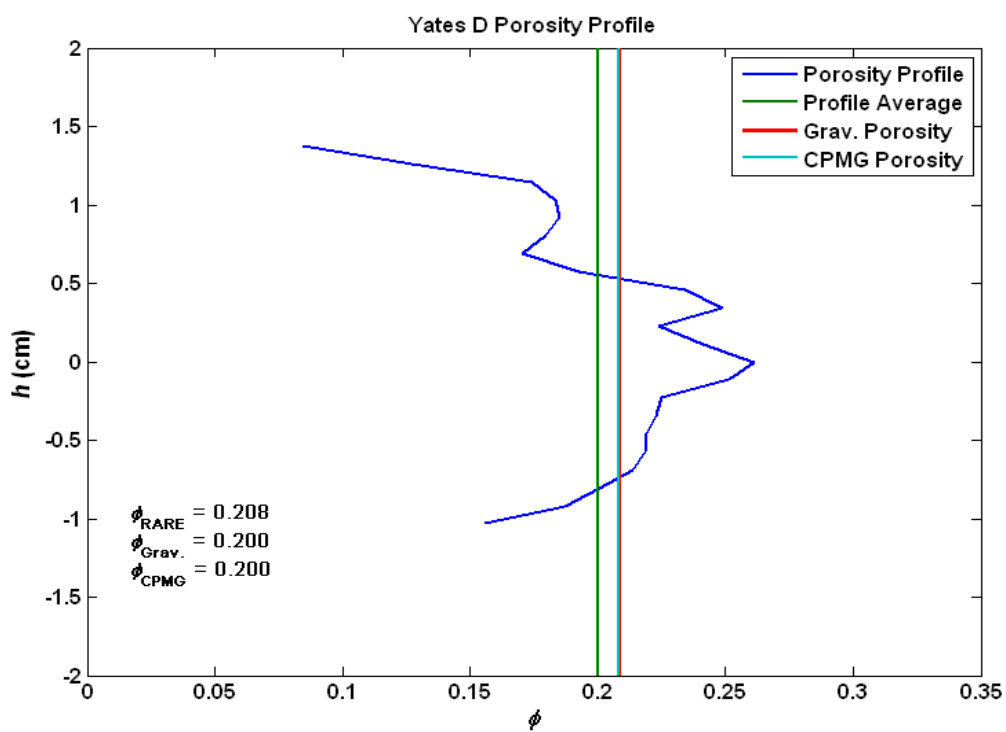


Figure 2.32: Porosity Profile for Yates D

Summary

The application of MRI principles can be applied while using a ultra-low field spectrometer to generate 1-D NMR profiles. Profiling a sample is a valuable tool enabling for the determination of inherent spatial characteristics. When parameters are properly selected, useful information can be extracted from NMR profiles. These parameters include the gradient strength, dwell time, and the number of acquisition points. Proper parameter selection is not straight forward since an interdependence of the parameters exists. The gradient imparts spatial realization upon the measurements, but can also cause attenuation due to diffusion. The proposed method of selecting parameters is based on trying to minimize the attenuation due to diffusion while maximizing the image resolution.

Furthermore, by taking advantage of differing relaxation times within a sample, images with different types of contrast, such as spin-density, T_1 -weighted, and T_2 -weighted, can be generated. By comparing several images which have undergone various amounts of relaxation, T_2 can be calculated as a function of sample position. The rapid acquisition with relaxation enhancement (RARE) pulse sequence can be used to generate multiple profiles each with a different amount of T_2 relaxation. Experiments have been performed with Texas Cream Limestone and vuggy Yates core samples. The resulting T_2 map indicates the lack of heterogeneity with Texas Cream core, but slight heterogeneity within the Yates core sample. With the Yates core, a region of low macroporosity is noted near the top of the core. Furthermore, a porosity profile can be constructed from the T_2 map. For each of the core samples, the resulting porosity profiles were in good agreement with the average values obtained gravimetrically and via CPMG.

Chapter 3

D-T₂ Profiling

Diffusion-Weighted Imaging is a MRI technique used most successfully in clinical settings to identify regions of poor blood flow in the brain (Le Bihan, Poupon, Amadon, & Lethimonnier, 2006). However, it has the potential to be applied to porous media. Combining diffusion-weighted imaging with a sequence like RARE leads to an imaging analogue of diffusion editing. Diffusion editing has proven extremely useful in identifying saturating fluids in porous media when exhibit overlapping T_2 distributions and identifying (Freedman, Heaton, Flaum, Hirasaki, & Hürlimann, 2003) (Hürlimann, Flaum, Venkataramanan, Flaum, Freedman, & Hirasaki, 2003) (Flaum, Chen, & Hirasaki, 2004). In this chapter, a new NMR pulse sequence is presented which combines imaging and diffusion editing allowing for the ability to distinguish fluids based upon their self-diffusion coefficients.

3.1 Development of the Pulse Sequence

Two different pulse sequences have been developed in an effort to measure D - T_2 distribution. One, CPMG – DE, relies on the application of pseudostatic gradient throughout the experiment (Flaum, Chen, & Hirasaki, 2004) and subsequently, there is no way to incorporate frequency-encoding gradient pulses. The other method, PFG – DE, uses two gradient pulses prior to the formation of a stimulated echo in order to make the measurement sensitive to diffusion (Hürlimann & Venkataramanan, 2002) (Flaum, Hirasaki, Flaum, & Straley, 2005). Since the gradient is not being applied constantly, additional pulses can be included in the sequence in order to make the measurement sensitive to position. Therefore, the PFG – DE sequence will be used as a starting point for creating an imaging analogue to diffusion editing. Such pulse sequences have been used before. Merboldt et al. (1985) used a stimulated echo imaging sequence to measure the diffusion coefficients of aqueous solutions of CuSO_4 and poly(ethyleneglycol). Scheenen et al. (2000) used a pulse sequence denoted as the Pulse Field Gradient STimulated Echo Turbo Spin Echo (PFG STE TSE) to measure the apparent diffusion coefficient of water in maize plant stem as well as the flow of water through a tomato pedicel.

Presented in Figure 3.1 is the final design for the D - T_2 profiling pulse sequence. The need for specific structural components, such as the bipolar gradient pulses and placement of imaging gradients, will be discussed in the following sections.

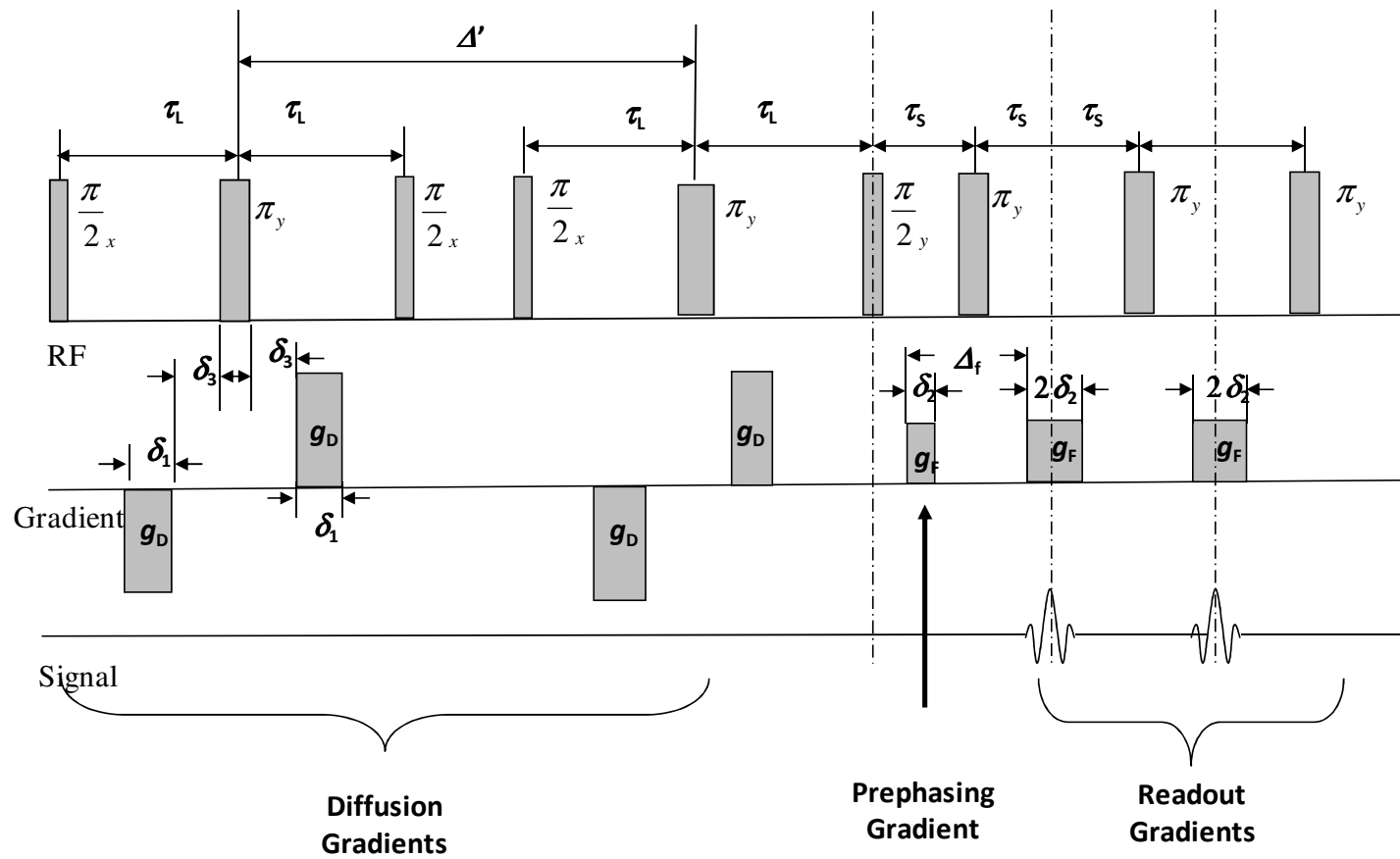


Figure 3.1: $D-T_2$ profiling pulse sequence

3.1.1 Gradient Pulse Structure and Echo Stability

Prior to introducing any type of profiling capabilities into a diffusion measurement, a pulse sequence that produces a broad, reproducible echo must be selected. If the selected sequence yields a poorly shaped echo, it cannot be expected to yield a meaningful profile. Therefore, two gradient pulse structures were investigated. The first was a unipolar gradient structure common to most pulsed field gradient diffusion measurements and is depicted in Figure 3.2. Squalane was measured using $\Delta = 60$ msec, $\delta = 3$ msec, $g = 20$ G cm⁻¹, $RD = 1$ sec, $NS = 64$. This experiment was repeated several times with a one minute wait time between each run. The resulting echo shows some oscillatory behavior indicating that echo is refocusing under a residual gradient. Furthermore, after repeated application the signal continued to deteriorate.

Next, the use of a bipolar gradient pulse structure was analyzed. Bipolar gradients can help reduce the effect of background gradients and gradients generated from residual eddy currents (Cotts, Hoch, Sun, & Markert, 1989). The pulse sequence is shown in Figure 3.3. The same type of experiments performed with the unipolar gradient pulses is repeated using bipolar pulses. The echo forms as expected. It is broad with no oscillatory behavior and one channel is even and the other odd. Furthermore, after repetition, the echo shows only slight changes from the initial experiment. Therefore, the bipolar gradient structure will be implemented for the measurement of diffusion coefficients.

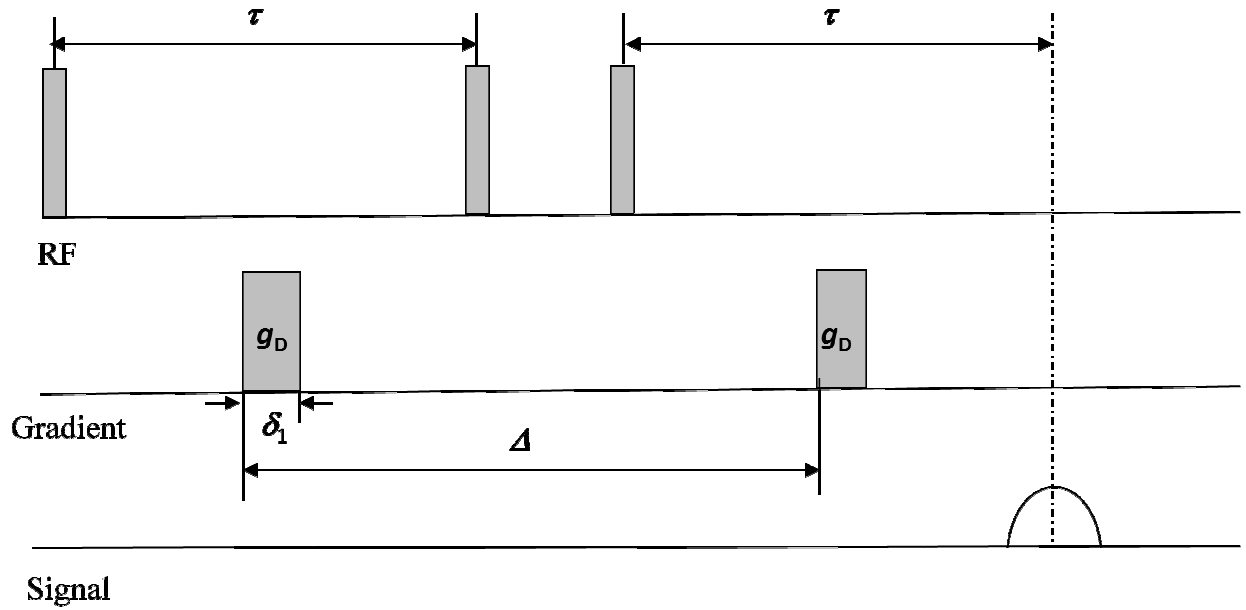


Figure 3.2: Unipolar pulsed field gradient stimulated echo pulse diagram (Tanner, 1970)

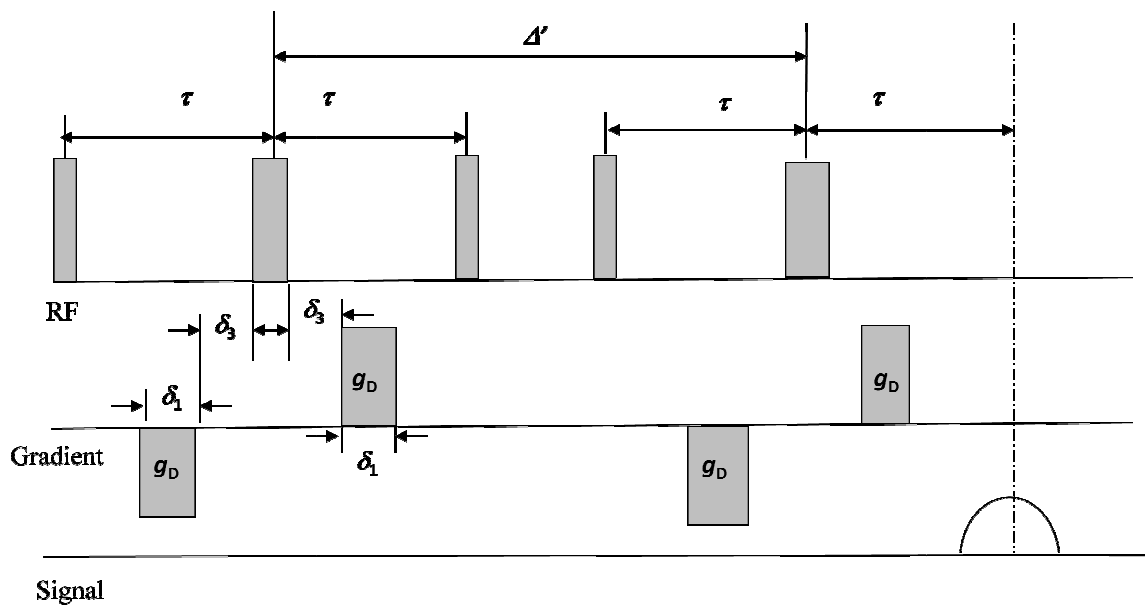


Figure 3.3: Bipolar pulsed field gradient stimulated echo pulse diagram (Cotts, Hoch, Sun, & Markert, 1989)

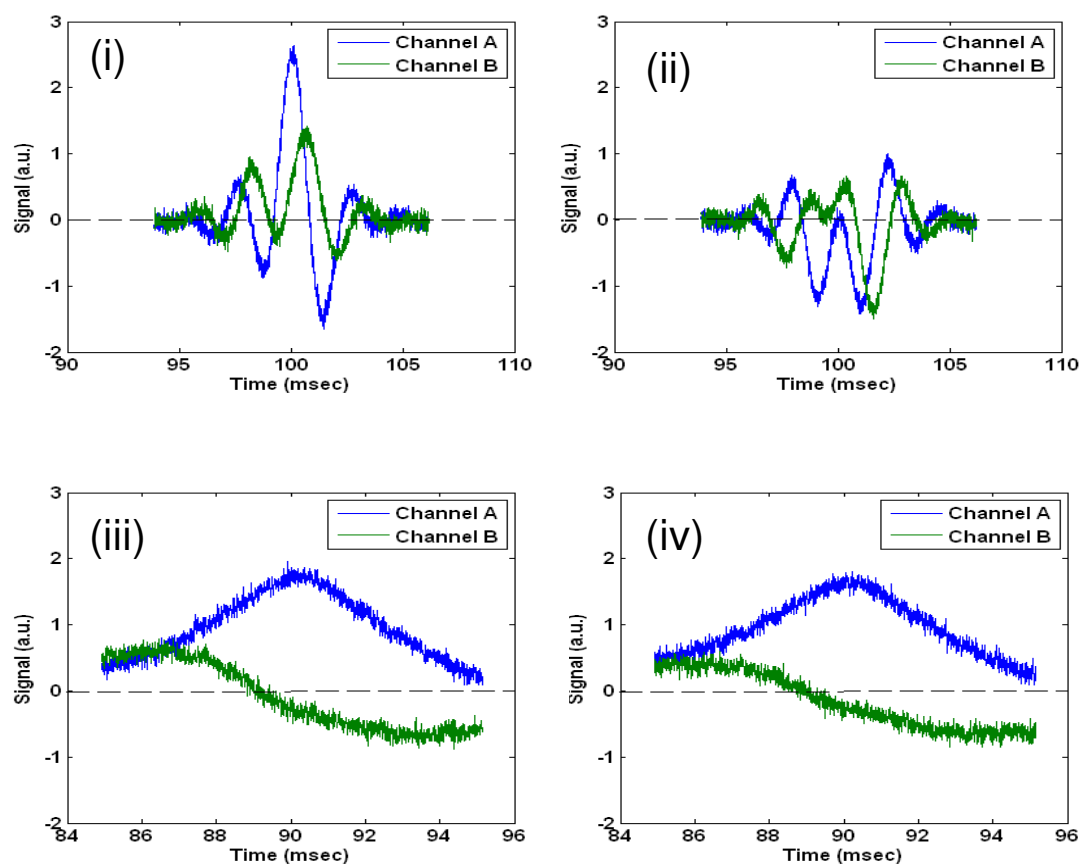


Figure 3.4: : Effect of Unipolar vs. Bipolar Gradient Pulses in a Stimulated Echo Diffusion Sequence. $\Delta = 60$ msec, $\delta = 3$ msec, $g = 20$ G cm⁻¹, $RD = 1$ sec, $NS = 64$, 1 min. wait between experiments. (i) Unipolar Pulses, 1st experiment, (ii) Unipolar Pulses, 4th experiment, (iii) Bipolar Pulses, 1st experiment, (iv) Bipolar Pulses, 4th experiment

3.1.2 Increasing Pulse Sequence Phase Stability

The presence of large diffusion gradient pulses in an imaging pulse sequence often leads to phase errors. CPMG phase stability requirements necessitate the need for an equivalent degree of dephasing of a spin isochromat between successive refocusing pulses (Bernstein, King, & Zhou, 2004). Phase errors can result from the random motion of the spins under strong magnetic field gradients, and the simplest way to counter this problem is to require that all refocusing pulses be tuned to 180° (Alsop, 1997). Therefore, the first attempt at creating D - T_2 profiling pulse (Figure 3.5) sequence tried to capitalize on this fact. However, large fluctuations were still noted in FFT phase data (Figure 3.6). These fluctuations most likely stem from the application of strong gradients and the presence of refocusing pulses that are not tuned exactly to 180° . Even small deviations in the refocusing pulse can cause phase errors (Alsop, 1997). Direct and stimulated echoes form via different coherence pathways. In the presence of a strong magnetic field gradient and imperfect R.F. pulses, the direct and stimulated echoes will refocus at the same time but with different phases (Bernstein, King, & Zhou, 2004) causing these echoes to combine destructively resulting in an oscillatory echo decay (Alsop, 1997). This phase instability manifests itself as movement of the echo within the acquisition window and large fluctuations of the phase angle in the analysis of the FFT quadrature data (Figure 3.6).

In order to create a pulse sequence with greater phase stability, two steps were taken: the separation of the diffusion and imaging sections (Norris et. al, 1992) and the inclusion of a $(\pi/2)_y$ pulse during the formation of the peak of the first echo (Alsop,

1997). Separating the diffusion and imaging sections allows us to deal with phase instability then proceed in collecting T_2 and imaging data. However, by doing so, data collection is delayed resulting in loss of more T_2 data. Then, by applying a $(\pi/2)_y$ pulse during the formation of the first echo's peak, the out of phase component of magnetization will be tipped onto the longitudinal axis leaving behind the in-phase signal in the transverse plane (Figure 3.6).

The results before and after the separation of the diffusion and imaging sections of the sequence and the inclusion of a $(\pi/2)_y$ during the formation of the first echo are presented in Figure 3.6. Prior to this modification, the first and second echoes do not form in exactly the same position within the acquisition mode (Figure 3.6, (i)). Additionally, FFT quadrature data (Figure 3.6, (iii)) demonstrates very large phase oscillations. However, after modifying the pulse sequence, phase stability has been improved vastly. The first and second echoes occur in the same position within the acquisition window (Figure 3.6, (ii)), and the large oscillations noted in the FFT quadrature data have been damped (Figure 3.6, (iv)).

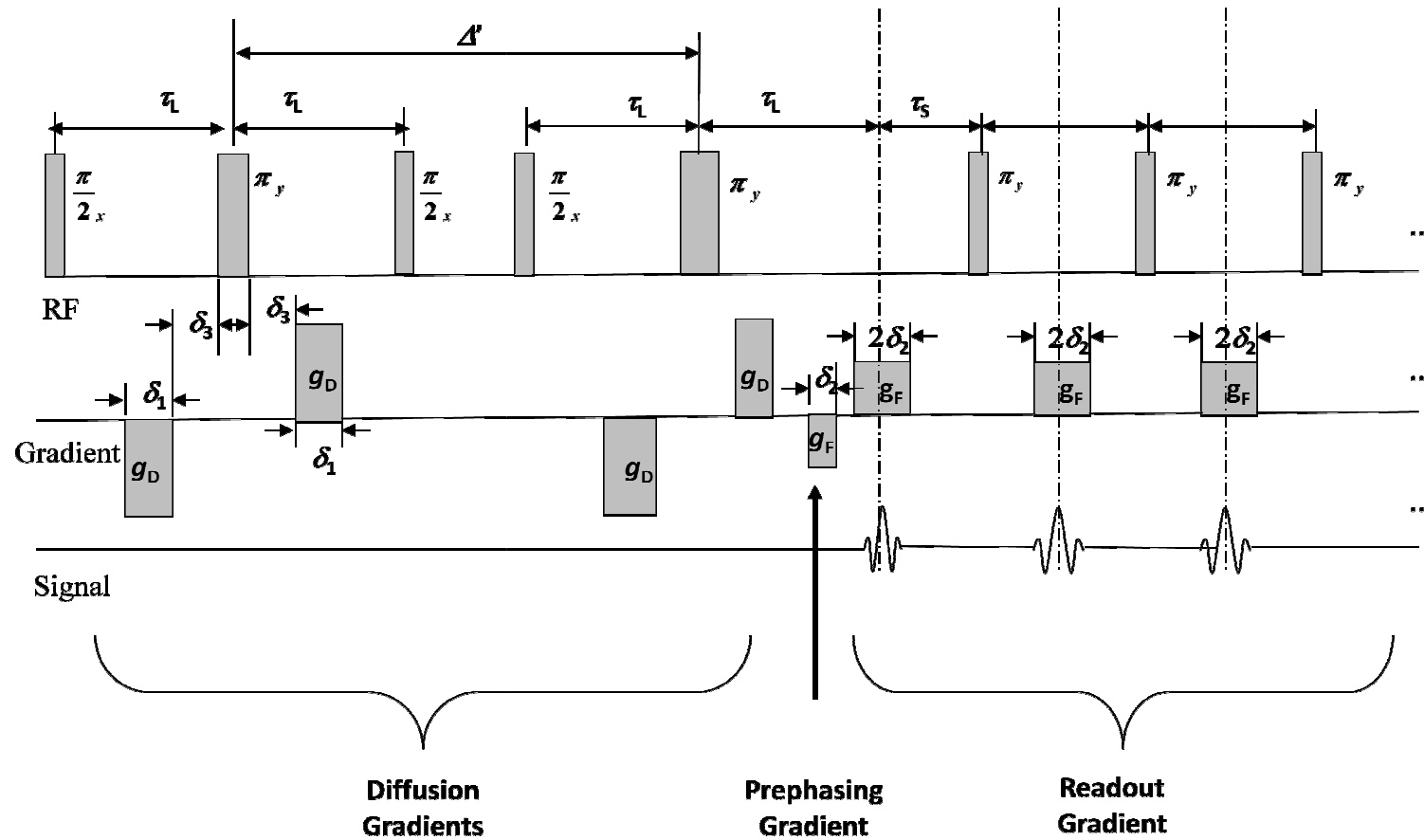


Figure 3.5: Initial design of D - T_2 profiling pulse sequence

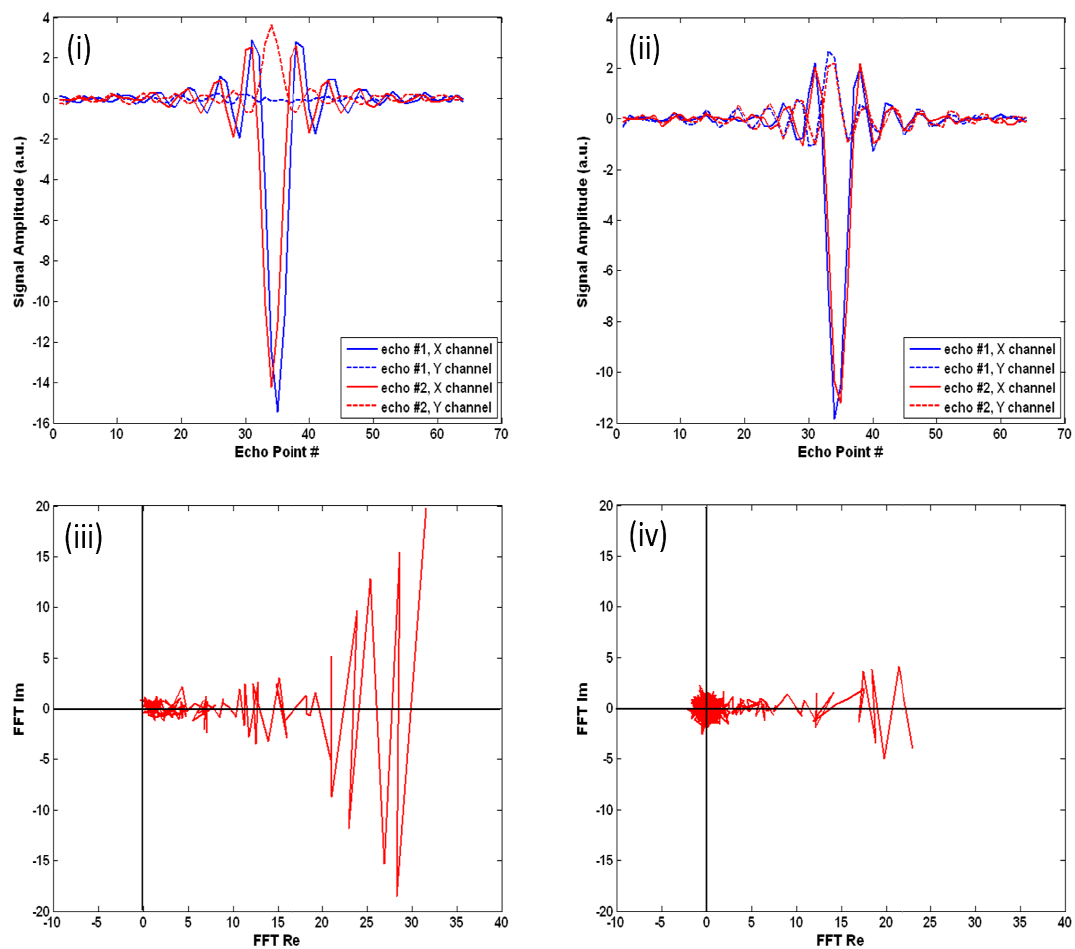


Figure 3.6: Reduction of phase sensitivity. Squalane, $g = 2.5 \text{ G cm}^{-1}$, $d = 6 \text{ msec}$. (i) 1st two echoes before inclusion of $\pi/2$ pulse and, (ii) After. (iii) FFT quadrature data of all echoes at $h = 1.38 \text{ cm}$ echoes before inclusion of $\pi/2$ pulse, and (iv) After.

3.1.3 Magnetization Equation

As discussed in Chapter 2, by implementing the concept of the effective gradient, the attenuation equation for the D - T_2 profiling pulse sequence can be generated. The attenuation equation for the D - T_2 profiling sequence, given by equation (3. 1), shares structural similarity with the diffusion-relaxation attenuation equation for the pulsed field gradient diffusion editing experiment (Hürlimann & Venkataramanan, 2002) (Flaum, Hirasaki, Flaum, & Straley, 2005). The most noticeable difference is the diffusion kernel. In D - T_2 profiling, sensitivity to diffusion stems from two sources: the diffusion gradient pulses as well as the imaging gradient pulses. The portion of the equation related to the diffusion gradient pulses takes the form expected for a bipolar gradient structure (Cotts, Hoch, Sun, & Markert, 1989) and the portion quantifying the effect of the imaging pulses has the same form as the attenuation equation for the RARE pulse sequence.

$$M = \frac{M_0}{2} \exp\left(\frac{-(\Delta' + 2\tau_L)}{T_1}\right) \exp\left(\frac{-2n\tau_S}{T_2}\right) \exp\left(-D\gamma^2 \left[4g_D^2\delta_1^2 \left(\Delta' - \delta_3 - \frac{2\delta_1}{3}\right) + g_f^2\delta_2^2 \left(2(n-1)\tau + \Delta_f - \frac{2(n-1)\delta_2}{3}\right)\right]\right) \quad (3. 1)$$

3.1.4 Data Processing

Data for the D - T_2 experiments is processed in a very similar manner to data generated from a RARE experiment. The main differences are the need to analyze multiple experiments to determine the effect of diffusion and the application of a 2-D inversion. Once the data from the battery of diffusion editing experiments has been readied for inversion, the profile data at a specific height for all of the experiments performed at varying gradient strengths is inverted using a 2-D inversion. The attenuation equation for the D - T_2 profiling experiment, equation (3. 1), can still be broken into two kernels for a 2D inversion (Hürlimann & Venkataramanan, 2002). However, the attenuation due to the imaging pulses is neglected during the inversion since the effect of the imaging pulses is negligible in comparison to the diffusion pulses. For instance, in the measurement of water, the leading term ($4g_d^2 \delta_1^2$) for the weakest gradient in the experiment is roughly 10 times larger than the leading term ($g_f^2 \delta_2^2$) for the imaging pulses.

3.1.5 Phase Cycling

The phase cycling list implemented with the $D-T_2$ profiling experiment was selected in order to help minimize the formation of additional echoes typically accompanying the stimulated echo. The sequence suggested by Fauth et al. (1986) was implemented and repeated in cyclically order pairs (CYCLOPS) (Hoult & Richards, 1975) fashion resulting in a 16 step list. Table 3.1 summarizes the phase cycling list utilized for the $D-T_2$ profiling experiments.

Table 3.1: $D-T_2$ profiling phase cycling list

ϕ_1	ϕ_2	ϕ_3	ϕ_4	ϕ_π	ϕ_{read}
0	0	0	$\pi/2$	$\pi/2$	π
0	0	π	$\pi/2$	$\pi/2$	0
0	π	0	$\pi/2$	$\pi/2$	0
0	π	π	$\pi/2$	$\pi/2$	π
$\pi/2$	$\pi/2$	$\pi/2$	0	0	$3\pi/2$
$\pi/2$	$\pi/2$	$3\pi/2$	0	0	$\pi/2$
$\pi/2$	$3\pi/2$	$\pi/2$	0	0	$\pi/2$
$\pi/2$	$3\pi/2$	$3\pi/2$	0	0	$3\pi/2$
π	0	0	$3\pi/2$	$3\pi/2$	0
π	0	π	$3\pi/2$	$3\pi/2$	π
π	π	0	$3\pi/2$	$3\pi/2$	π
π	π	π	$3\pi/2$	$3\pi/2$	0
$3\pi/2$	$\pi/2$	$\pi/2$	π	π	$\pi/2$
$3\pi/2$	$\pi/2$	$3\pi/2$	π	π	$3\pi/2$
$3\pi/2$	$3\pi/2$	$\pi/2$	π	π	$3\pi/2$
$3\pi/2$	$3\pi/2$	$3\pi/2$	π	π	$\pi/2$

ϕ_1 , ϕ_2 , ϕ_3 , and ϕ_4 represent the phase for the first, second, third, and fourth $\pi/2$ pulses, respectively. ϕ_π represents the phase of all of the π pulses and ϕ_{read} is the phase during acquisition.

3.2 Determination of Porosity and Saturation Profiles

Porosity profiles can be generated in a similar fashion as with RARE results (see Chapter 2). However, when using D - T_2 profiles, an extrapolation of the first few echoes is not performed to calculate M_0 . Instead, the area under the D - T_2 map is taken as a measure of M_0 . Therefore, the porosity profile can be calculated using the following equation.

$$\phi(x) = \frac{\sum_{all D} \sum_{all T_2} f_{core}(D, T_2, x) / \bar{M}_{0brine}}{\pi r^2 L} \quad (3.2)$$

Equation (3. 2) can be implemented on water saturated core samples. However, when a core is saturated with both oil and water, an estimate of porosity can be obtained by relying on the oil's effective Hydrogen Index (HI_{eff}) to calculate the core's pore volume. The Hydrogen Index is a measure of a sample's hydrogen content compared to water at the same temperature and pressure (Coates, Xiao, & Prammer, 1999). When performing a D - T_2 profiling experiment, a large portion of spins can relax due to the long diffusion time resulting in the loss of signal. Therefore, the effective Hydrogen Index is an attempt to compensate for the loss in signal during the diffusion time and is determined by performing independent D - T_2 profiling experiments on water and oil samples while using the same parameters for both measurements. The figure below shows the results for the experiments used to determine the HI_{eff} for Shell Mars Yellow (SMY) crude oil. Once

the effective Hydrogen Index has been determined, an estimate of the porosity profile can be obtained for a partially saturated core sample using equation (3. 3).

$$\phi(x) = \frac{1/\bar{M}_{0brine} \left(\sum_{D>D_{cutoff}} \sum_{all T_2} f_{core}(D, T_2, x) + \sum_{D<D_{cutoff}} \sum_{all T_2} f_{core}(D, T_2, x) / HI_{eff} \right)}{\pi r^2 L} \quad (3. 3)$$

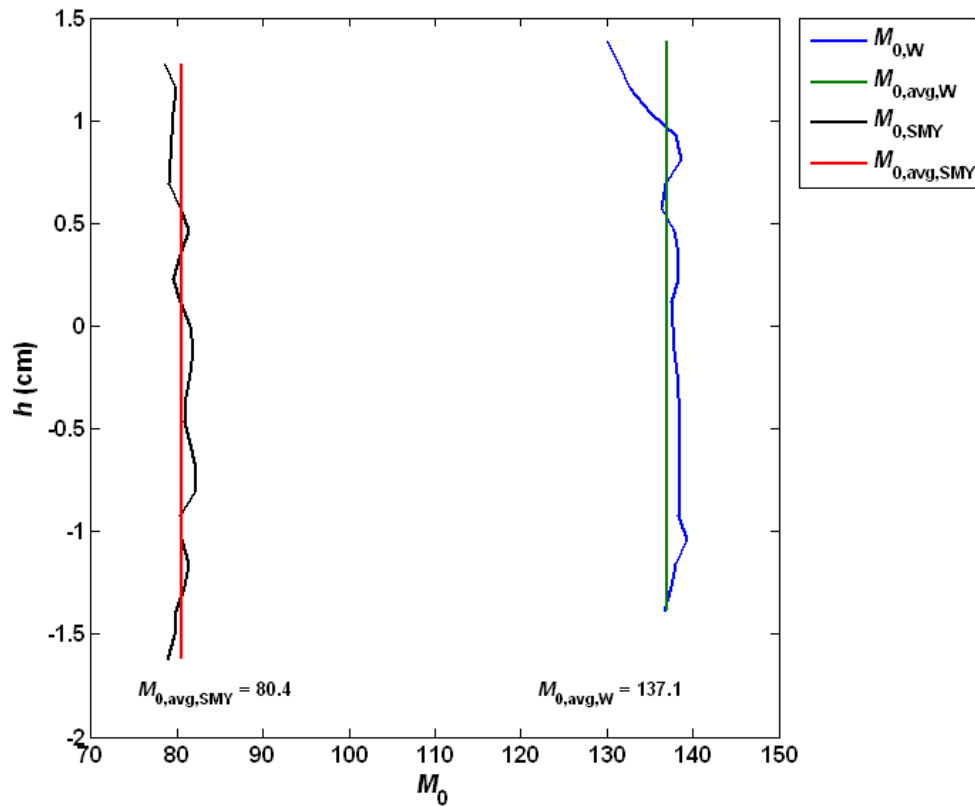


Figure 3.7: Comparison of M_0 for water and SMY crude oil. The effective Hydrogen Index, $HI_{eff,SMY}$, for SMY is 0.58.

Similarly, saturation profiles can be generated once the effective hydrogen index is known. The simplest method in determining saturation is to implement a cutoff based on the self-diffusion coefficients. Data corresponding to smaller diffusion coefficients than the cutoff represent the oil phase while values larger correspond to the aqueous phase. Figure 3.8 illustrates a standard representation of D - T_2 data. In this case, the horizontal, purple dashed line represents the cutoff value for separating the oil signal from the water signal. The saturation profile can be calculated using equation (3.4). An alternate approach which lacks the need for arbitrarily selecting a cutoff to determine saturation is presented in a later section.

$$S_o(x) = \frac{\sum_{D < D_{cutoff}} \sum_{all T_2} f_{core}(D, T_2, x) / HI_{eff}}{\left(\sum_{D > D_{cutoff}} \sum_{all T_2} f_{core}(D, T_2, x) + \sum_{D < D_{cutoff}} \sum_{all T_2} f_{core}(D, T_2, x) / HI_{eff} \right)} \quad (3.4)$$

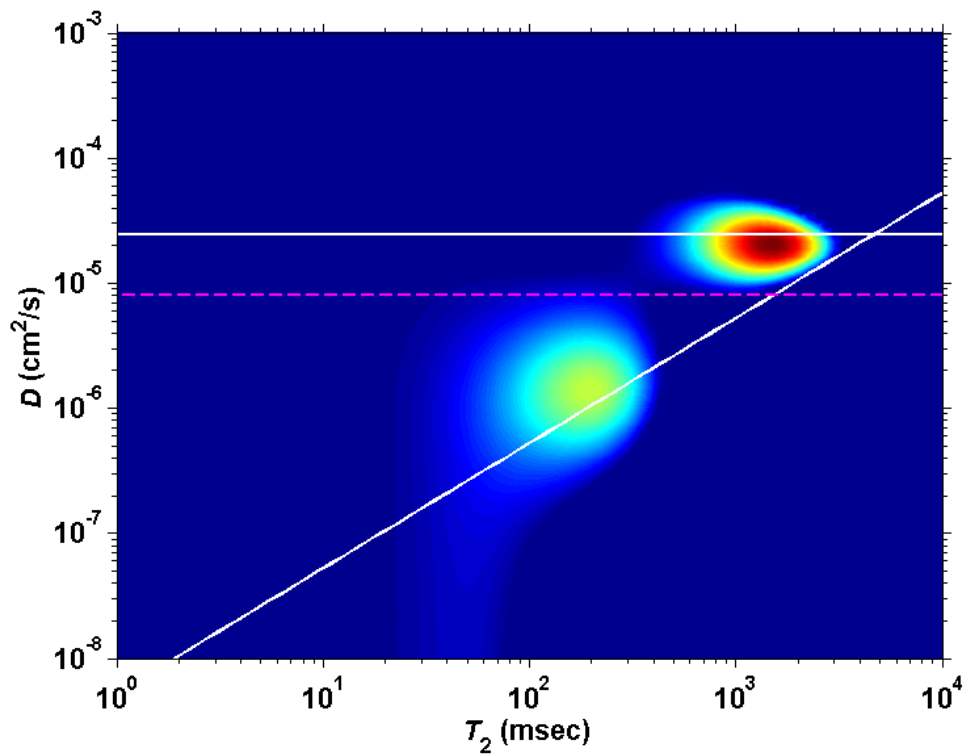


Figure 3.8: D - T_2 profiling map of water and SMY in a sandpack after 0.3 PV waterflood at $h = 12.8$ cm. The diffusion coefficient for water and the D - T_2 correlation for dead crude oils correspond to the horizontal and sloped solid white lines. The dashed purple line indicates the cutoff value used in calculating saturation.

3.3 Parameter Selection

Selecting appropriate parameters is vital in producing quality NMR data. For D- T_2 profiling, parameter selection can be divided into two categories: selection of diffusion parameters and imaging parameters. Diffusion and imaging parameters can be selected independently since the attenuation due to the imaging pulses should be minimal in comparison to the diffusion gradients (Neeman, Freyer, & Sillerud, 1990). Flaum (2007) presents a methodology in selecting appropriate parameters (Δ , d , g) for a diffusion measurement. Also, imaging parameters can be selected as previously discussed for the RARE pulse sequence (see Chapter 2).

The parameters presented in Table 3.2 and Table 3.3 were selected to measure a sandpack saturated with water and Shell Mars Yellow (SMY crude oil). Note that the imaging parameters were selected so that aliasing would not occur. Since the sandpack is 1 foot in length, a large portion of the sample resides outside of the probe's sweet spot for any given measurement. Therefore, the length of the probe's detection range was used as a proxy for the sample height in calculating the imaging parameters. For each image, only data corresponding to positions within the sweet spot was processed. Then, the sandpack is moved so that another portion of the sample resides within the sweet spot. A composite image can then be constructed by stacking the results from each measurement.

Table 3.2: Diffusion parameters selected for the measurement of a water and SMY saturated sandpack

Diffusion Parameters	
Δ'	40 msec
δ_1	5.1 msec
δ_3	1 msec
g_D	0.8 to 45 G cm ⁻¹
τ_{long}	15.1 msec

Table 3.3: Imaging parameters selected for the measurement of a water and SMY saturated sandpack

Imaging Parameters	
τ_{short}	3 msec
g_F	0.8 G cm ⁻¹
δ_2	1.3 msec
SI	128
DW	0.016 msec

In addition to the parameters summarized in Table 3.2 and Table 3.2, careful selection of the number of gradient pre-pulses and the spacing between RF and gradient pulses is vital to removing artifacts from the generated profiles. Careful selection of these parameters improves the quality of the profiles. Furthermore, refinement of the gradient list is necessary in order to reduce the experimental duration so that the experiments can be completed in a reasonable time frame. These topics are covered in the following sections.

3.3.1 Diffusion Editing Parameters

The goal behind selecting diffusion editing parameters is to allow for the collection of as much T_2 information as possible while also being able to fully attenuate the sample for a diffusion measurement. Selection of the diffusion time (Δ) was based on the rule of thumb that $\Delta/T_2 \approx 0.5$ (Flaum, 2004). Smaller Δ 's yield sharper results when all other parameters remained the same. As Δ is increased, more T_2 relaxation occurs during the diffusion time causing fast relaxing peaks to become less distinct and more spread out. However, large gradients are needed to attenuate the SMY signal. So the selection of $\Delta/T_2 \approx 0.5$ will result in some T_2 attenuation of the oil, but will allow for the appropriate time intervals needed for the placement of the gradients pulses. The characteristic T_2 was taken to be the log mean relaxation time for the SMY crude oil (83 msec). Therefore, Δ was set to 40 msec. Next, δ_1 was chosen such that the SMY would be attenuated to a ratio of 0.01 when using nearly the full range of the gradient amplifier. The maximum gradient strength selected was set to 45 G cm^{-1} in order to avoid any possible pulse irregularities when using the very upper limits of the gradient amplifier's range.

Initial experiments were performed with a set of 25 logarithmically spaced gradient strengths (Flaum, 2007). The first point was selected by determining the necessary gradient strength needed to attenuate water to an attenuation ratio of 0.99. The last point was set to 45 G cm^{-1} , the maximum desired gradient strength. The length of the list allowed for both the water and oil phases to be clearly resolved, but required an experimental duration close to 36 hours for the measurement of a 4 cm section. This

translates to an experimental duration of roughly 15 days in order to complete the measurement of a 1 foot long sandpack. Thus, a set of 25 points make this experiment impractical due to the duration of the experiment.

In order to reduce the time needed to complete the measurement, the use of shorter gradient lists has been examined. It is desired to use as short of a set of gradient strengths as possible to resolve saturation profiles. The result from this initial set of gradient strengths will be used as a basis for future comparison with shorter lists. Points were systematically removed from the initial list prior to inversion of the experimental data so the effect of using different sets of gradients can be mimicked without need of repeating the measurement. First, data was inverted using full set of 25 gradient strengths. Log mean values of T_2 and D were determined from the $D-T_2$ maps for both phases, and these values were used in a simple simulation describing the expected behavior during the experiment using the attenuation equation (equation (3. 1)). Two things become immediately obvious: two diffusion regimes exist (one for water and one for oil), and the log spacing of the gradient strengths concentrates the majority of the data in the water sensitive region. Points were initially dropped from 25 to 12. This was done by trying to keep the points roughly evenly spaced with respect to the log of the attenuation ratio over the two diffusion attenuation regimes. For example, Figure 3.9 shows the expected attenuation ratios for both of the oil and water phases and the 12 gradient strengths selected to measure each regime. The first six points were selected specifically to be sensitive to water, while the last six were selected to be sensitive to the oil phase. After determining the saturation profiles when using 12 gradients strengths, the procedure was repeated, and the number of points varied from 12 to 6 gradient values.

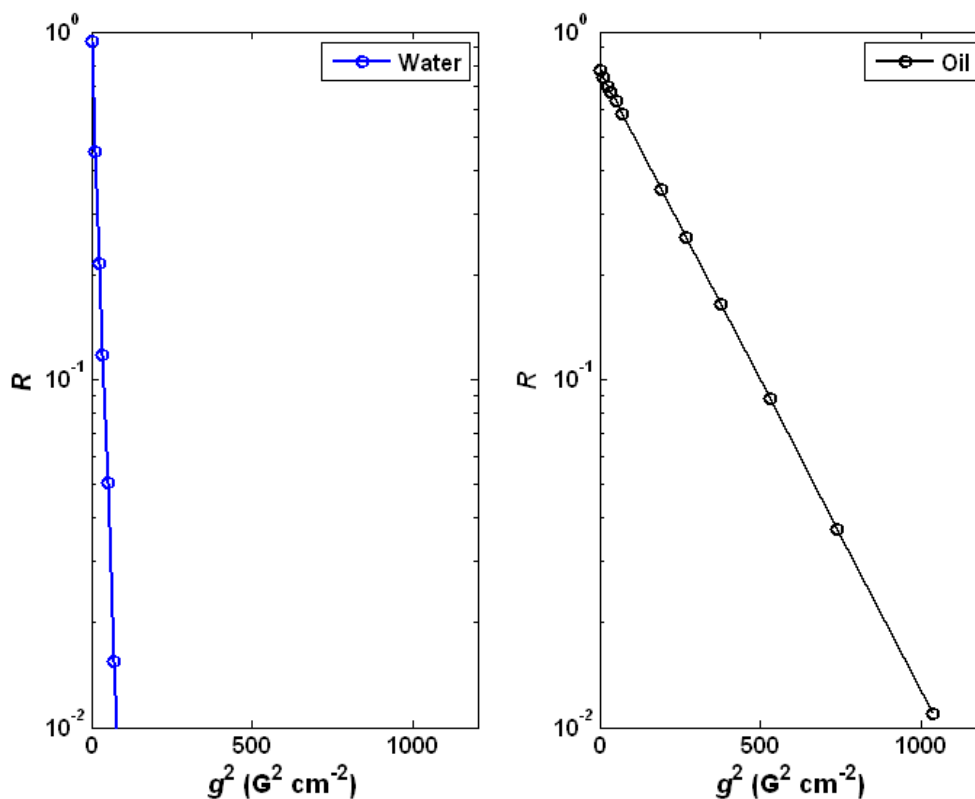


Figure 3.9: Expected attenuation ratio for water (left pane) and oil (right pane) using a 12 point gradient list.

Figure 3.10 shows the saturation profiles when the number of gradients used during the inversion is varied and spaced evenly with respect to g^2 . For this experiment, a collection of vials were filled to different heights of water and oil so that step changes in the saturation profile would be evident. As the number of gradient values used during the inversion is reduced, the resulting saturation profile becomes noisier and underestimates the actual saturation. However, the use of 10 to 12 gradient strengths yields a saturation profile that is in good agreement with the full set of data (25 points).

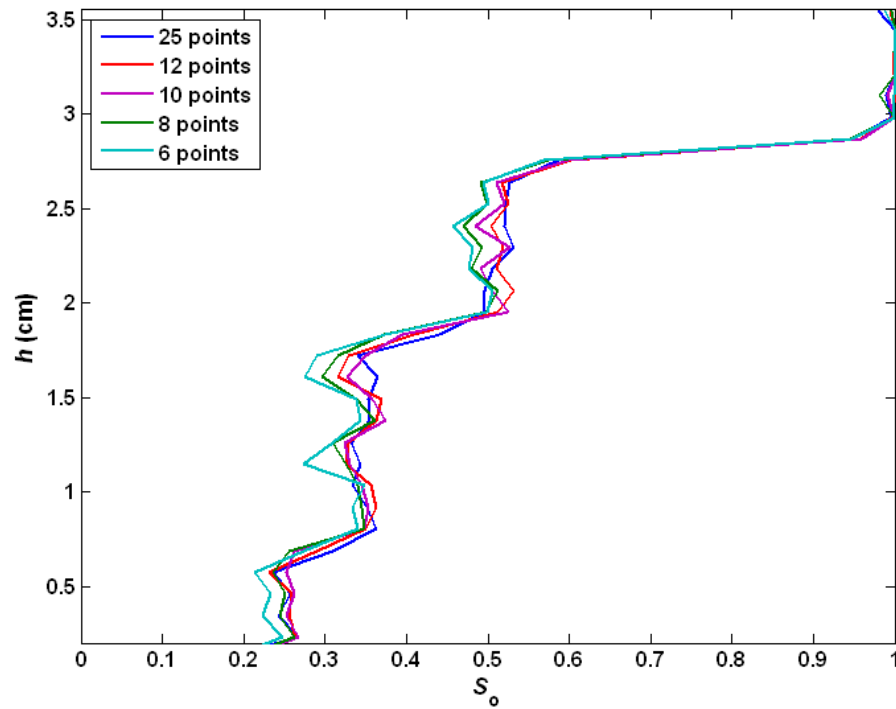


Figure 3.10: Saturation Profiles for a collection of vials with varying heights of oil and water when the number of gradients used during inversion is reduced and spaced evenly with respect to g^2 . $S_o = 1.0, 0.5, 0.33,$ and 0.25 from top to bottom.

In addition to an even space with respect to g^2 , a geometric space of the gradient points was also examined. The same procedure was followed as noted above. The attenuation range was divided into two regions and the first and last gradient strength was identified for each section. Then points were selected from the original set of 25 to generate set of gradients strengths with geometric spacing. The results are presented in Figure 3.11.

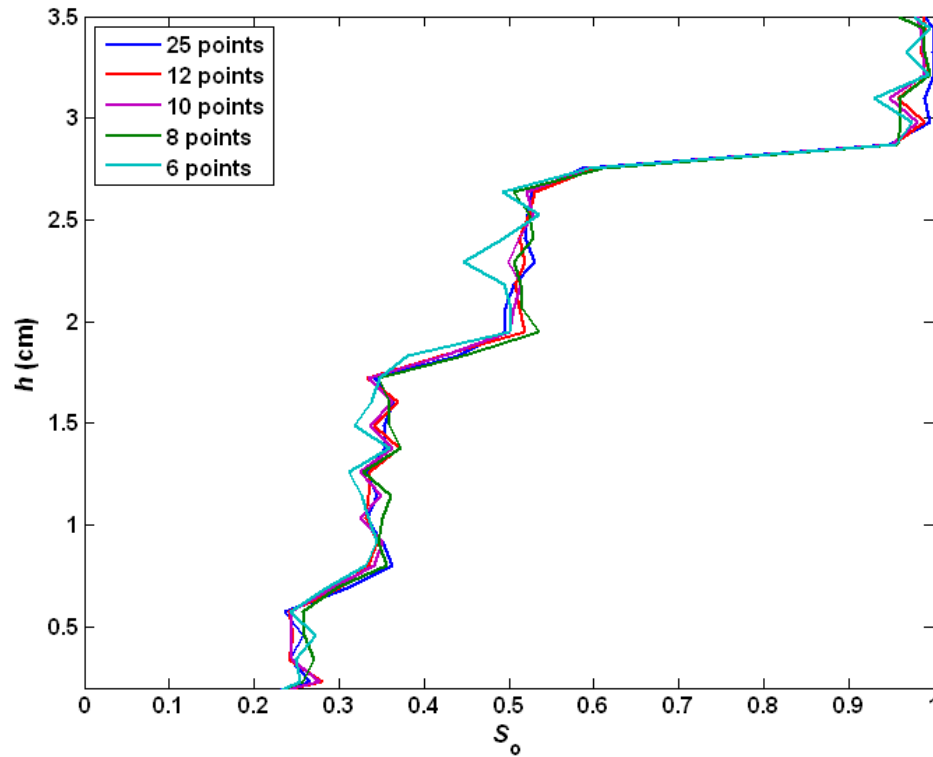


Figure 3.11: Saturation Profiles for a collection of vials with varying heights of oil and water when the number of gradients used during inversion is reduced and spaced geometrically. $S_o = 1.0, 0.5, 0.33,$ and 0.25 from top to bottom.

From the results presented in Figure 3.10 and Figure 3.11, both approaches to reducing the number of needed gradient strengths for verification of saturation show that a set of 25 gradient values is not necessary. Using either even spacing with respect to g^2 or geometric spacing, the length of this list can be greatly reduced. Since both spacing strategies are effective, the large reduction in the number of data points is most likely a result of splitting the gradient list into two with one part sensitive to water and the other oil. A suitable saturation profile is achieved using a 10 to 12 point list with even g^2 spacing or an 8 point list using geometric spacing. Therefore, it appears that geometric spacing allows for a smaller list. This may be a result of the first few points being spaced

closer together when the signal to noise ratio is higher. However, the geometric spacing yields poor results when measuring high oil saturation and should be avoided when measuring cores with high oil saturation such as samples at irreducible water saturation.

From these results, a procedure can be developed that will enable the selection of a set gradients suitable for the determination of a saturation profile. First, the gradient list can be divided into two sets. The first set allows the measurement to be sensitive to water and the second to oil. For the water sensitive gradient strengths, the first and last points are selected so that the entire attenuation range of the water can be measured. Data points are then spaced geometrically over this range. While these gradient pulses are primarily chosen to help identify the water phase, they will also cause the oil signal to attenuate. In order to measure the oil phase, the second half of the gradient list should span the region starting with the last gradient value in the water sensitive set and end with a gradient value that will attenuate the remain signal to noise. Once again, the gradient values should be spaced geometrically. However, the use of geometric spacing should be used cautiously when analyzing samples with oil saturation expected to be near unity since the results presented in Figure 3.11 show a deviation from the expected oil saturation in the region where $S_o = 1$.

3.3.2 Gradient Pre-Pulses

Gradient pre-pulses add additional stability to the gradient waveform by balancing the effect of eddy currents on the system's magnetization throughout the duration of the pulse sequence (Gounarides, Chen, & Shapiro, 1999). While the bipolar diffusion gradients are supposed to help balance the effect of the eddy currents generated by strong pulses, analysis of the echo and subsequent 1-D profile generated during a D - T_2 profiling experiment at a high gradient strength indicate that gradient instability may still exist.

Improper selection of the number of gradient pre-pulses can generate artifacts in the resulting D - T_2 profiles. For instance Figure 3.12 displays the result of a D - T_2 profiling experiment performed on a sandpack at residual water conditions without the application of gradient pre-pulses. In Figure 3.12 (right pane), the intensity of the projected self-diffusion data forms a valley in each region of interest. However, this valley does not show up in the porosity and saturation profiles (Figure 3.13) calculated from the D - T_2 profile. Examination of the echo data for the experiment shows that at low g values an echo with a single peak forms (Figure 3.14) while the use of high g values results in echoes with two distinct peaks (Figure 3.15). This is indicative of a sequence in which the gradients prior to refocusing are not properly balanced by the gradients after refocusing. In other words, the magnitude and duration of the first set of bipolar pulses is not equivalent to the second set even though their parameters are identical.

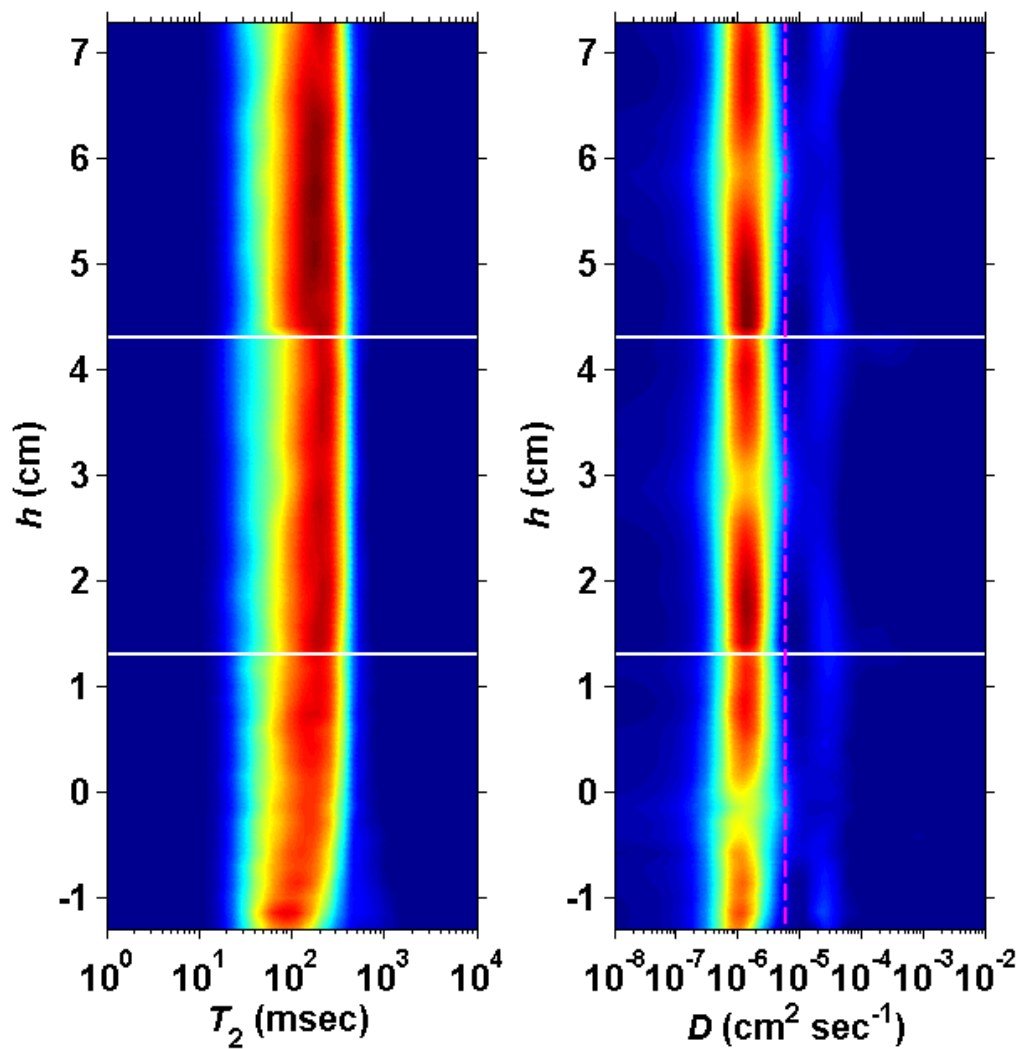


Figure 3.12: T_2 and D projections of D - T_2 profile maps for a sandpack after oilflood. Horizontal white lines indicate individual measurement regions

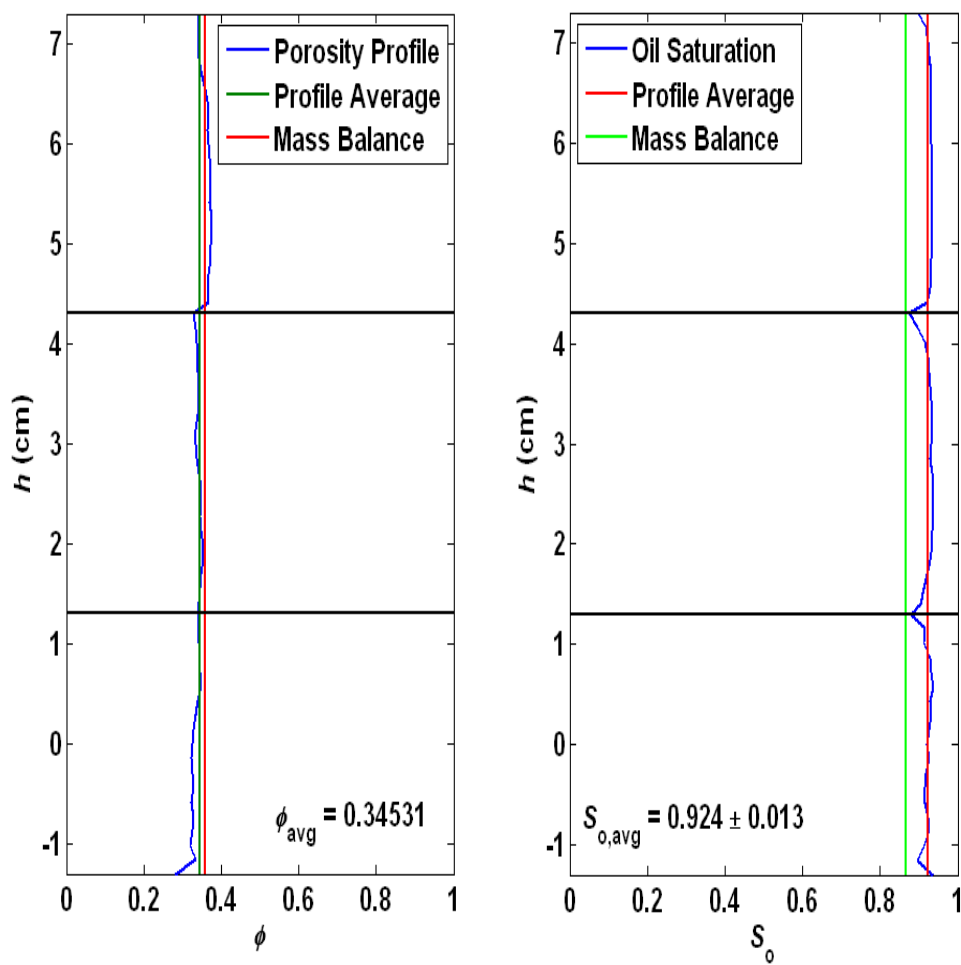


Figure 3.13: Porosity (left) and oil saturation (right) profiles generated from D - T_2 profiling measurements. Horizontal black lines indicate individual measurement regions.

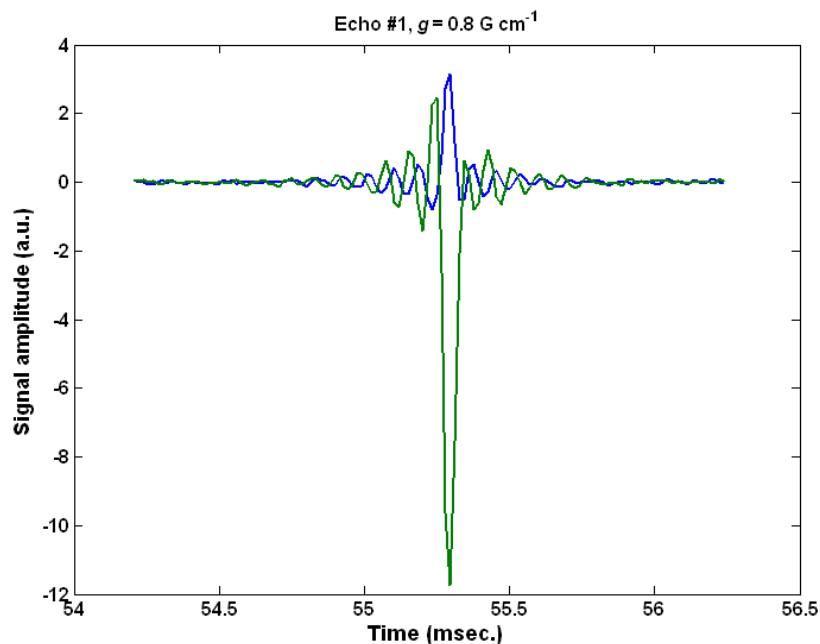


Figure 3.14: First echo collected with D - T_2 profiling pulse sequence using a weak gradient ($g = 0.8 \text{ G cm}^{-1}$)

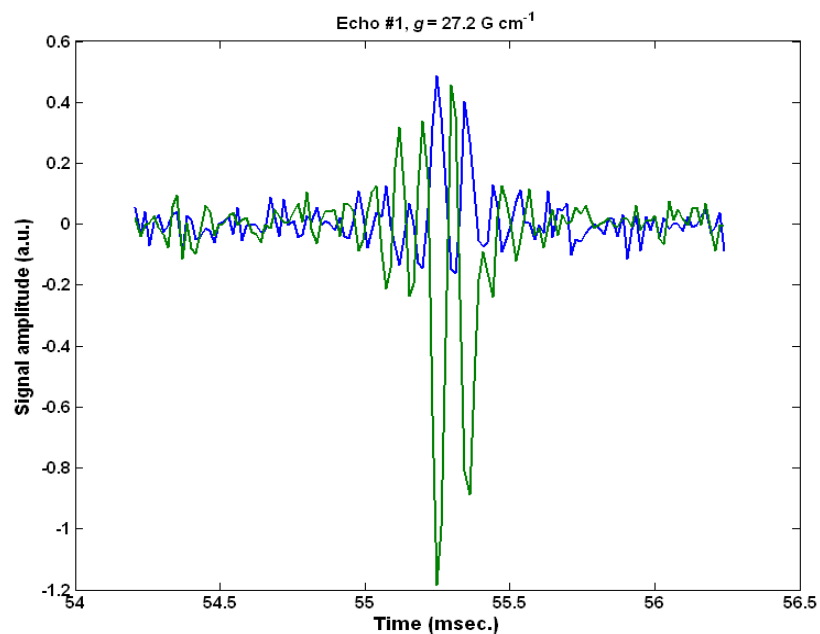


Figure 3.15: First echo collected with D - T_2 profiling pulse sequence using a strong gradient ($g = 27.2 \text{ G cm}^{-1}$). Note the presence of two peaks as compared to the single peak in Figure 3.14.

A battery of measurements was performed in order to select an appropriate number of pre-pulses. Parameters were set to those listed in Table 3.2 and Table 3.3, but the number of pre-pulses was varied between 0 to 9. Each pre-pulse consists of a bipolar pair separated by $2\delta_3$ while each pair is separated by Δ' . Figure 3.16 shows the results of several D - T_2 experiments performed with different number of pre-pulses. Each subplot depicts the profile of the first echo collected at various gradient strengths: 19.4, 27.2, 32.2, 38.0, and 45.0 G cm⁻¹. When too few gradient pre-pulses are used, the profiles generated from the first echo using the largest 4 gradient strengths demonstrate large variations and often times overlap with one another. This phenomena is noted when either 0, 1 or 3 pre-pulses are implemented (Figure 3.16, subplots (i), (ii) and (iii)). As the number of pre-pulses was increased, the profiles start to flatten out and separate because the gradient pre-pulses prevent an echo from forming two distinct peaks (Figure 3.17). However, the profile corresponding to the experiment performed at the largest diffusion gradient strength never changes its appearance in any appreciable manner which may be due to low signal to noise ratio for the measurement. Furthermore, little difference is noted between the results when using 5, 7 or 9 pre-pulses (Figure 3.16, subplots (iv), (v) and (vi)). Therefore, the range between 5 and 9 pre-pulses yields a suitable value for the number of needed gradient pre-pulses. Figure 3.18 shows the results of D - T_2 experiment performed on the same sandpack depicted in Figure 3.12, but with the application of 9 gradient pre-pulses to the upper segments of the sample and no pre-pulses in the lower part. From these results, it is clear that the application of gradient pre-pulses eliminates the valley noted in the intensity of the diffusion data (Figure 3.12).

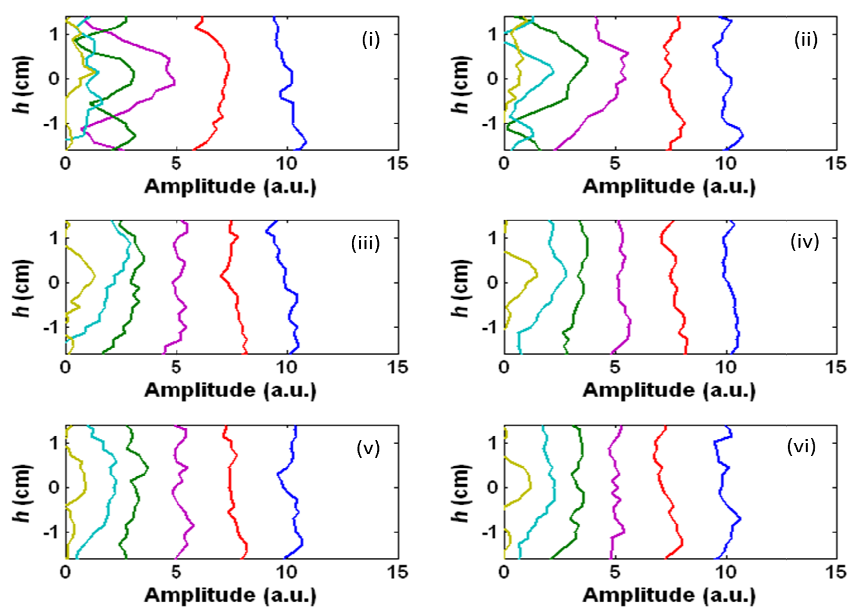


Figure 3.16: Results from D - T_2 profiling experiments performed using (i) 0, (ii) 1, (iii) 3, (iv) 5, (v) 7, and (vi) 9 gradient pre-pulses. The colored lines represent the first echo collected at $g = 19.4, 27.2, 32.2, 38.0,$ and 45.0 G cm^{-1} (from left to right).

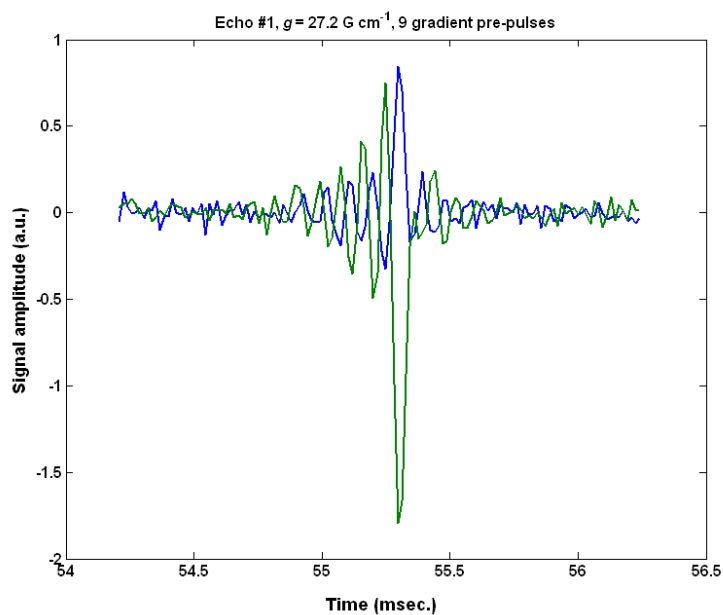


Figure 3.17: First echo collected with D - T_2 profiling pulse sequence using a strong gradient ($g = 27.2 \text{ G cm}^{-1}$) and 9 gradient prepulses. Note the absence of two peaks as compared Figure 3.15

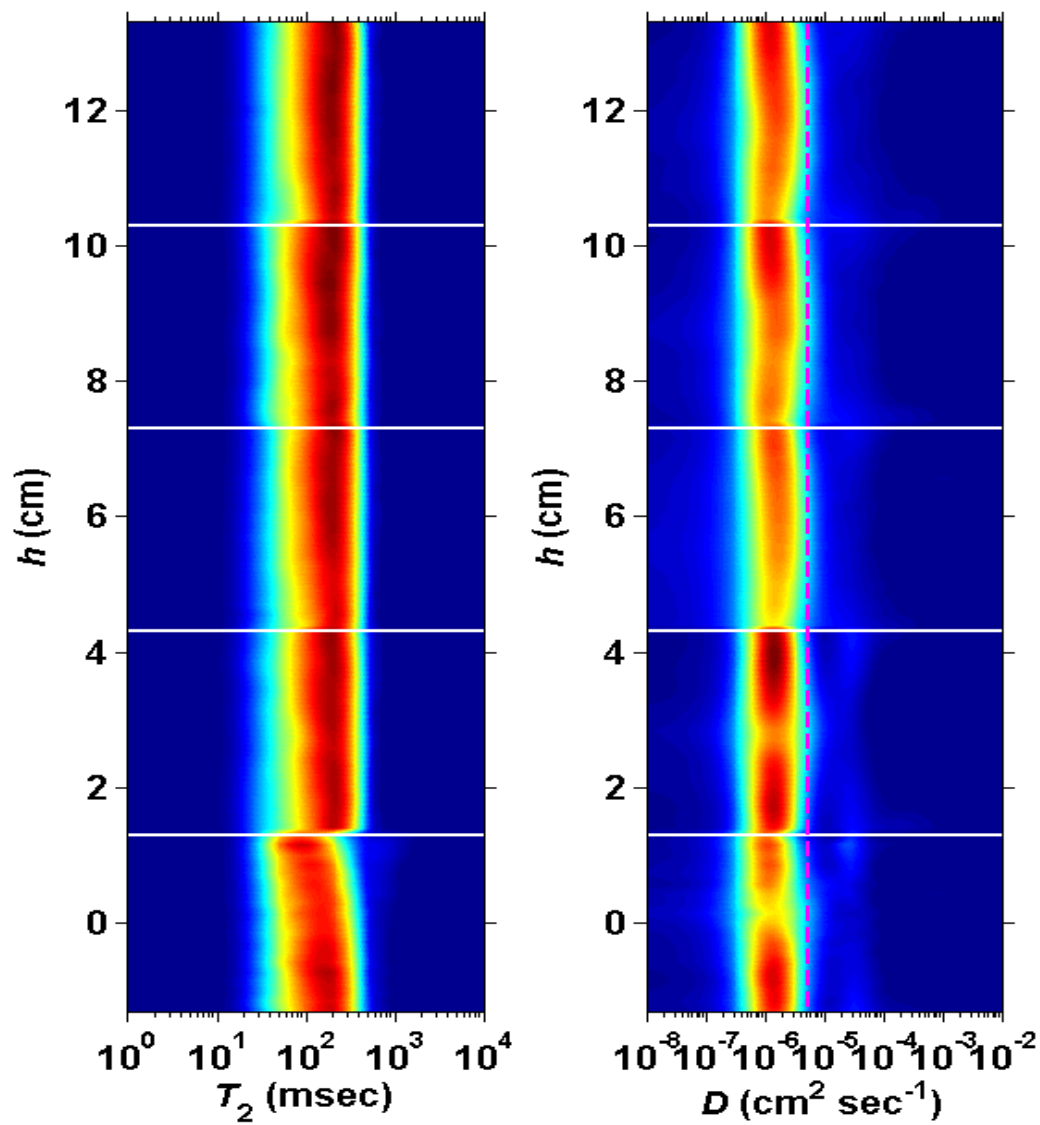


Figure 3.18: T_2 and D projections of D - T_2 profile maps for a sandpack after oilflood. The pulse sequence utilized 9 pre-pulses for the measurement of the top 3 sections and 0 prepulses for the bottom 2 sections. Horizontal white lines indicate individual measurement regions

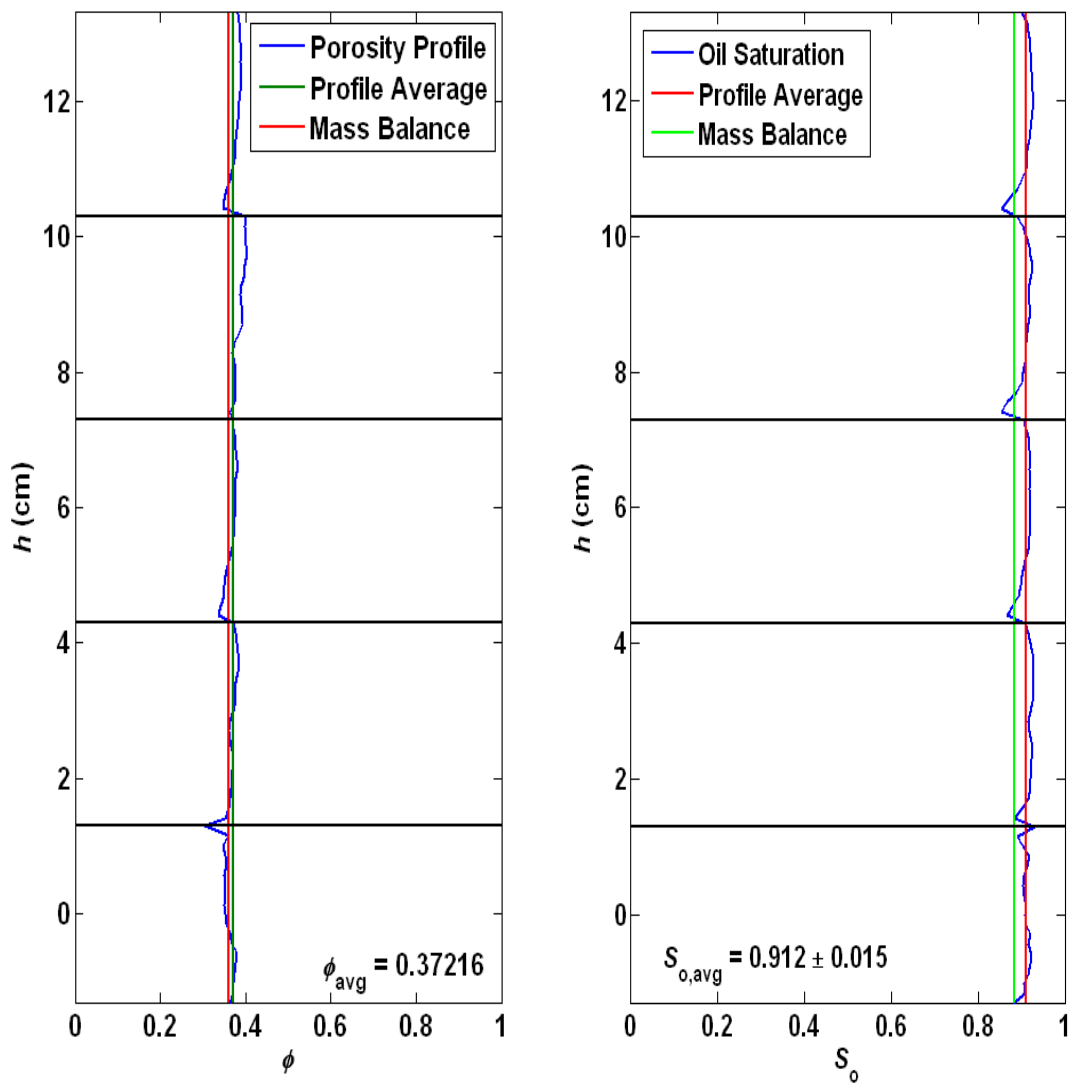


Figure 3.19: Porosity (left) and oil saturation (right) profiles generated from $D-T_2$ profiling measurements. The pulse sequence utilized 9 pre-pulses for the measurement of the top 3 sections and 0 prepulses for the bottom 2 sections. Horizontal black lines indicate individual measurement regions.

3.3.3 Spacing between RF and Gradient Pulses

Narrow spacing between RF and gradient pulses can greatly impact the tipping ability of the RF pulse. Gradient pulses require time for the magnetic field to stabilize when the gradient is turned on or off. If the spacing between RF and gradient pulses is less than the gradient fall time, then the two will overlap causing degradation of the NMR signal. When a RF pulse is applied while there is a gradient in the magnetic field, the RF pulse becomes slice selective causing certain locations within the sample to not be completely refocused.

While the application of gradient prepulses helped to remove the valley present in the measured D - T_2 profiles, a consistent dip near the bottom edge of the measurement region is still present (Figure 3.18, right pane). This dip is also noted in the oil saturation profile near the bottom of each measurement region (Figure 3.19, right pane). This feature appears to be included in all of the measurement sections and therefore, the cause is most likely a hardware phenomena rather than a true representation of the sandpack. Since this behavior appears to occur at the same height within the sample, the cause most likely stems from the application of the gradients since the gradient introduces sensitivity to position. The prepulses help stabilize the pulse, but a long tail to the pulse can still effect the system by interfering with the RF pulses.

In order to select an appropriate spacing between the gradient and RF pulses, a simple pulse sequence is used. In this sequence, a gradient pulse is applied and then after some duration (δ_3) an FID experiment is performed (Figure 3.20). As δ_3 is increased, the FID decay becomes slower indicating a smaller influence of the gradient pulse on the RF

pulse (Figure 3.21). When δ_3 approaches 10 to 15 msec, only a small deviation in FID decay is noted indicating that this time delay (δ_3) is needed between RF and gradient pulses in order to avoid any interaction between the two. However, if δ_3 is set to 10 or 15 msec for the D - T_2 profiling experiment (Figure 3.1), a large portion of the oil signal will be lost due to relaxation of the oil phase before the collection of the first echo. Therefore, a smaller value of δ_3 must be selected, and a trade-off between signal quality and T_2 information exists. In order to avoid losing a majority of the crude oil components to T_2 relaxation during the diffusion sensitive portion of the sequence, it is desired to collect the first echo before $t = T_{2,\log\text{mean}}$ of the crude oil. Subsequently, δ_3 in the D - T_2 profiling sequence must be less than 6 msec ($\Delta = 40$ msec, $\delta_1 = 5.1$ msec) and was therefore set to 5 msec. Figure 3.22 shows two 1-D profiles acquired over the same portion of the sandpack using the pulse sequence in Figure 3.1. The same diffusion gradient pulses were applied, but one used a value of δ_3 equaled to 1.0 msec and the other 5.0 msec. The experiment performed with $\delta_3 = 1.0$ msec shows a rounding at the bottom of the sample similar to the response observed in the saturation profile (Figure 3.19, right pane). When δ_3 is increased to 5.0 msec, no rounding is observed and the profile appears to be fairly uniform across the sample. Figure 3.23 and Figure 3.24 display the results acquired from a sandpack at irreducible water conditions with a gradient-RF spacing of 5.0 msec. While $\delta_3 = 5.0$ msec is much less than the needed 10 to 15 msec spacing indicated in Figure 3.21, the symptomatic rounding of the profiles noted in Figure 3.18 and Figure 3.19 was alleviated.

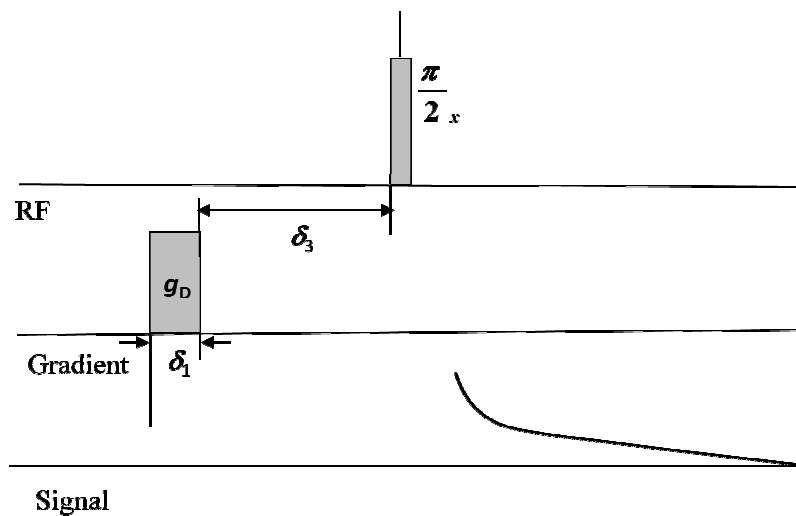


Figure 3.20: Pulse sequence used to examine the effect of RF-gradiated pulse

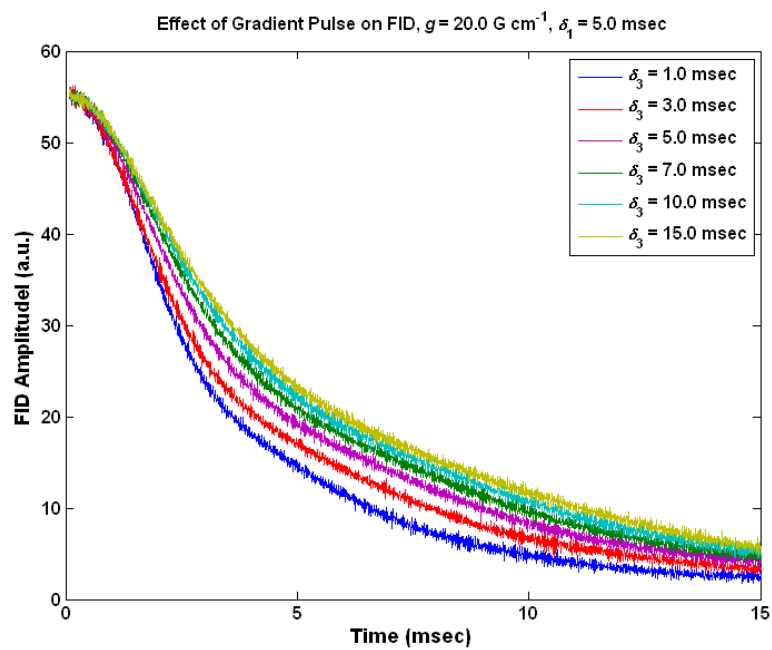


Figure 3.21: Effect of δ_3 on the FID signal using the pulse sequence depicted in Figure 3.20

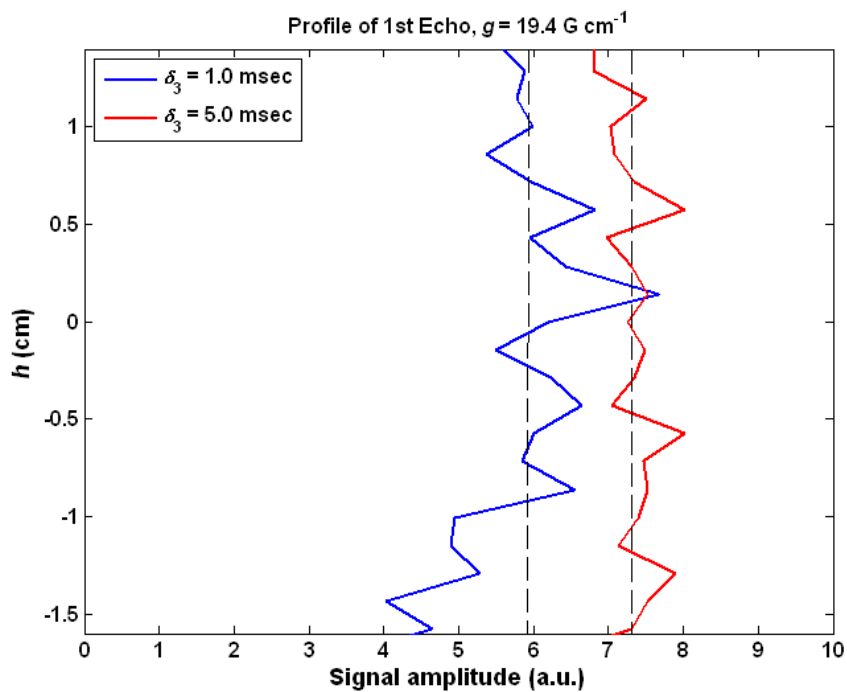


Figure 3.22: Profiles of first echo collected from D - T_2 profiling pulse sequence. Experiment with $\delta_3 = 1.0 \text{ msec}$ exhibits a smaller amplitude and noticeable rounding near the bottom of the measurement range in comparison to the experiment performed with $\delta_3 = 5.0 \text{ msec}$.

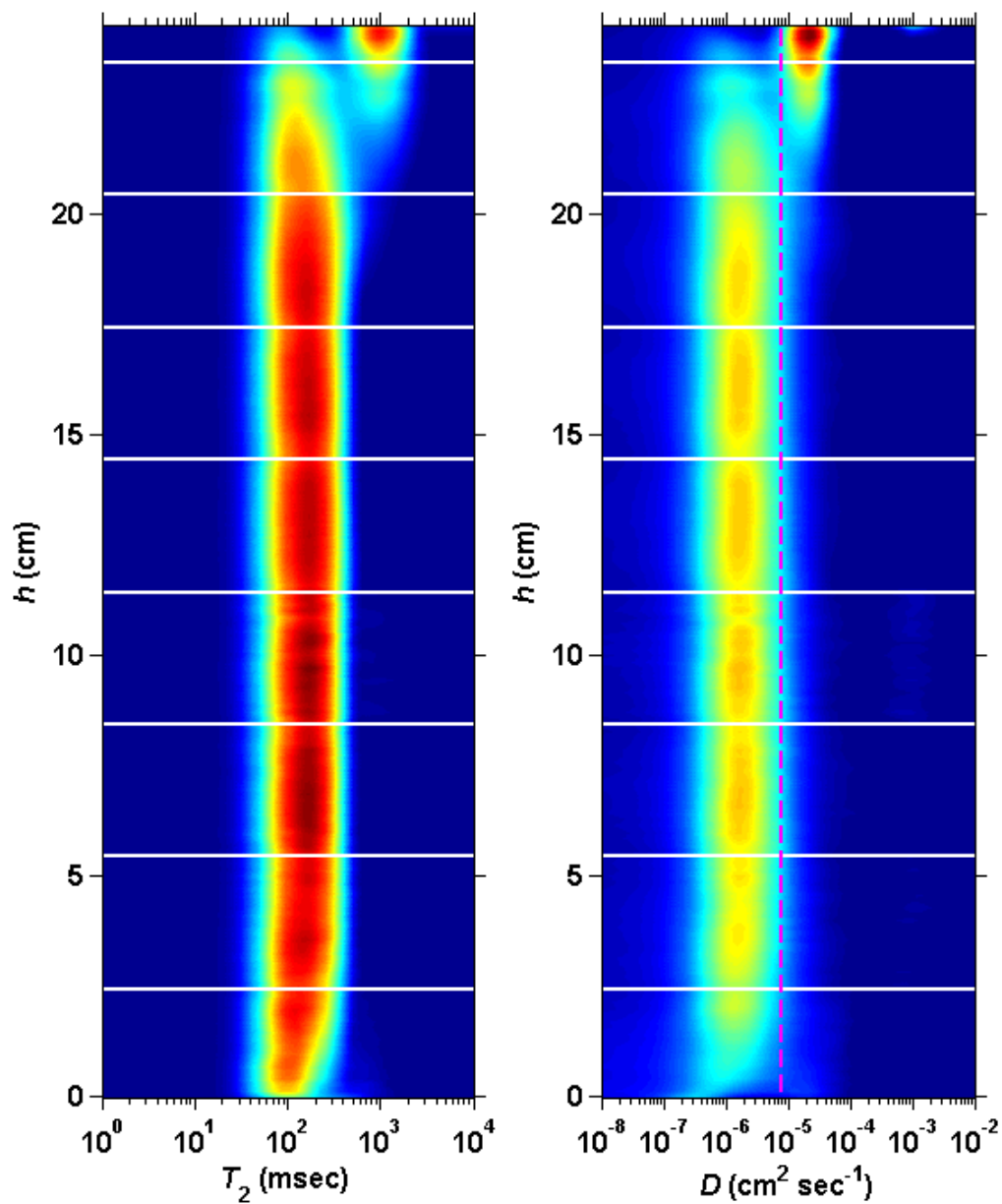


Figure 3.23: T_2 and D projections of D - T_2 profile maps for a sandpack after oilflood. Oilflood was performed at a rate of 5 ft day^{-1} . Horizontal white lines indicate individual measurement regions

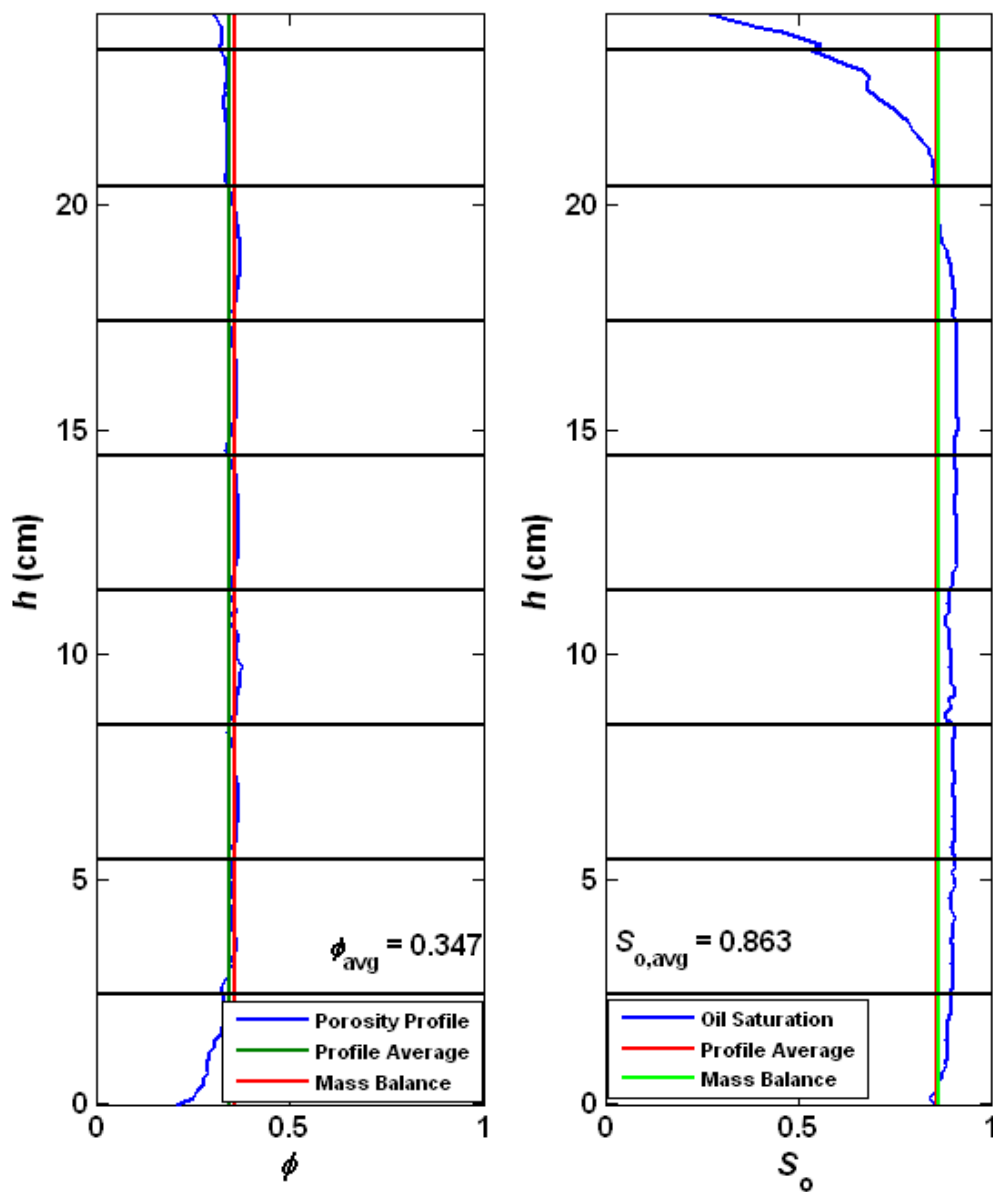


Figure 3.24: Porosity (left) and oil saturation (right) profiles generated from $D-T_2$ profiling measurements. Oilflood was performed at a rate of 5 ft day^{-1} . Horizontal black lines indicate individual measurement regions.

3.4 SandPack Experiments

A glass column of 4.4 cm I.D. and 30.5 cm length was packed with U.S. Silica 20/40 sand. Next, CO₂ was introduced into the system to remove any air. Then, approximately 4.5 pore volumes of water were used to flush the sandpack. The pore volume, porosity, and permeability were determined to be 160 mL, 0.36, and 80.3 Darcy, respectively. NMR profiling experiments were performed after each stage of the flooding process. All D - T_2 profiling experiments were performed with the parameters listed in Table 3.2 and Table 3.3 except d_3 was set to 5.0 msec and 9 gradient pre-pulses were included prior to excitation.

After the initial waterflood, Shell Mars Yellow ((SMY) crude oil was introduced into the column. The oilflood was performed at a rate of 5 ft day⁻¹, and a total of 4 PV of oil was injected. The resulting average oil saturation was calculated to be 0.867 by mass balance and 0.863 by NMR. Examination of the saturation profile after the oilflood allowed for the identification of an end effect at the outflow end of the sandpack (Figure 3.23 and Figure 3.24). The capillary end-effect is a result of the continuity of capillary pressure across the face of the core (Bear, 1972). When the water saturation near the outflow end of the sandpack is low, this can result in a large gradient in capillary pressure in this region of the sandpack. Water will be retained within the porous medium until the pressure gradient in the oil phase exceeds the capillary pressure gradient. The capillary end effect number, $N_{C,end}$, can be used to determine under which conditions an capillary end effect may be present. When $N_{C,end} < 0.10$, viscous effects dominate minimizing the capillary end effect (Mohanty & Miller, 1991). At a velocity of 5 ft day⁻¹, the value of

$N_{C,end}$ was equaled to 0.81. Subsequently, an end effect was noticed in the measured saturation profile. However, when the flow rate was increased to a superficial velocity of 40 ft day⁻¹, the pressure drop in the oils phase is increased, and the value of $N_{C,end}$ was reduced to 0.10 resulting in minimization of the end effect as demonstrated in Figure 3.25 and Figure 3.26.

$$N_{c,end} = \frac{\sigma\sqrt{k\phi}}{\mu\nu L} \quad (3.5)$$

Upon completion of the oilflood, a waterflood was performed at a rate of 1 ft day⁻¹. The waterflood was performed in two steps; each step consisting of an injection of 0.3 PV of water. After each step, saturation profile was measured. The water injections were performed 7 weeks apart. The D and T_2 projections taken after the first and second injection are represented in Figure 3.27 and Figure 3.29, respectively. The gravity number, N_G , and mobility ratio were determined to be 0.94 and 1.21, respectively. The saturation and porosity profiles are also presented in Figure 3.28 and Figure 3.30. The NMR profiling experiments yielded average oil saturations of 0.62 and 0.35 after 0.3 and 0.6 PV waterflood, respectively which is in good agreement with saturations obtained via mass balance ($S_o = 0.63$ and 0.36 after 0.3 and 0.6 PV waterflood, respectively). In Figure 3.31, the resulting saturation profiles have been combined into a single plot. Near the inlet, the saturation profiles for the 0.3 and 0.6 PV water floods do not overlap. When a wetting fluid is displacing a non-wetting fluid, the non-wetting fluid will reach residual conditions at after a certain volume has been injected. The saturation near bottom portion of the sandpack after a 0.6 PV waterflood is closer to residual oil conditions than the saturation profile at after a 0.3 PV waterflood. Note that one segment of the sandpack at 0 pV waterflood was not measured.

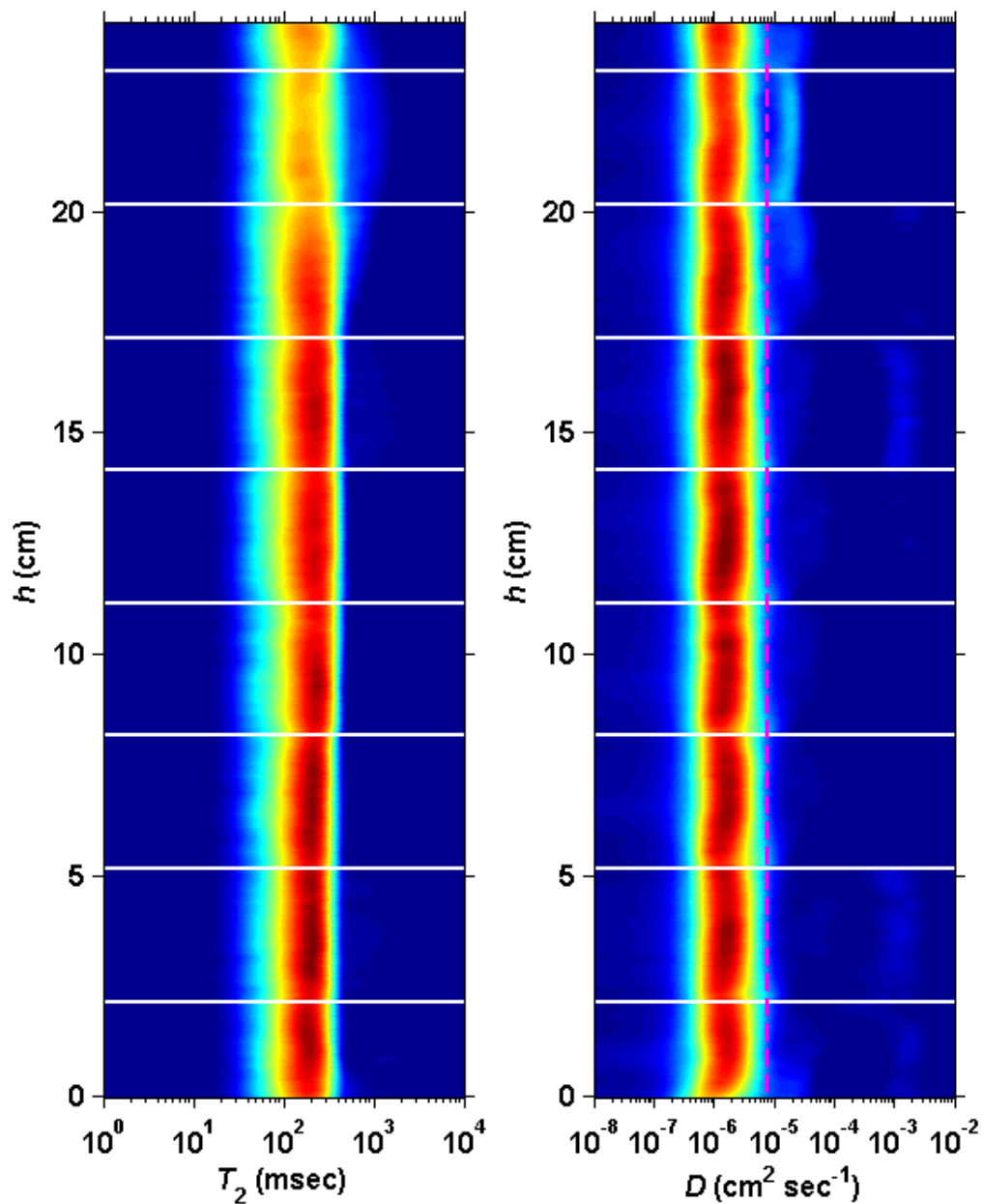


Figure 3.25: T_2 and D projections of D - T_2 profile maps for a sandpack after oilflood. Oilflood was performed at a rate of 40 ft day^{-1} . Horizontal white lines indicate individual measurement regions

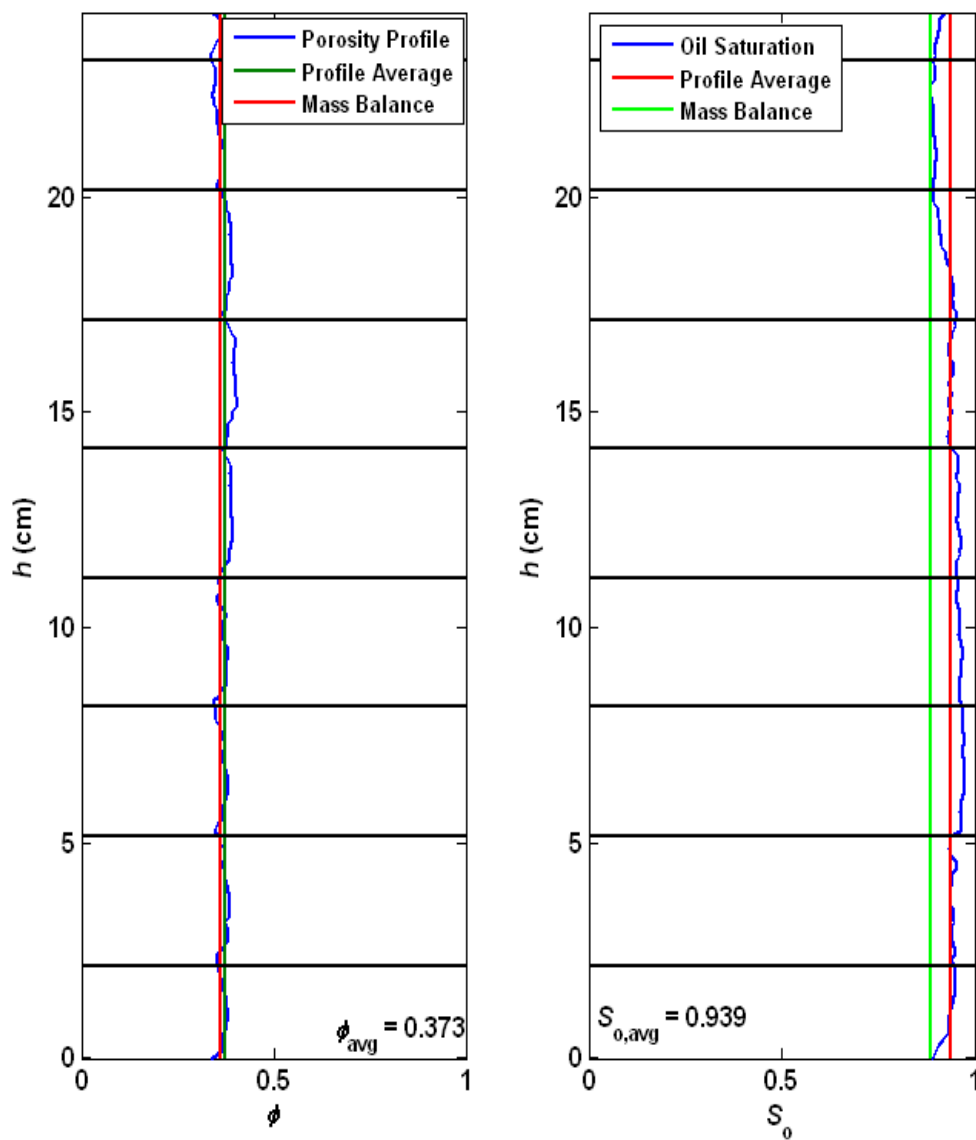


Figure 3.26: Porosity (left) and oil saturation (right) profiles generated from $D-T_2$ profiling measurements. Oilflood was performed at a rate of 40 ft day^{-1} . Horizontal black lines indicate individual measurement regions.

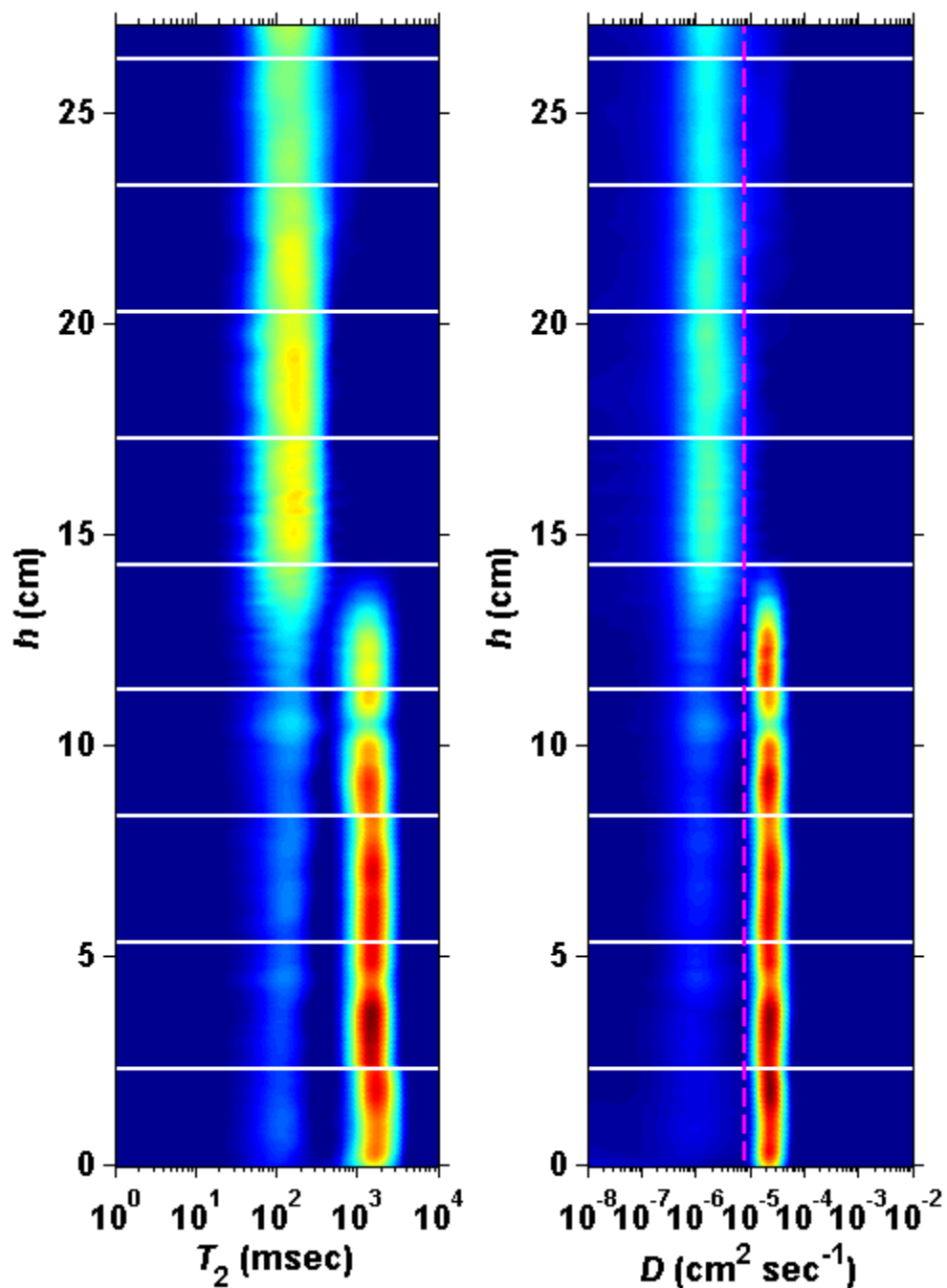


Figure 3.27: T_2 and D projections of D - T_2 profile maps for a sandpack after a 0.3 PV waterflood performed at a rate of 1 ft day^{-1} . Horizontal white lines indicate individual measurement regions

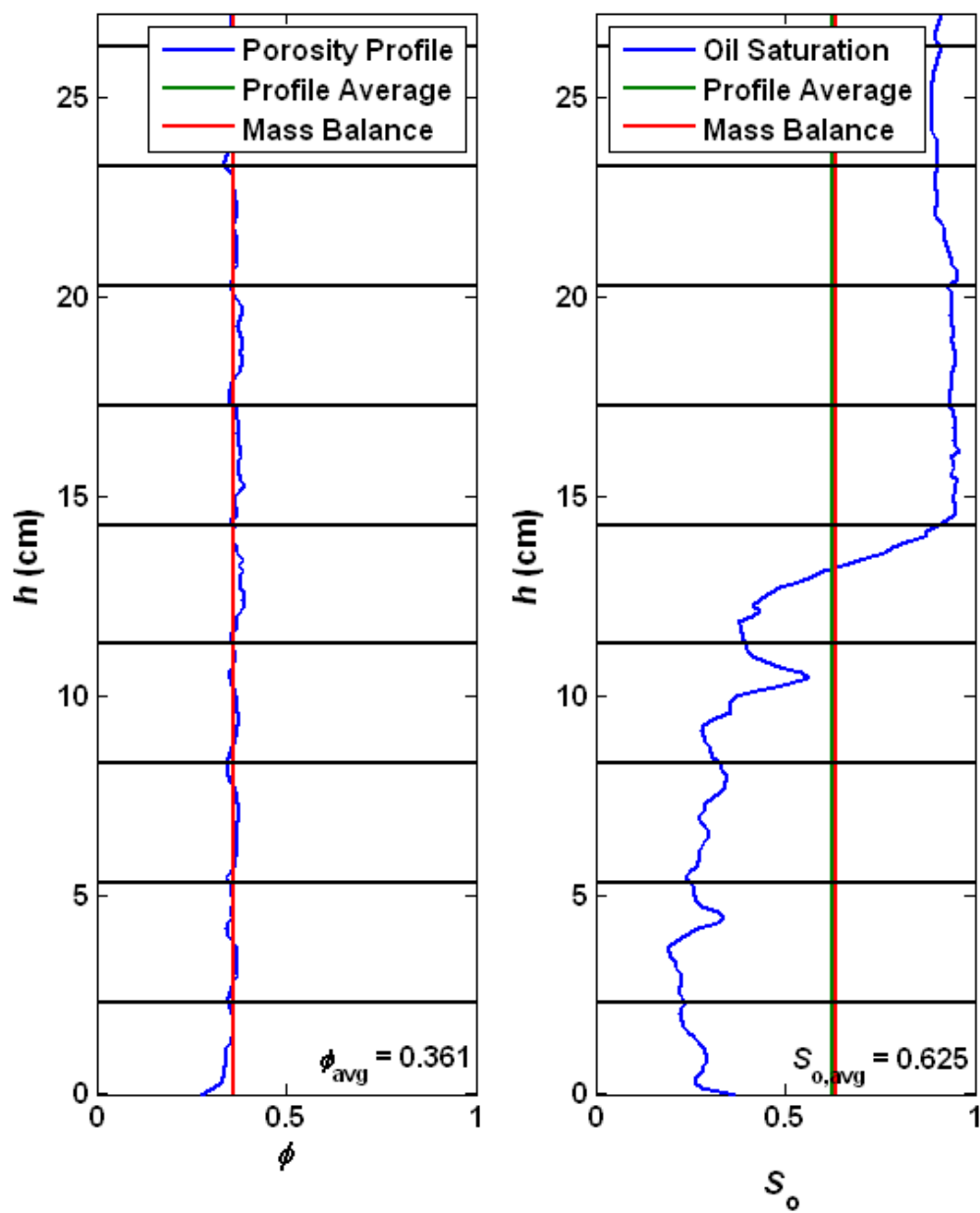


Figure 3.28: Porosity (left) and oil saturation (right) profiles generated from D - T_2 profiling measurements after a 0.3 PV waterflood performed at a rate of 1 ft day^{-1} . Horizontal black lines indicate individual measurement regions.

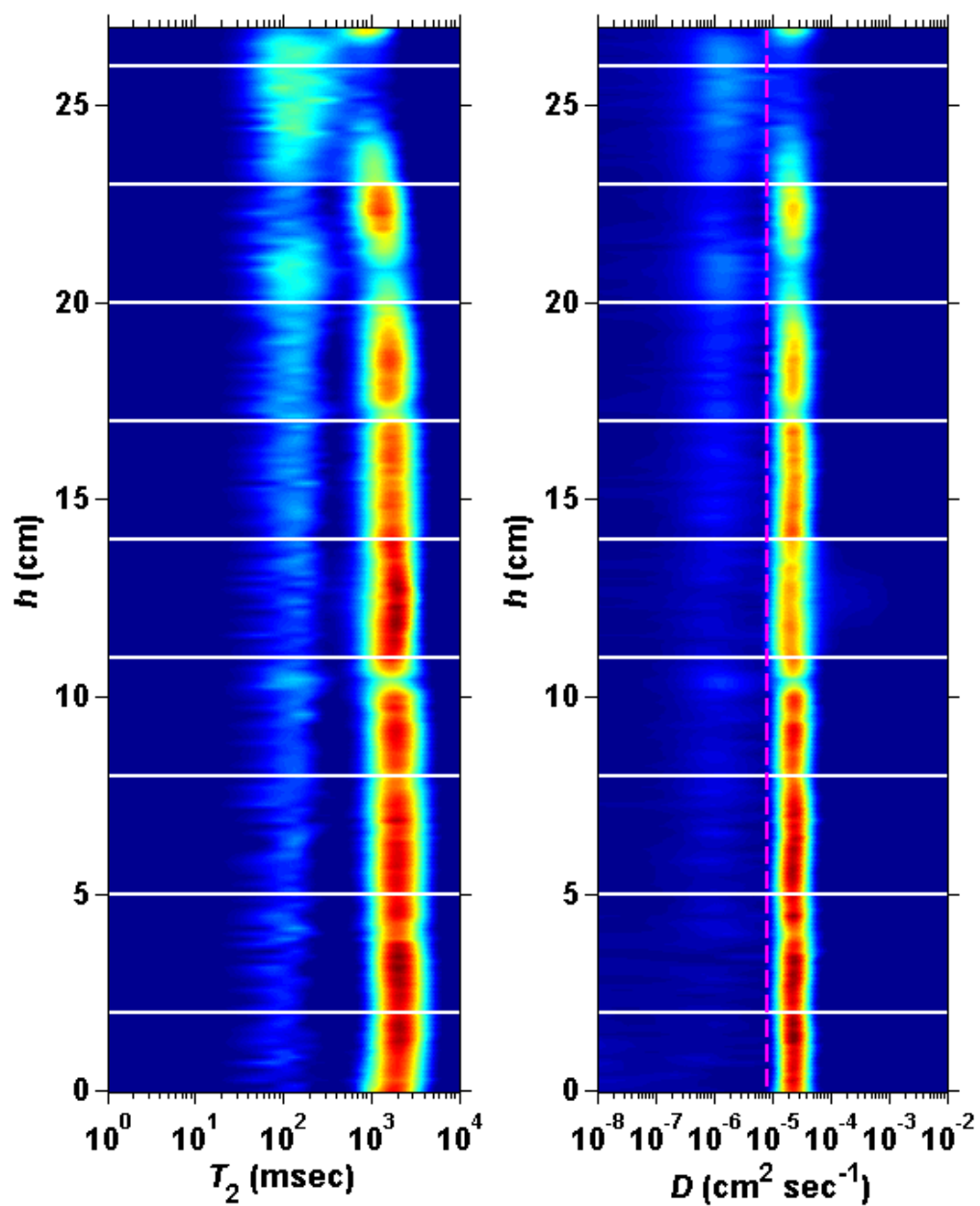


Figure 3.29: T_2 and D projections of D - T_2 profile maps for a sandpack after a 0.6 PV waterflood performed at a rate of 1 ft day⁻¹. Horizontal white lines indicate individual measurement regions

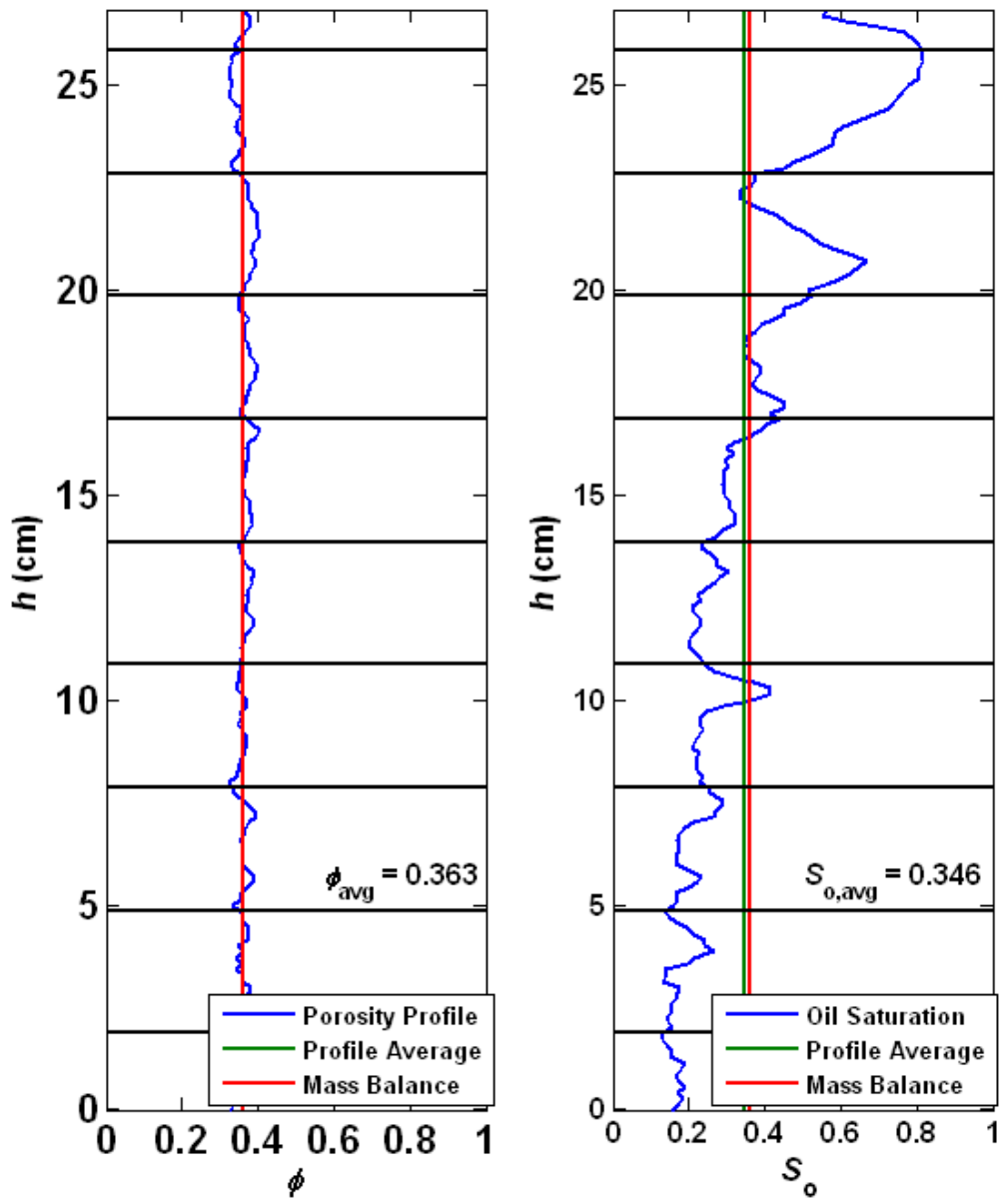


Figure 3.30: Porosity (left) and oil saturation (right) profiles generated from $D-T_2$ profiling measurements after a 0.6 PV waterflood performed at a rate of 1 ft day⁻¹. Horizontal black lines indicate individual measurement regions.

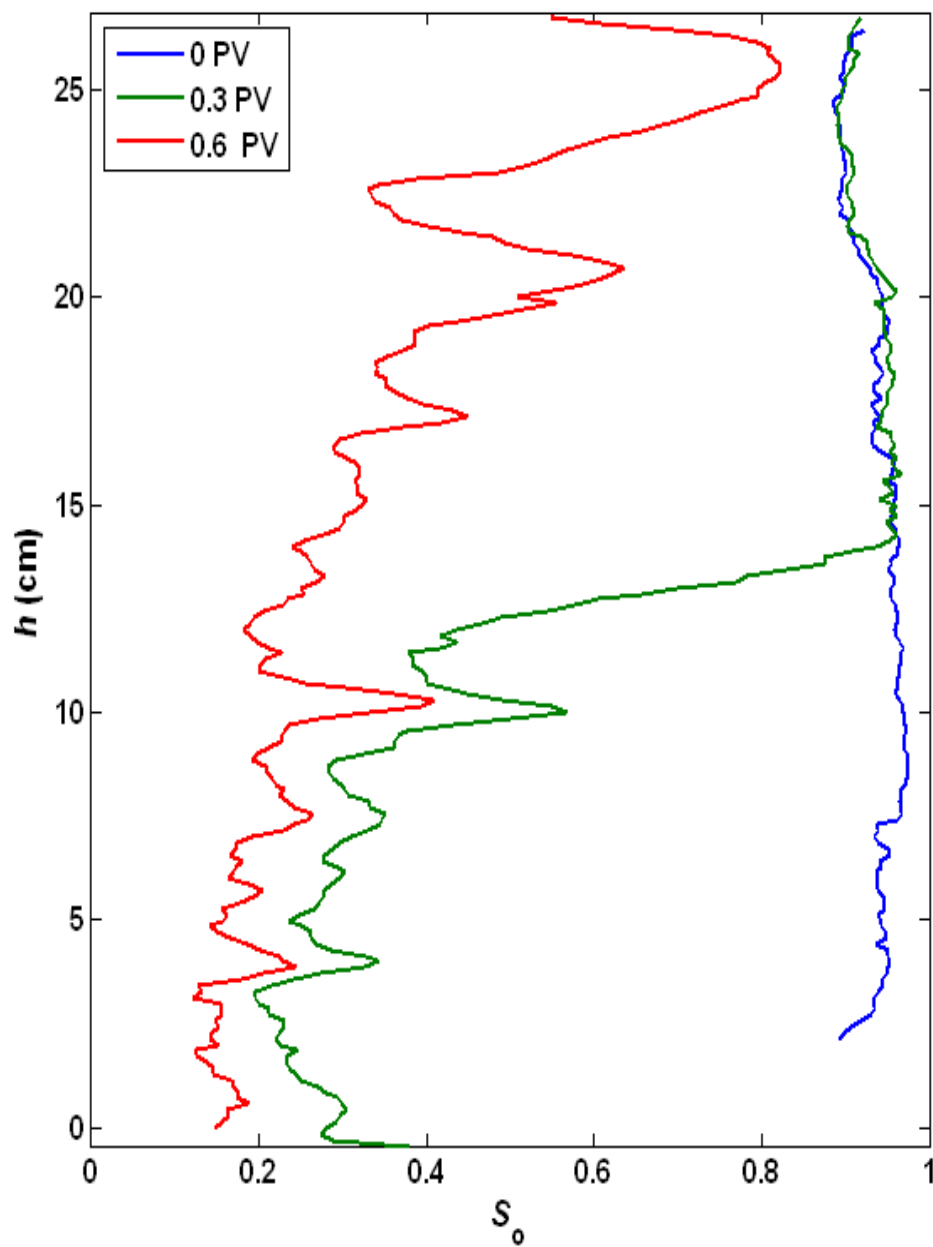


Figure 3.31: Oil saturation profiles after a 0, 0.3, and 0.6 PV waterflood. Note that one segment of the sandpack at 0 pV waterflood was not measured.

3.5 An Alternate Method to Calculate Saturation

The standard approach to determining oil and water saturations from D - T_2 maps has been to select a cutoff value based on the diffusion coefficient. Data that fell above the cutoff was considered to be water and data below the cutoff was said to be oil. However, in some experiments, notably those with low signal to noise, oil and water peaks may overlap and present no clear region to place a cutoff line. In these situations, the placement of the cutoff line can be arbitrary and result in lumping the tail end of one phase in with the other. Therefore, in order to remove the arbitrary nature of selecting a cutoff, the D - T_2 map can be fit to a multi-modal log-normal distribution in order to identify the two phases in the system.

In order to generate a saturation value, the D - T_2 maps can be fit to one of two models: a univariate or bivariate multimodal lognormal distribution. The univariate model relies on fitting data that has been projected onto the D -axis rather than fitting all of the 2-D data. The D and T_2 projections are given by equations (3. 6) and (3. 7), respectively.

$$f_D (D) = \sum_{all\ T_2} f(D, T_2) \quad (3. 6)$$

$$f_{T_2} (T_2) = \sum_{all\ D} f(D, T_2) \quad (3. 7)$$

After the projection has been performed, they are normalized by their area, and then a bimodal lognormal model, $\bar{f}_D(D; \mu, \sigma)$, is fit through the normalized data f_D .

$$\bar{f}_D(D; \mu, \sigma) = \sum_{i=1}^n \frac{w_i}{D\sigma_i\sqrt{2\pi}} \exp\left(\frac{-(\ln D - \mu_i)^2}{2\sigma_i^2}\right) \quad (3.8)$$

Where

$$\sum_{i=1}^n w_i = 1 \quad (3.9)$$

And n is the number of nodes. The fit is performed in Matlab using the built in subroutine `lsqcurvefit`. For a bimodal fit, the fitting parameters are w_1 , σ_1 , σ_2 , and the log means of the two peaks. Figure 3.32 illustrates an example of using this method to fit a distribution of diffusion coefficients. Once the fitting is complete, saturation values can be calculated. The term w_1 is the fraction of the overall signal due to the presence of oil, and $(1-w_1)$ is the contribution due to the presence of water. Therefore, saturation can be determined using the following equation.

$$S_o = \frac{V_{oil}}{V_{oil} + V_{water}} = \frac{\frac{w_1}{HI_{SMY}}}{\frac{w_1}{HI_{SMY}} + (1 - w_1)} \quad (3.10)$$

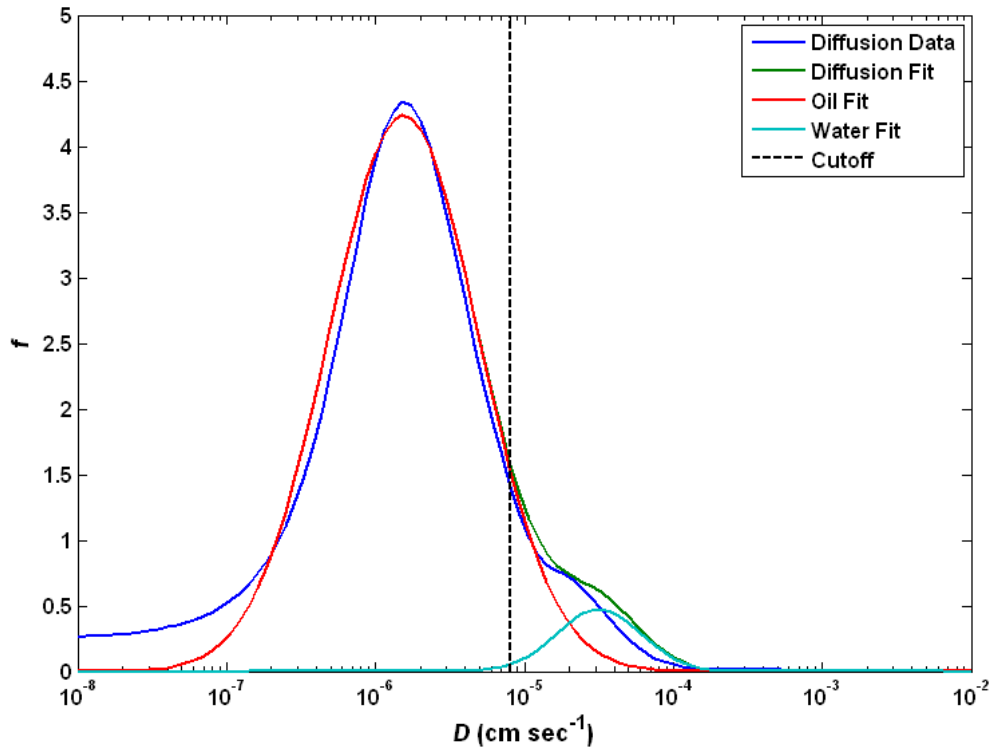


Figure 3.32: Fit results using just the Diffusion Coefficient from sandpack after 0.3 PV waterflood ($h = 22.6$ cm).

The second model fits the 2-D data, $f(D, T_2)$, to a multimodal bivariate lognormal distribution function.

$$\begin{aligned} & \bar{f}_{DT_2}(D, T_2; \mu_D, \sigma_D, \mu_{T_2}, \sigma_{T_2}) \\ &= \sum_{i=1}^n \frac{w_i}{DT_2 \sigma_{D_i} \sigma_{T_2_i} \sqrt{2\pi}} \exp\left(\frac{-(\ln D - \mu_{D_i})^2}{2\sigma_{D_i}^2}\right) \exp\left(\frac{-(\ln T_2 - \mu_{T_2_i})^2}{2\sigma_{T_2_i}^2}\right) \quad (3.11) \end{aligned}$$

Where

$$\sum_{i=1}^n w_i = 1 \quad (3.12)$$

And n is the number of nodes. This fit is again performed in Matlab using the built in subroutine `lsqcurvefit`. However, a large portion of the data contained in the D - T_2 map corresponds to values of zero. Therefore, the range of the data is restricted so the relevant portion of the map is sent to the fitting algorithm. This region is found by analyzing the projected data f_D and f_{T_2} . The region of interest (ROI) is determined to be

$$f_{D,ROI}(D) > 0.001 \max [f_D(D)] \quad (3.13)$$

$$f_{T_2,ROI}(T_2) > 0.001 \max [f_{T_2}(T_2)] \quad (3.14)$$

The green box in Figure 3.33 shows an example of the ROI used in the fit of a D - T_2 map.

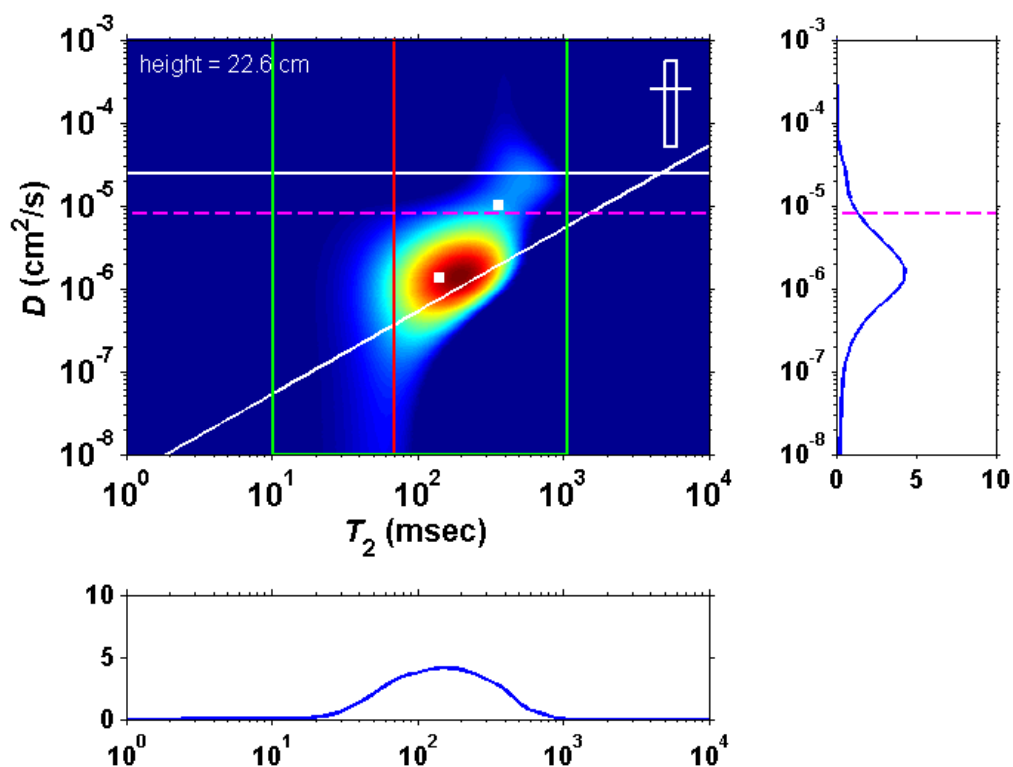


Figure 3.33: D - T_2 map taken from a profile of a sandpack after a 0.3 PV waterflood ($h = 22.6$ cm). The green box denotes the region of interest for the bivariate, bimodal fit. The white squares show the resulting log means from the fit.

For a bimodal fit, the fitting parameters are w_1 , $\sigma_{D,1}$, $\sigma_{D,2}$, $\sigma_{T_2,1}$, $\sigma_{T_2,2}$ and the D and T_2 log means of the first and second peaks. Once the fit parameters have been optimized the saturation can be again calculated as illustrated previously. Figure 3.34 shows the resulting fit for the D - T_2 map presented in Figure 3.33. Figure 3.35 shows the same results as Figure 3.34, but the data and resulting fits have been projected onto the T_2 (top pane) and D axes (bottom pane).

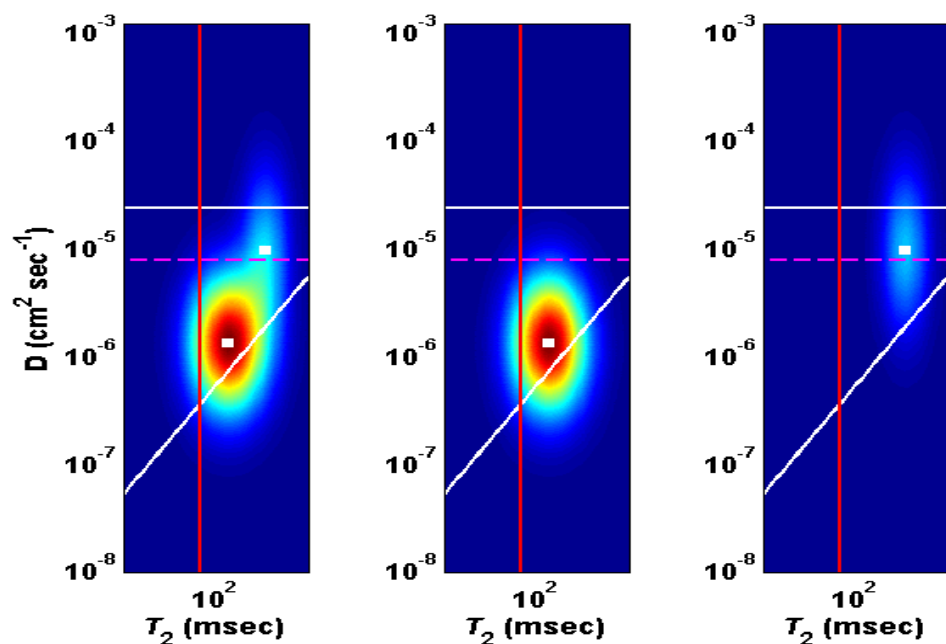


Figure 3.34: D - T_2 fitting results of data presented in Figure 3.33. The bimodal, bivariate fit is depicted (left) as well as the contribution from each phase: oil (center) and water (right).

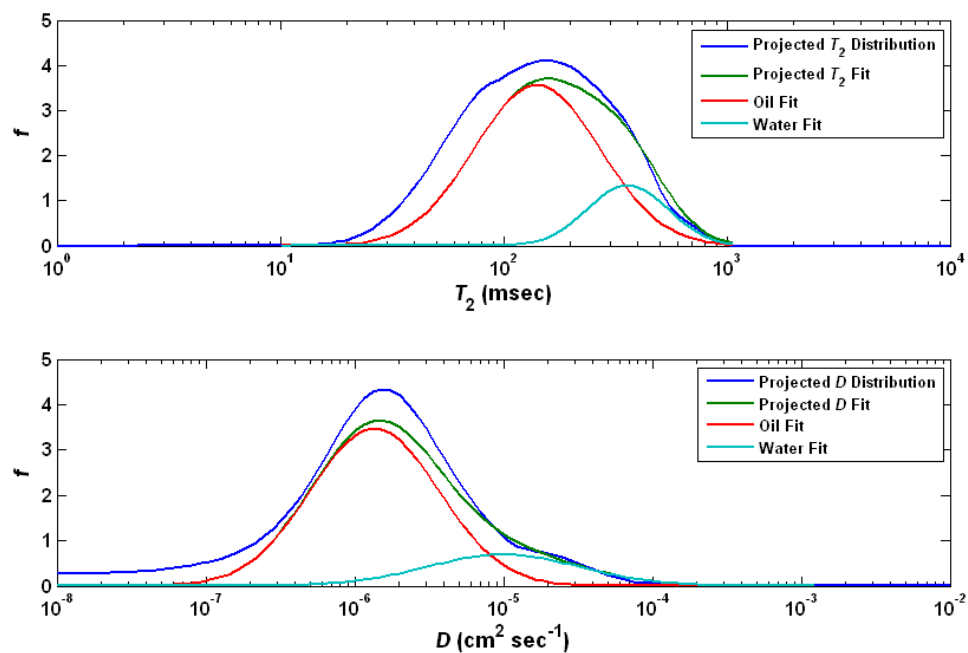


Figure 3.35: D - T_2 fitting results of data in Figure 3.33 presented as projections onto T_2 (top) and D (bottom) axes.

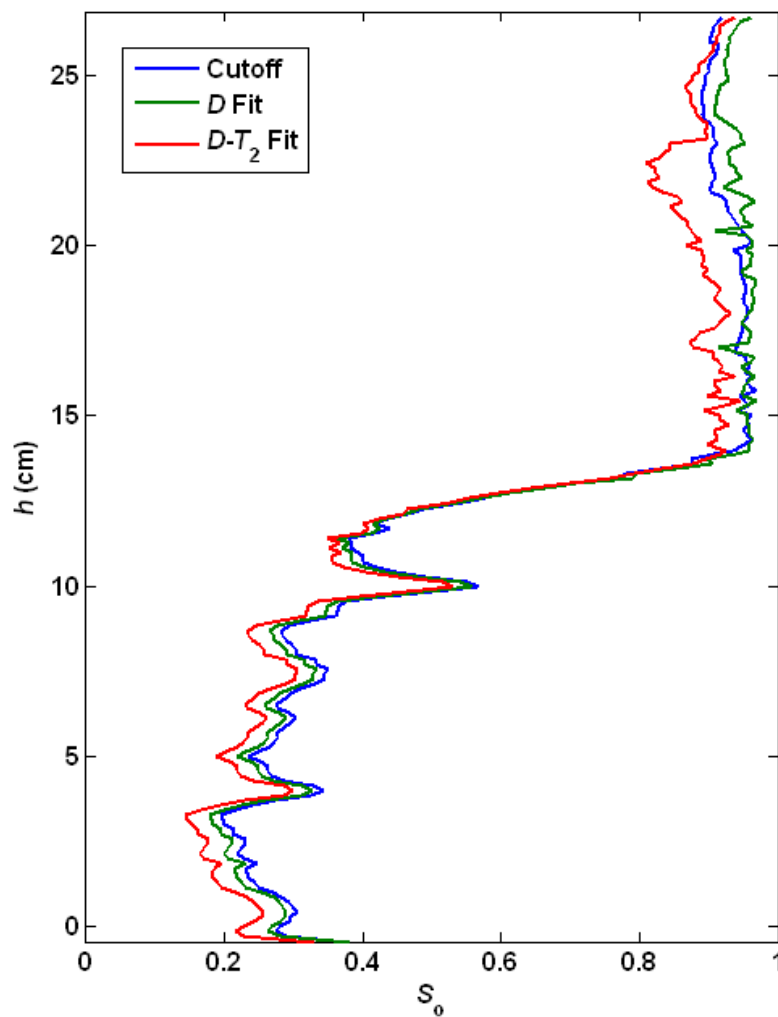


Figure 3.36: Comparison of a saturation profile calculated using fitting and cutoff methods.

Figure 3.36 shows the saturation profiles after 0.3 PV waterflood calculated using three different methods: cut-off, fitting the diffusion coefficient, and fitting both D and T_2 . The cutoff method yield an average oil saturation of 0.625 while the D and $D-T_2$

fitting methods yielded average oil saturations of 0.631 and 0.590, respectively. The fitting and cutoff methods yield very similar results for the saturation profiles. However, the most noticeable difference is that the fitting methods estimate the oil saturation to be slightly lower in the region with low oil saturation. Furthermore, in the region of high oil saturation, all three methods start to show slight deviation from one another. For the D fit, the saturation is determined to be slightly higher in the region of high oil saturation in comparison to the cutoff saturation. This may result when oil and water peaks slightly overlap, and application of the cutoff method results in a portion of one phase to be confused with the other. For instance, Figure 3.32 shows the fitting of distribution of diffusion coefficients at the top of the sandpack in an area of high oil saturation. The cutoff used is near the minimum between the two peaks of the distribution, and everything to the right is considered water and to the left oil. However, the fit generated an oil peak with a large tail that crosses the line used in the cutoff procedure. The portion of the tail crossing the cutoff line results in a slightly higher oil saturation in this region of the sandpack for the fitting method. However, the D - T_2 fit shows a much lower oil saturation near the top of the sandpack than the cutoff or D fit methods. In an effort to fit both D and T_2 simultaneously, a broad distribution is fit to the water signal in order to compensate for a nearly featureless T_2 distribution. Including data that adds no new information produces poorer fitting results.

Table 3.4: Quality of fit for D and D - T_2 fitting methods for the determination of saturation

	L_2 Norm	
	Set of Vials	0.3 PV Waterflood
D Fit	0.58	0.11
D - T_2 Fit	1.20	0.89

In order to determine which method, fitting of the just the distribution of diffusion coefficients versus the $D-T_2$ map, yielded the better saturation profile both methods were applied to two different systems. The first system is a collection of vials with varying heights of oil and water in order to produce varying saturation levels across the sample ($S_o = 1.0, 0.5, 0.33,$ and 0.25 from top to bottom). The results for this experiment are illustrated in Figure 3.37. The second system is the sandpack after 0.3 PV waterflood. In both cases, the saturation profile generated via the cutoff method was compared with results from both fits. Also, the L2-norm between the fit and the data was calculated for both cases and is presented in Table 3.4. In both instances, the fit of the diffusion coefficient yielded a better saturation profile in terms of the accuracy in determining saturation (Figure 3.37) and the closeness of fit (smaller L2-norm).

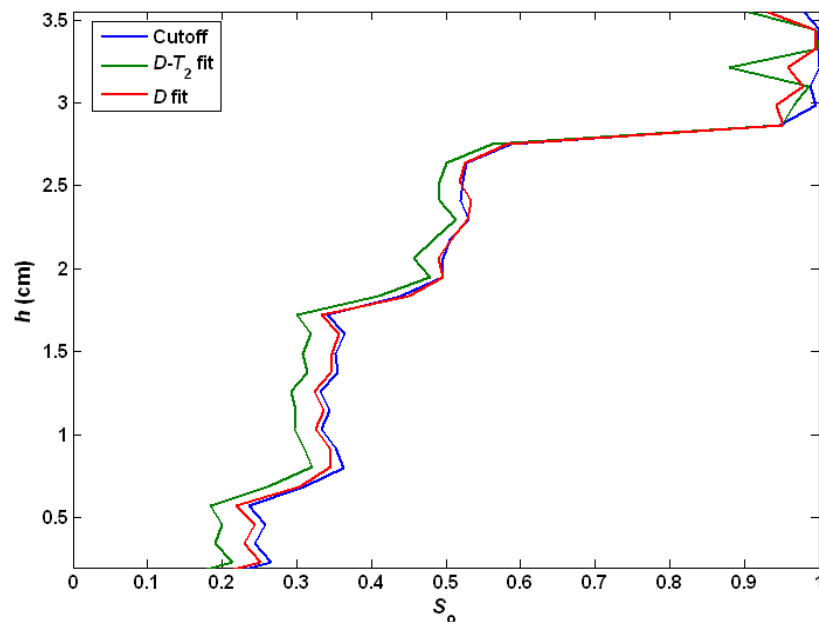


Figure 3.37: Comparison of a saturation profile calculated using fitting and cutoff methods for a system of vials with varying heights of water and SMY crude oil.

Two other examples are presented in Figure 3.38 and Figure 3.40. Both examples relying on fitting just the diffusion data because it yielded a better fit and is less time intensive in comparison to simultaneously fitting both D and T_2 . In Figure 3.38, the saturation profile for a water saturated sandpack is shown. The saturation profile generated via the cutoff method has many unexpected peaks caused by a slight smearing of the water peak below the oil-water cutoff line. When using the fitting method, most of the peaks are removed; however, one is still noticeably present. Figure 3.39, shows the fit at $h = 17.02$ cm where the large peak appears in the saturation profile. The distribution has a single peak corresponding to the diffusivity of water. However, the distribution has a long tail with low amplitude. When applying a bimodal fit to this distribution, one mode is fit to the tail while the other mode corresponds to water peak. Therefore, the large peak present in the saturation profile arises from the fitting of an artifact in the D distribution.

Also, Figure 3.40 shows the sandpack after a 0.6 PV waterflood. The cutoff method yielded an average oil saturation of 0.35, and the fitting method produced a slightly lower average oil saturation of 0.34 ($S_o = 0.36$ by mass balance) while exhibiting the same features demonstrated by the cutoff method.

This approach to calculating saturation offers an alternative method for determining saturation from D-T2 maps. The cutoff method requires an arbitrary division between oil and water. This is a reasonable approach when the response from the two phases can be distinguished readily. However, in cases with low signal to noise, the water and oil peaks often overlap, and this method allows for the determination of saturation without the need for an arbitrary selection parameter such as a cutoff. Saturation profiles generated using this approach reduced erroneous peaks identified

using the cutoff method on a water saturated sandpack and confirmed the saturations measured via mass balance. However, caution must be used in the application of this technique especially in measurements in which restricted diffusion is noted (Wayne & Cotts, 1966) (Flaum, Hirasaki, Flaum, & Straley, 2005).

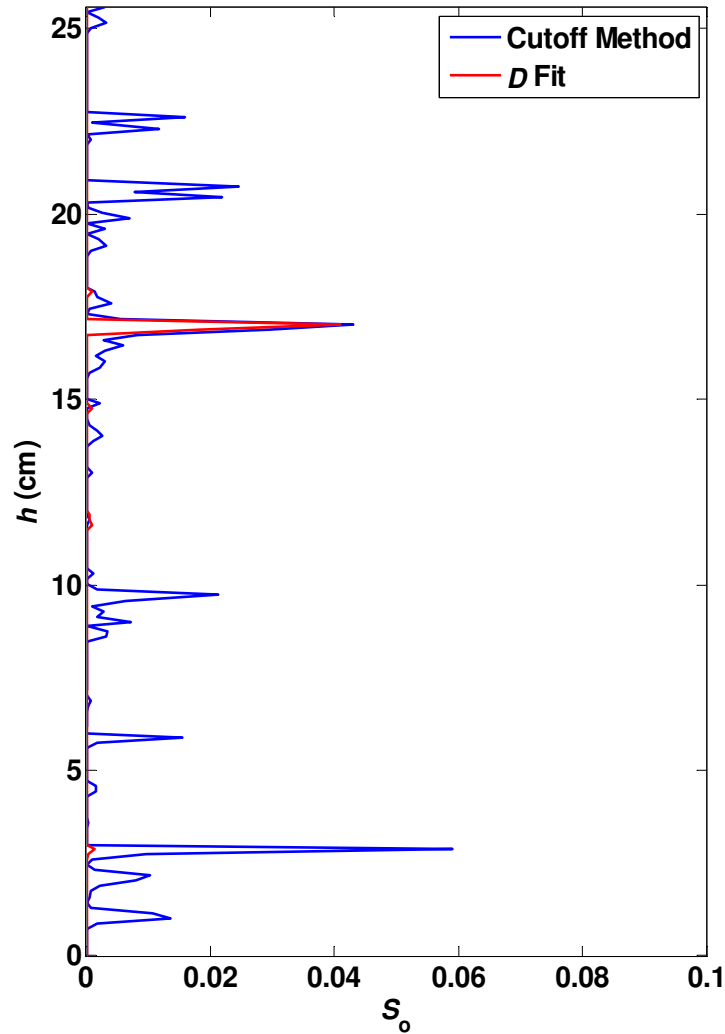


Figure 3.38: Saturation Profile of a water saturated sandpack. Most of the peaks generated when using the cutoff method are removed by fitting the diffusion coefficient.

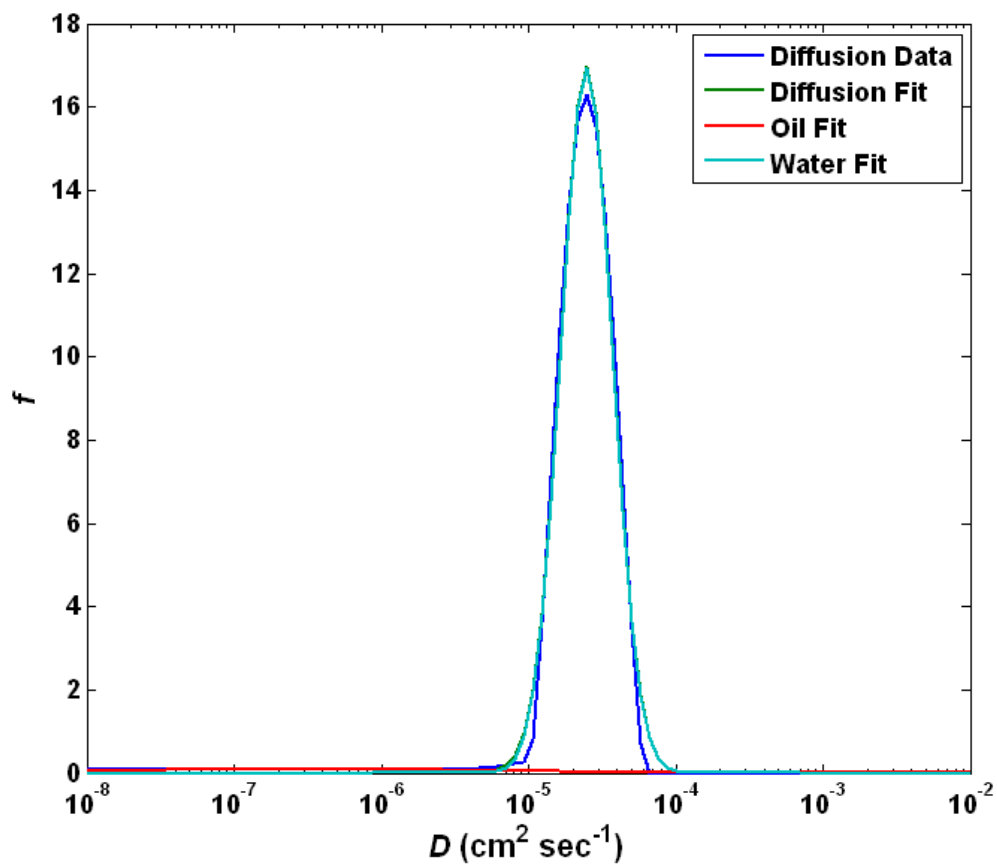


Figure 3.39: Fitting result from the water saturated sandpack at $h = 17.02$ cm (location corresponding to large spike in saturation profile, Figure 3.38)

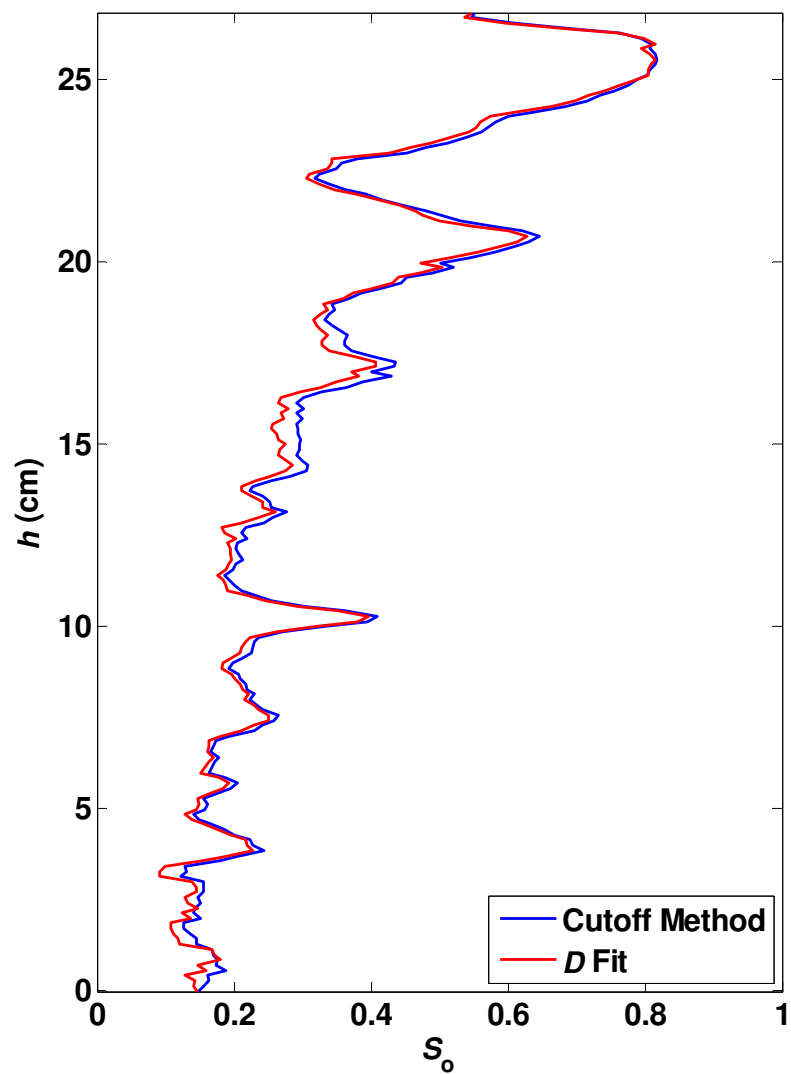


Figure 3.40: Saturation Profile of a sandpack after a 0.6PV waterflood. Both methods yield a saturation profile with similar features, but the fitting method yields lower oil saturation.

3.6 Summary

In this chapter, the design and development of an imaging analogue to diffusion editing is presented. The most notable features of the pulse sequence are the bipolar gradient pulses implemented to make the measurement sensitive to diffusion and the inclusion of a $(\pi/2)_y$ RF pulse applied when the first echo peak reaches its peak. Both features are included in order to improve phase stability of the acquired signal. When implemented, the bipolar diffusion gradient produces a stable and well shaped echo in comparison to the unipolar gradient. Then, the $(\pi/2)_y$ RF pulse flips the out-phase signal onto the longitudinal axis prior to the measurement of T_2 with the train of refocusing pi pulses.

In addition to the structural components of the pulse sequence, the impact of the parameters on the measurement is addressed. Some parameters, like the number of gradient prepulses and RF-gradient spacing, directly impact the quality of the NMR signal while others, namely the diffusion gradient list, impact the experimental duration.

The applicability of generating D - T_2 profiles using the pulse sequence presented in Figure 3.1 was examined by analyzing bulk fluids and a sandpack at various stages of the flooding process. Results generated from both systems show that the proposed pulse sequence can correctly quantify the volume of oil and water present in a given sample.

Chapter 4

Conclusions and Future Work

4.1 Conclusions

Presented in the preceding chapters are two new pulse sequences designed for a low-field NMR spectrometer along with guidelines needed in selecting appropriate experimental parameters. Both T_2 and D - T_2 profiling rely on the application of frequency-encoding gradients to impart spatial sensitivity to these NMR measurements. Frequency-encoding gradients allow several things to be accomplished. First, it allows for a profile to be generated for a sample spanning the length of the spectrometer's sweet spot without the need for multiple slice selective measurements. Second, utilizing a pulsed gradient as opposed to a pseudostatic gradient, as in the application of a slice selective CPMG, the sensitivity to diffusion due to the imaging process can be minimized, and the heat generated in the gradient coils greatly reduced. However, the time needed to switch on and off the frequency-encoding gradient forces the need for longer echo spacings which may result in the loss of some of the faster relaxing components of the sample.

As discussed in Chapter 2, the RARE experiment is an imaging analogue to the CPMG measurement, and therefore, T_2 can be determined as a function of sample height.

This was demonstrated for various samples including bulk fluids and core samples. For core samples, it allows for the determination of porosity and the identification of changes in the pore structure as a function of the core's height. But its usefulness is limited to system in which each NMR sensitive phase possesses a unique, non-overlapping T_2 distribution.

In order to be able to analyze a broad set of systems, imaging capabilities were incorporated into a diffusion editing sequence. Chapter 3 discusses some of the difficulties encountered and presents possible solutions. The approaches taken to prevent signal degradation were found to be suitable for the instrument used in this study. Design of a $D-T_2$ profiling pulse sequence on another low-field spectrometer may or may not require some of the techniques introduced in Chapter 3. However, the methodology presented can be used as a guide for cataloguing and fixing problematic behavior once it has been identified.

Diffusion editing allows for a wealth of information to be collected from a sample. Now, $D-T_2$ profiling extends these abilities and allows for the determination of diffusivity-relaxation distributions as a function of sample height. By using $D-T_2$ profiling, two fluids, water and SMY, could be distinguished based upon their diffusion coefficients along the length of a 1 foot long sandpack. The NMR determined saturation profiles extracted from $D-T_2$ profiling data yielded profiles with averages very close to the average saturations determined via mass balance at various stages within the flooding process. Furthermore, the displacement behavior as described by the saturation profile presents a reasonable depiction of the oilflood and subsequent waterflood. During the oilflood, the presence of an end-effect near the outflow end of the sandpack corresponded

well with the dimensionless capillary end-effect number, $N_{C,end}$. During the water flood, the first 0.3 PV of injected water advanced near the center of the column which is clearly evident in the NMR saturation profile. The next 0.3PV injection saw the breakthrough of water from the column and the corresponding saturation profile confirms that the oil saturation near the outlet is below the initial oil saturation. The peaks noted in the saturation profile after 0.6 PV waterflood may be indicative of viscous fingering. Furthermore, near the inlet of the sand pack, the saturation has reduced demonstrating that after the initial 0.3 PV waterflood, the swept region at the bottom of the column had not yet reached residual oil conditions, but that after a 0.6 PV waterflood, the lower region of the sandpack is near residual oil conditions.

4.2 Future Work

The application of imaging pulse sequences using low-field NMR can be applied to wide range of experiments and systems. Both T_2 and $D-T_2$ profiles can be used to examine properties including, but are not limited to, the heterogeneity, fluid configuration, wettability, and pore structure of a core sample. For instance, the RARE sequence could be a powerful tool in the analysis of porosity and pore structure. Application of the RARE experiments on a water saturated core sample can provide information of the porosity and pore size, but can also quantify the degree of heterogeneity in pore structure along the length of the core. By measuring T_2 distributions after centrifuge experiments of water saturated core samples, pore

connectivity can be studied (Moctezuma, Békri, Laroche, & Vizika, 2003). Instead of relying on a CPMG measurement, the RARE pulse sequence not only provides an estimate of pore vug connectivity, but can be used to help locate connected and dead vugs within the porous media.

The D - T_2 profiling experiment also could be used to examine pore structure. By performing restricted diffusion analysis with the D - T_2 profiling sequence pore structure and connectivity could be studied. However, one of the strongest abilities of D - T_2 profiling is to distinguish phases with overlapping T_2 distributions base when the phases have unique self-diffusion coefficients. Therefore, the most robust tool for profiling core samples partial saturated with water and oil is the D - T_2 profiling experiment. Recent experiments have utilized the measurement of water/air saturation profiles to generate water/air capillary pressure curves. Instead of measuring saturation after many centrifuge experiments, a few, moderate velocities are chosen for the centrifuge experiments, and the resulting air/water saturation profiles are used in construction of water/air capillary pressure curves (Chen & Balcom, 2005) (Lindsay, Cornwall, & Green, 2009). By using D - T_2 profiling experiments, a similar methodology may be implemented to construct water/oil capillary pressure curve. D - T_2 profiling could also be implemented in order to study the displacement process through heterogeneous porous media including oilflood, waterflood, and enhanced oil recovery (EOR) processes to examine not only saturation profiles of remaining oil, but in what pores the oil may be located.

Emulsions offer another avenue of study with the T_2 and D - T_2 profiling. A single spin echo imaging sequence has been utilized in effort to determine the water and oil content of an emulsion (Jiang, Hirasaki, Miller, Moran, & Fleury, 2007). However, T_2

and $D-T_2$ profiling are able to provide larger amounts information about the emulsion. For instance, not only could water and oil fractions be determined as a function of height, but also information could be determined about the drop size distribution of the emulsion as a function of sample height.

References

- Alsop, D. (1997). Phase insensitive preparation of single-shot RARE: Application to diffusion imaging in humans. *Magnetic Resonance in Medicine* , 38, 527-533.
- Baldwin, B., & Yamanashi, W. (1986). Detecting fluid movement and isolation in reservoir core with medical NMR imaging techniques. *SPE Reservoir Engineering* , 4 (2), 207-212.
- Bear, J. (1972). *Dynamics of fluids in porous media*. New York: Dover Publications, Inc.
- Bernstein, M., King, K., & Zhou, X. (2004). *Handbook of MRI pulse sequences*. Amsterdam: Elsevier Academic Press.
- Blackband, S., Mansfield, P., Barnes, J., Clague, A., & Rice, S. (1986). Discrimination of crude oil and water in sand and in bore cores with NMR imaging. *SPE Formation Evaluation* , 1 (1), 31-34.
- Bloch, F., Hansen, W., & Packard, M. (1946). Nuclear induction. *Physical Review* , 69 (3-4), 127.
- Callaghan, P. (1991). *Principles of nuclear magnetic resonance microscopy*. New York: Oxford University Press, Inc.
- Chen, Q., & Balcom, B. (2005). Capillary curve measurements using a single moderate-speed centrifuge and quantitative magnetic resonance imaging. *Presented at the International Symposium of the Society of Core Analyst*. Toronto, Canada.
- Chen, Q., Butler, K., Gingras, M., & Balcom, B. (2005). A mechanism study of a co-current and counter-current imbibition using new magnetic resonance techniques. *Presented at the International Symposium of the Society of Core Analyst*. Toronto, Canada.
- Chen, S., Kim, K., Qin, F., & Watson, A. (1992). Quantitative NMR imaging of multiphase flow in porous media. *Magnetic Resonance Imaging* , 10, 815-826.
- Cheng, Y. M., MacGregor, R., & Balcom, B. (2005). Direct detection of hydrocarbon displacement in a model porous soil with magnetic resonance imaging. *Analytical Chemistry* , 77, 1824-1830.
- Cheng, Y., Huang, Q., Eic, M., & Balcom, B. (2005). CO₂ dynamic adsorption/desorption on zeolite 5A studied by ¹³C magnetic resonance imaging. *Langmuir* , 21, 4376-4381.
- Chuah, T.-L. (1996). *Estimation of relaxation time distributions for NMR CPMG measurements*. Doctoral Dissertation, Rice University, Houston, TX.

- Coates, G., Xiao, L., & Prammer, M. (1999). *NMR logging: Principles & applications*. Houston, TX: Gulf Publishing Company.
- Cotts, R., Hoch, M., Sun, T., & Markert, J. (1989). Pulsed field gradient stimulated echo method for improved NMR diffusion measurement in heterogeneous systems. *Journal of Magnetic Resonance* , 83 (2), 252-266.
- Edelstein, W., Vineagr, H., Tutunjian, P., Roemer, P., & Mueller, O. (1988). NMR imaging for core analysis. *Presented at SPE Annual Technical Conference and Exhibition*. Houston, TX.
- Fauth, J.-M., Schweiger, A., Braunschweiler, L., Forrer, J., & Ernst, R. (1986). Elimination of unwanted echoes and reduction of dead time in three pulse electron spin-echo spectroscopy. *Journal of Magnetic Resonance* , 66, 74-85.
- Flaum, M. (2007). *Fluid and rock characterization using new NMR diffusion-editing pulse sequences and two dimensional diffusivity-T2 maps*. Doctoral Dissertation, Rice University, Houston, TX.
- Flaum, M., Chen, J., & Hirasaki, G. (2004). NMR diffusion editing for D-T2 maps: Application to recognition of wettability change. *SPWLA 45th Annual Logging Symposium*. Noordwijk, Netherlands.
- Flaum, M., Hirasaki, G., Flaum, C., & Straley, C. (2005). Measuring pore connectivity by pulsed field gradient diffusion editing with hydrocarbon gases. *Magnetic Resonance Imaging* , 23 (2), 337-339.
- Fordham, E., Hall, L., Ramakrishnan, T., Sharpe, M., & Hall, C. (1993). Saturation gradients in drainage of porous media: NMR imaging measurements. *AIChE Journal* , 39 (9), 1431-1443.
- Freedman, R., Heaton, N., Flaum, M., Hirasaki, G. F., & Hürlimann, M. (2003). Wettability, saturation, and viscosity from NMR measurements. *SPE Journal* , 8 (4), 317-327.
- Gounarides, J., Chen, A., & Shapiro, M. (1999). Nuclear magnetic resonance chromatography: applications of pulse field gradient diffusion NMR to mixture analysis and ligand-receptor interactions. *Journal of Chromatography B* , 725, 79-90.
- Green, D., Dick, J., McAloon, M., de J. Cano-Barrita, P., Burger, J., & Balcom, B. (2008). Oil/water imbibition and drainage capillary pressure determined by MRI on a wide sampling or rocks. *Presented at the International Symposium of the Society of Core Analyst*. Abu Dhabi, UAE.
- Hahn, E. (1950). Spin echoes. *Physical Review* , 80 (4), 580-594.

- Henning, J., Nauerth, A., & Friedburg, H. (1986). RARE imaging: A fast imaging method for clinical MR. *Magnetic Resonance in Medicine*, 3, 823-833.
- Hoult, D., & Richards, R. (1975). Critical factors in the design of sensitive high resolution nuclear magnetic resonance spectrometers. *Proceedings of the Royal Society of London. Series A, Mathematical and Physical Sciences*, 344 (1638), 311-340.
- Hürlimann, M., & Venkataramanan, L. (2002). Quantitative measurements of two-dimensional distribution functions of diffusion and relaxation in grossly inhomogeneous fields. *Journal of Magnetic Resonance*, 157 (1), 31-42.
- Hürlimann, M., Flaum, M., Venkataramanan, L., Flaum, C., Freedman, R., & Hirasaki, G. (2003). Diffusion-relaxation distribution functions of sedimentary rocks in different saturation states. *Magnetic Resonance Imaging*, 21, 305-310.
- Jiang, T., Hirasaki, G., Miller, C., Moran, K., & Fleury, M. (2007). Diluted bitumen water-in-oil emulsion stability and characterization by nuclear magnetic resonance (NMR) measurements. *Energy & Fuels*, 21, 1325-1336.
- Johannesen, E., Howard, J., & Graue, A. (2008). Evaluation of wettability distributions in experimentally aged cores. *Presented at the International Symposium of the Society of Core Analyst. Abu Dhabi, UAE.*
- Johns, M., & Gladden, L. (1998). MRI study of non-aqueous phase liquid extraction from porous media. *Magnetic Resonance Imaging*, 15 (5/6), 655-657.
- Lauterbur, P. (1973). Image formation by induced local interactions: Examples employing nuclear magnetic resonance. *Nature*, 242 (5394), 190-191.
- Le Bihan, D., Poupon, C., Amadon, A., & Lethimonnier, F. (2006). Artifacts and pitfalls in diffusion MRI. *Journal of Magnetic Resonance Imaging*, 24 (3), 478-488.
- Liang, Z., & Lauterbur, P. (2000). *Principles of magnetic resonance imaging: A signal processing perspective*. New York: IEEE Press.
- Lindsay, C., Cornwall, C., & Green, D. Acquisition of core capillary pressure data by in-situ saturation monitoring: A comparative evaluation. *Presented at the International Symposium of the Society of Core Analyst. Noordwijk, The Neatherlands.*
- Mandava, S., Watson, A., & Edwards, C. (1990). NMR imaging of saturation during immiscible displacements. *AIChE Journal*, 36 (11), 1680-1686.
- Merboldt, K., Hänicke, W., & Frahm, J. (1985). Self-diffusion NMR-imaging using stimulated echoes. *Journal of Magnetic Resonance*, 64 (3), 479-486.

- Moctezuma, A., Békri, S., Laroche, C., & Vizika, O. (2003). A dual network model for relative permeability of bimodal rocks: Application in vuggy carbonate. *Presented at the International Symposium of the Society of Core Analyst*. Pau, France.
- Mohanty, K., & Miller, A. (1991). Factors influencing unsteady relative permeability of mixed-wet reservoir rock. *SPE Formation Evaluation* , 6 (3), 349-358.
- Neeman, M., Freyer, J., & Sillerud, L. (1990). Pulsed-gradient spin-echo diffusion studies in NMR imaging: Effects of the Imaging gradients on determination of diffusion coefficients. *Journal of Magnetic Resonance* , 90 (2), 303-312.
- Purcell, E., Torrey, H., & Pound, R. (1946). Resonance absorption by nuclear magnetic moments in a solid. *Physical Review* , 69 (1-2), 37-38.
- Quan, C., Weimin, W., & Xianchun, C. (1996). Application of NMR imaging to steam foam flooding in porous media. *Magnetic Resonance Imaging* , 14 (7/8), 949-950.
- Riskedal, H., Tipura, L. H., & Graue, A. (2008). NMR monitoring of spontaneous brine imbibition in carbonates. *Presented at the International Symposium of the Society of Core Analyst*. Abu Dhabi, UAE.
- Scheenen, T., Van Dusschoten, D., De Jager, P., & Van As, H. (2000). Microscopic displacement imaging with pulsed field gradient turbo spin-echo NMR. *Journal of Magnetic Resonance* , 142 (2), 207-215.
- Stapf, S., & Han, S. (Eds.). (2006). *NMR Imaging in chemical engineering*. Weinheim, Germany: Wiley-VCH Verlag GmbH & Co. KGaA.
- Stejskal, E., & Tanner, J. (1965). Spin diffusion measurements: Spin-echoes in the presence of a time-dependent field gradient. *The Journal of Chemical Physics* , 42 (1), 288-292.
- Tanner, J. (1970). Use of stimulated echoes in NMR diffusion studies. *The Journal of Chemical Physics* , 52 (5), 2523-2526.
- Torrey, H. (1956). Bloch equations with diffusion terms. *Physical Review* , 104 (3), 563-565.
- Wayne, R., & Cotts, R. (1966). Nuclear-magnetic-resonance study of self-diffusion in bounded medium. *Physical Review* , 151 (1), 264-272.
- Zhang, Q. (2001). *NMR formation evaluation: hydrogen index, wettability and internal field gradients*. Doctoral Dissertation, Rice University, Houston, TX.

Appendix

This appendix address the Matlab code to be implemented in the processing of RARE or $D-T_2$ profiling data. The first section covers the subprograms and subroutines needed to handle the data. The second and third sections address the operation of the code to produce either a T_2 or $D-T_2$ profile.

A.1 Matlab Subprograms and Subroutines

There are 7 main files that prepare the data for inversion. Data is extracted from *.RiNMR files using *lect1_prof.m* (for the RARE inversion) or *readRiDat.m* ($D-T_2$ profiling inversion). After the data has been imported into Matlab, the individual echoes are isolated using *divide_data.m*. Next, the Fourier reconstruction (Liang & Lauterbur, 2000) is performed using *ft_phase_rotation.m*. After application of the Fourier transform to all of the echoes, rotation of the echo data is performed using *rotate_profile.m*. The file *sample_heigh.m* determines the height of the sample. If desired, the user can manually enter the position of the top and bottom of the sample by adjusting the variables *top* and *bottom*. Averaging of the profiles is performed in *prof_avg.m* (RARE inversion) or *divide_data.m* ($D-T_2$ profiling inversion). The selected weights for the profile average can be modified in these two files.

A.2 Operation of Matlab Code for RARE experiment

In order to process data for a RARE experiment, the raw data acquired from the Maran must be saved as an *.RiDat file by using the WR command at the RINMR prompt. The data file can be stored at any location accessible by the computer running the Matlab inversion.

At the Matlab prompt, type *rare* to execute the code. A graphical interface should appear. Click the *Select Directory* button. After the navigation window will appears, navigate to the appropriate directory, select any file in the directory, and click open. All of the *.RiDat files stored in this directory will appear in the box below the *Select Directory* button. Click the desired file to load the data into Matlab. Once the data has been loaded, all of the data acquired on the Maran will be plotted. Individual or groups of echoes and profiles can be displayed by using the plotting commands in the center of the window. In order to start the T_2 inversion, click the *Estimate T2* button. A new window should appear that will allow you to set the relevant parameters for the inversion. Once the parameters have been selected, select *Calculate T2* to begin the inversion. Upon completion, the T_2 profile will be displayed and all relevant data and results will be saved in the \Results subfolder in a file with the same name as the *.RiDat file. Each results file contains two Matlab structs: *parameters* which contains the experimental parameters and *results* which stores the results from the inversion.

A.2 Operation of Matlab Code for $D-T_2$ profiling experiment

In order to process data for a $D-T_2$ profiling experiment, the raw data acquired from the Maran must be saved as an *.RiDat file by using the WR command at the RINMR prompt. If the *.dprof* script is run on the Maran, data files will automatically be saved in this fashion with the appropriate name convention for the Matlab code. The data files can be stored at any location accessible by the computer running the Matlab inversion, but must be stored in the same directory.

Data processing should begin by opening *loaddata_dt2prof.m*. In this file, parameters such as T_1-T_2 ratio and the calibrated gradient factor can be set. The user should set the variable *NtE* (line 6) to number of gradient values used in the experiment. The variable *direct* can be set to the directory in which the data is stored. Similarly, enter the appropriate filename for the variable *filename*. Additionally, if the user wishes to drop a certain experiment from the inversion analysis, the *drop* variable must be changes from 0 to the number or set of numbers corresponding to the experiments to be neglected during analysis. This number corresponds to the position within the list of gradient values used when running *.dprof* on the Maran. Once these parameters have been set, execution of this program will load the data into Matlab. The raw data and parameters are saved in the files named *datafile* and *parameters*, respectively. Next, return to the Matlab command prompt and type *gamut* to begin the data inversion. Upon completion this program will plot the resulting profile and save all the results in a file named *mapoutmod*. The inversion is performed at multiple values for the regularization parameter. All values of the regularization parameter are stored in the vector *alphas*.

The profiles can be regenerated for an alternate regularization parameter by modifying the variable *index* in *distros_many.m*. *index* varies between 1 and 25. Additional parameters used in the calculation performed in *distros_many.m*, such as Hydrogen Index or the expected M_0 for a known volume of water, are defined in the first few lines of the file and can be modified as needed. The cutoff value for D can be modified in the file *mapplot3_many.m* by changing the variable *cutoff*. In order to run one of the fitting procedures (section 3.) to determine saturation, uncomment the *sat_fit2* (line 153) or *sat_fit3* (line 154) command for fitting of D or $D-T_2$ distributions, respectively.

If the profile consists of multiple measurement regions, the results from each section can be combined into a single profile by using *distros_many.m*. First, the filenames for all relevant datafiles (*datafile*, *parameters*, and *mapoutmod*) must be appended with number corresponding to the measurement region. If experiments are performed over 10 individual regions, the datafiles corresponding to the bottom-most region should be appended with a 1 (e.g. *datafile1*, *parameters1*, and *mapoutmod1*), and for the uppermost region should be appended with a 10 (e.g. *datafile10*, *parameters10*, and *mapoutmod10*). Next, the variable *num_files* should be set equal to the number of measurement regions. Finally, executing *distros_many.m* will generate the combined profiles for all the specified measurement regions.